



12-2000

## Investigations of chiral effects in molecular spectroscopy

Shannon Mark Mahurin

Follow this and additional works at: [https://trace.tennessee.edu/utk\\_graddiss](https://trace.tennessee.edu/utk_graddiss)

---

### Recommended Citation

Mahurin, Shannon Mark, "Investigations of chiral effects in molecular spectroscopy. " PhD diss., University of Tennessee, 2000.  
[https://trace.tennessee.edu/utk\\_graddiss/8342](https://trace.tennessee.edu/utk_graddiss/8342)

This Dissertation is brought to you for free and open access by the Graduate School at TRACE: Tennessee Research and Creative Exchange. It has been accepted for inclusion in Doctoral Dissertations by an authorized administrator of TRACE: Tennessee Research and Creative Exchange. For more information, please contact [trace@utk.edu](mailto:trace@utk.edu).

To the Graduate Council:

I am submitting herewith a dissertation written by Shannon Mark Mahurin entitled "Investigations of chiral effects in molecular spectroscopy." I have examined the final electronic copy of this dissertation for form and content and recommend that it be accepted in partial fulfillment of the requirements for the degree of Doctor of Philosophy, with a major in Physics.

Robert N. Compton, Major Professor

We have read this dissertation and recommend its acceptance:

Robert Hinde, Marianne Breinig, Jon Levin

Accepted for the Council:

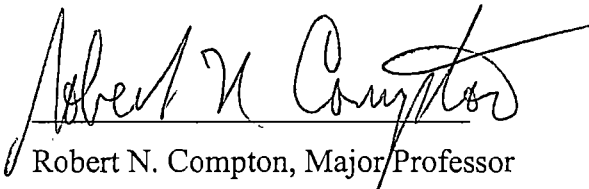
Carolyn R. Hodges

Vice Provost and Dean of the Graduate School

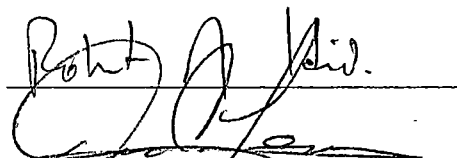
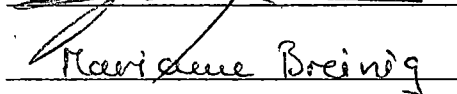
(Original signatures are on file with official student records.)

To the Graduate Council:

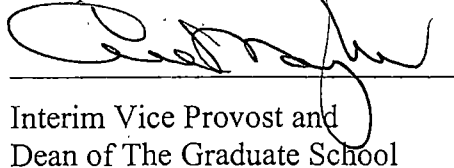
I am submitting herewith a dissertation written by Shannon Mark Mahurin entitled "Investigations of Chiral Effects in Molecular Spectroscopy." I have examined the final copy of this dissertation for form and content and recommend that it be accepted in partial fulfillment of the requirements for the degree of Doctor of Philosophy, with a major in Physics.

  
Robert N. Compton, Major Professor

We have read this dissertation  
and recommend its acceptance:

  
  
Marielene Breinig

Accepted for the Council:

  
Interim Vice Provost and  
Dean of The Graduate School

# Investigations of Chiral Effects in Molecular Spectroscopy

A Dissertation

Presented for the

Doctor of Philosophy

Degree

The University of Tennessee, Knoxville

Shannon Mark Mahurin

December 2000

DEDICATION

To my family for their love and support  
throughout the course of this endeavor.

## ACKNOWLEDGMENTS

I would first like to thank my advisor, Dr. Robert Compton, for his guidance and patience throughout this project. He was always available for discussions and questions, and his lab has been an excellent learning environment. His scientific curiosity and love of learning have truly been an inspiration to me.

I would also like to thank the members of my committee, Dr. Robert Hinde, Dr. Marianne Breinig, and Dr. Jon Levin for their willingness to serve and for their suggestions and comments.

I want to thank Dr. Amer Lahamer for his assistance with the Mössbauer data and for numerous helpful discussions. I also want to thank Dr. Jim Bogard for his assistance with the radiation sources.

Finally, I would like to extend a special thank you to all my friends and colleagues, particularly those in Dr. Compton's group, who have made my experience here such an enjoyable one.

## ABSTRACT

A consequence of the chiral weak interaction is that the enantiomers of a chiral molecule will differ in energy by the minute parity-violating energy difference (PVED). The enantiomers of a chiral iron complex were prepared and characterized with various spectroscopies, including x-ray photoelectron spectroscopy and x-ray diffraction. Measurements of the Mössbauer spectra show a small difference in the energy of the two enantiomers ( $\sim 10^{-10}$  eV). This energy difference nears the expected order of magnitude of the parity-violating energy difference for a molecule in which the chiral center is a high Z atom.

Sodium chlorate has been known to form chiral crystals from achiral aqueous solutions for over one hundred years. Typically, equal numbers of right- and left-handed crystals are produced in unstirred crystallizations. Data has been taken that show an excess of right-handed crystals are produced when crystallizations occur under the influence of a beta source. The beta particles are spin polarized due to the chiral weak interaction which is responsible for beta decay. Preliminary results indicate that the influence of positrons (which are spin polarized oppositely to beta particles) is in the opposite direction.

Finally, measurements of mass resolved resonant and non-resonant multiphoton ionization of the chiral 2-butylamine entrained in a nozzle jet expansion into a linear time-of-flight mass spectrometer constructed in house were obtained using right- and left-circularly polarized laser light. In addition, ratios of ionization rates for linearly and circularly polarized light were measured.

## TABLE OF CONTENTS

CHAPTER	PAGE
I. INTRODUCTION	1
Historical Perspective	1
Optical Activity in Isotropic Media	2
II. SEARCH FOR PVED IN $\text{Fe}(\text{phen})_3\text{Sb}_2(\text{C}_4\text{H}_2\text{O}_6)_2$	14
Introduction	14
Synthesis and Characterization	22
Raman	30
ESCA	31
Mössbauer	36
Results and Discussion	39
III. CRYSTALLIZATIONS OF SODIUM CHLORATE AND SODIUM BROMATE	47
Introduction	47
Experimental	51
Results and Discussion	54
Conclusion	73
IV. EXPERIMENTAL APPARATUS	75
Introduction	75
Laser System	76
Time-Of-Flight Mass Spectrometer	77
Testing and Initial Measurements	84
Conclusion	101
V. MULTIPHOTON IONIZATION OF 2-BUTYLAMINE	102
Introduction	102
Experimental	107
Results and Discussion	108
Conclusion	127
VI. CONCLUSIONS	131
LIST OF REFERENCES	133
APPENDICES	138
VITA	143



## LIST OF TABLES

TABLE	PAGE
I. Summary of Mössbauer data	43
II. Unstirred crystallizations of sodium chlorate	56
III. Unstirred crystallizations of sodium bromate	60
IV. Sodium chlorate crystallizations under $\text{Sr}^{90}$ source	63
V. Sodium chlorate controls (at RADCAL)	68
VI. Sodium chlorate crystallizations under $\text{Na}^{22}$ source	71

## LIST OF FIGURES

FIGURE	PAGE
1. A photograph of the optical rotation of laser light as it propagates through a sucrose solution	7
2. Experimental setup used to measure the optical activity of sucrose	9
3. Plots of laser intensity as a function of distance for four different laser wavelengths	10
4. Optical rotatory dispersion (ORD) curve for sucrose. The line represents a theoretical plot based on the Drude equation	11
5. Plot of the inverse specific rotation versus the square of the wavelength (in nanometers). The slope determines the rotation constant	12
6. Structures of the l and d forms of the cations showing the propeller shapes of ligands bonded to the central iron atom	23
7. Diffraction patterns for the two enantiomers of the iron complex	25
8. Plot of the circular dichroism (CD) and the optical rotatory dispersion (ORD) for the d-Fe(phen) <sub>3</sub> Sb <sub>2</sub> (C <sub>4</sub> H <sub>2</sub> O <sub>6</sub> ) <sub>2</sub> . The mirror enantiomers show the expected opposite CD and ORD	26
9. Racemization curve for the Fe complex in acetonitrile	28
10. Electrospray time-of-flight mass spectra of the iron complex	29
11. Raman spectra for the iron complex with two different counter ions	32
12. ESCA spectra for the two enantiomers of the iron complex	34
13. ESCA spectrum for the gold foil used as a calibration (note the mercury peak)	35
14. Decay scheme of the <sup>57</sup> Co to produce a 14.4 keV gamma ray	37
15. Setup for the Mössbauer experiment	40

FIGURE	viii PAGE
16. Mössbauer spectra for the two enantiomers of the iron complex	41
17. Diagram showing the parity violating energy difference in the two enantiomers of a chiral molecule	44
18. Stereographic view of the sodium chlorate and sodium bromate crystals	52
19. Setup used to determine the handedness of NaClO <sub>3</sub> and NaBrO <sub>3</sub> crystals	53
20. Diagram of the experimental setup used to study the effect of beta radiation on the crystallization of NaClO <sub>3</sub> and NaBrO <sub>3</sub>	55
21. Histogram of the unstirred crystallizations of NaClO <sub>3</sub>	58
22. Scatter plot of the crystallizations of NaClO <sub>3</sub> showing the random nature of the primary nucleation	59
23. Histogram of the unstirred crystallizations of NaBrO <sub>3</sub>	61
24. Crystallizations of NaClO <sub>3</sub> under the influence of a 41 mCi Sr <sup>90</sup> beta source	65
25. Sodium chlorate control experiments performed at the same site as the beta radiolysis experiments	69
26. Histogram of the crystallizations of NaClO <sub>3</sub> under the influence of a Na <sup>22</sup> positron source	72
27. Diagram of the time-of-flight mass spectrometer	78
28. Diagram of the timing sequence for triggering the gas pulse and the laser system	81
29. Diagram of the microchannel plate system used to detect ions in the mass spectrometer	83
30. Diagram of the mass spectrometer along with the electronics used to acquire data	85
31. Energy level diagram for nitric oxide (NO)	86

FIGURE	PAGE
32. (2+2) REMPI of nitric oxide through the $A^2\Sigma^+$ state	89
33. Energy level diagram for (3+2) REMPI through the 6s state of xenon	90
34. Mass spectrum of xenon. The bottom curve shows data taken with the TOF described in this thesis while the top curve shows a mass spectrum calculated using IsoPro	92
35. Diagram of the setup used to select various polarizations of the laser beam	95
36. Polarization effects on the (3+2) REMPI of xenon. Note the absence of signal with circularly polarized light	96
37. Diagram of the complete setup used to obtain mass spectra as a function of laser polarization	98
38. Wavelength dependence of the (3+2) REMPI of nitric oxide	100
39. Mass spectrum of 2-butylamine	109
40. Mass spectrum of 2-butylamine using xenon and argon as carrier gases	111
41. Mass spectra of 2-butylamine showing the decrease in ionization intensity for longer wavelengths	113
42. Wavelength dependence of 2-butylamine showing the (2+2) REMPI through the 3s Rydberg state	114
43. Wavelength dependence of the MPI of the 2-butylamine dimer showing the dip in signal at 473.35 nm	116
44. Polarization dependence of the MPI of racemic 2-butylamine at 473.35 nm	118
45. Polarization dependence of the MPI of (R)-(-)-2-butylamine at 473.35 nm	120
46. Polarization dependence of the MPI of (R)-(-)-2-butylamine at 470 nm	121

FIGURE	PAGE <sup>x</sup>
47. Polarization dependence of the MPI of racemic 2-butylamine dimer at 473.35 nm	122
48. Polarization dependence of the MPI of (S)-(+)-2-butylamine at 473.35 nm	123
49. Wavelength dependence of the (2+2) REMPI of benzene through the $^1B_{2u}$ the state	125
50. Polarization dependence of the MPI of benzene	126
51. Polarization dependence of the MPI of (R)-(-)-2-butylamine at 473.35 nm	128
52. Circular dichroism of (R)-(-)-2-butylamine	129

## CHAPTER I

## INTRODUCTION

Historical Perspective

In 1811, the French physicist Dominique F. J. Arago noticed that linearly polarized sunlight could be separated into its constituent colors by passing it along the optical axis of quartz crystal and analyzing it with a pile-of-plates polarizer. Though he failed to fully appreciate his observations in terms of optical rotation, this was the first observation of optical activity and optical rotatory dispersion, which are defined as the rotation of the plane of polarization of linearly polarized light and the unequal rotation of the plane of polarization of light of different wavelengths, respectively. Jean Baptiste Biot performed a more detailed study of quartz crystals ( $\text{SiO}_2$  arranged in a trigonal crystal structure) and the colors produced in Arago's experiments and correctly attributed the phenomena to optical rotation. In addition, he noted that there were two forms of quartz that rotated linearly polarized light in opposite directions.<sup>1</sup> A percentage of the  $\alpha$ -quartz crystals used by Biot had small extra faces such that they could exist in two different forms that, coincidentally, corresponded to the different rotations. In this case, the morphology of the quartz crystals matched the sense of rotation, which turned out to be quite serendipitous.

Building on the previous work of Biot, Louis Pasteur observed that sodium ammonium tartrate salts formed from tartaric acid also crystallized in two forms, each one a mirror image of the other. Using tweezers, Pasteur physically separated the two forms and dissolved them in water. He discovered that even though going to solution had destroyed the chirality of the crystal structure, the optical activity of the two solutions matched that

of the crystals. This observation led him to postulate that the *molecules* that composed the tartrate salts also possessed the requisite nonsuperimposability that determined chirality, i.e., sodium ammonium tartrate molecules are chiral.

While experimenting with a racemic mixture (which corresponds to equal numbers of right and left handed molecules) of the tartrates, Pasteur found that by allowing the racemate to ferment, a yeast formed and the remaining tartrate developed a rotatory power. Using a polarimeter, he noted that the sense of the rotation was always left handed. He thus concluded that the mold had only interacted with one form, leaving the other unaffected. The idea that certain biological systems would interact with only molecules of one handedness along with the discovery that natural organic products possessed optical rotatory power led Pasteur to make his famous statement that “L’ univers est dissymetrique” (“the universe is dissymmetric”)<sup>2</sup>. Since the discoveries of Biot and Pasteur, the study of optically active substances has become increasingly important, particularly in the pharmaceutical industry since many drugs are chiral and the different forms interact differently with biological systems.

#### Optical Activity in Isotropic Media

As has already been mentioned, Pasteur was the first to note that molecular dissymmetry was a necessary condition for optical activity. Thus, in order for an isotropic material (such as a liquid) to rotate the plane of polarization of linearly polarized light, the molecules that make up the material must exist as mirror images that are nonsuperimposable. The two mirror images of the molecule are known as enantiomers. The necessary symmetry conditions for optical activity are the absence of a plane of symmetry, center of inversion, and an improper axis of rotation. Any molecule that

meets the above conditions will possess nonsuperimposable mirror images and exhibit optical activity.

Optical activity in crystals is fundamentally different from optical activity in isotropic liquids. While the latter requires molecular dissymmetry, the former does not, i.e., it is not necessary for the molecules that make up a crystal to exhibit the nonsuperimposability condition. Optical activity in crystals is achieved when the molecules that make up the crystal are arranged in such a fashion as to exhibit a specific handedness. For example, sodium chlorate ( $\text{NaClO}_3$ ), which is an achiral molecule and is not optically active in solution, crystallizes in such a manner as to form a helix in which the oxygen atoms spiral along the axis. Thus, the crystalline form of sodium chlorate is optically active while the molecule is not.

At this point, it becomes necessary to distinguish between two types of birefringence. Linear birefringence is the separation of a light beam into two components that travel at different speeds in a medium as a result of a difference in the index of refraction for linearly polarized light beams parallel and perpendicular to the optical axis. Calcite is an example of a linearly birefringent material, as evidenced by the fact that when a ray is passed through the crystal axis it splits into two rays known as the ordinary and extraordinary rays. Circular birefringence, on the other hand, pertains to circularly polarized light as opposed to linearly polarized light. A material that has one index of refraction for right circularly polarized light,  $n_R$ , and one index of refraction for left circularly polarized light,  $n_L$ , is said to be circularly birefringent. A material that exhibits linear birefringence is not necessarily optically active, and a material that exhibits optical activity is not necessarily linearly birefringent.



Since linearly polarized light is composed of right and left circularly polarized light, a material that displays circular birefringence also exhibits optical activity. This can be easily understood by noting that since the indices of refraction for the two polarizations are different, the velocities of the two waves will also be different as they propagate through a circularly birefringent material. As one of the waves slows down with respect to the other, a phase difference between the two waves develops. The net effect is the rotation of the original linearly polarized beam. The magnitude of the rotation,  $\phi$ , can be expressed by Fresnel's equation<sup>3</sup>:

$$\phi = \frac{\pi(n_L - n_R)L}{\lambda} \quad (1.1)$$

where  $n_L$  and  $n_R$  correspond to the indices of refraction for left and right circularly polarized light, respectively,  $\lambda$  is the wavelength of the incident beam, and  $L$  is the path length. Circular dichroism, which is the differential absorption of right and left circularly polarized light, is related to the optical rotation through the Kramers-Kronig relation<sup>4</sup> given by the following:

$$\Delta\theta(f_\omega) = \frac{2\omega^2}{\pi} P \int_0^\infty \frac{\Delta\eta(g_\xi)d\xi}{\xi(\xi^2 - \omega^2)} \quad (1.2)$$

$$\Delta\eta(g_\omega) = -\frac{2\omega^3}{\pi} P \int_0^\infty \frac{\Delta\theta(f_\xi)d\xi}{\xi^2(\xi^2 - \omega^2)} \quad (1.3)$$

where  $\Delta\theta$  is the optical rotatory dispersion,  $\Delta\eta$  is the circular dichroism, and  $P$  indicates the Cauchy principal value. Clearly, the optical rotation and circular dichroism spectra are inherently intertwined. Knowledge of the complete spectrum of one allows the calculation of the other.

For a chiral material in liquid phase, the angle through which the polarization vector is rotated is determined by the density or concentration of the optically active component, as well as the path length, and the wavelength. Thus, in order to standardize the reporting of optical activity for liquids, the specific rotation has been adopted as a quantitative measure of these effects. The specific rotation for a chiral solution, denoted by  $[\alpha]_{\lambda}^T$ , is defined as:

$$[\alpha]_{\lambda}^T = \frac{\phi}{L \cdot c} \quad (1.4)$$

where  $\phi$  is the measured angle in degrees, L is the path length in decimeters, and c is the concentration in g/mL. The magnitude of the optical rotation can also depend on the temperature, decreasing for some compounds such as uridine<sup>5</sup> while increasing for others. To further standardize values, specific rotations are typically given at room temperature and, since the rotation also depends on wavelength, the sodium D line (which corresponds to a wavelength of 589 nm) is used. A plot of the specific rotation of a chiral medium as a function of the wavelength is known as an *optical rotatory dispersion* curve and it can be useful for gaining insight into the electronic structure of the medium of interest, particularly since the rotations are typically the result of electronic transitions within the molecule. For wavelengths that are well outside a single resonance absorption region of the material, the optical rotatory dispersion (ORD) can be described by the Drude expression:<sup>6</sup>

$$[\alpha]_{\lambda}^T = \frac{A}{\lambda^2 - \lambda_0^2} \quad (1.5)$$

where  $A$  is a constant known as the rotation constant and  $\lambda_0$  is the dispersion constant which corresponds to absorption wavelengths. If several optically allowed transitions contribute in the region of wavelength  $\lambda$ , the optical rotation is a sum over such expressions, i.e.,

$$[\alpha]_{\lambda}^T = \sum_i \frac{A_i}{\lambda^2 - \lambda_{0i}^2} \quad (1.6)$$

A vivid demonstration of optical activity, first described by Zare et al.<sup>7</sup> and later quantified by Mahurin et al.<sup>8</sup>, can be seen by directing a linearly polarized laser beam (e.g., a HeNe laser works well) down a 1 meter cylindrical glass tube filled with a sucrose solution with a concentration of .81 g/mL (made by dissolving 81 g of sucrose in enough water to make 100 mL of solution). Polarized light was scattered at right angles to the direction of propagation as a result of a combination of Tyndall and Rayleigh scattering. The scattering cross section of linearly polarized light from a collection of small identical particles is given by:

$$\frac{d\sigma}{d\Omega} = \frac{16\pi^4 r^6 N}{\lambda^4} \left( \frac{n^2 - 1}{n^2 + 2} \right)^2 \sin^2 \phi \quad (1.7)$$

where  $n$  is the index of refraction of the medium,  $r$  is the radius of the scattering particles,  $N$  is the particle density,  $\lambda$  is the wavelength, and  $\phi$  is the angle of observation with respect to the plane of polarization. Maximum scattering intensity occurred at right angles to the plane of polarization as indicated by the angular dependence in equation (1.7). The rotation of the beam is clearly seen as alternating bright and dark regions as the light polarization vector "spirals" along the tube (see Figure 1). The specific rotation can be obtained from equation (1.4) by measuring the distance,  $L$ , between consecutive



Figure 1. A photograph of the optical rotation of laser light as it propagates through a sucrose solution.

maximum or minimum intensities (which corresponds to a  $180^\circ$  rotation in the plane of polarization). In addition, the specific rotation at a variety of wavelengths, including four lines from a Coherent Argon-ion laser (456.9, 476.5, 488.0, 514.5 nm), the 632.4 nm line from a HeNe laser, and the 785 nm line from a diode laser, were acquired to construct the ORD curve. The ORD curve was then fit to the Drude equation, equation (1.5), to obtain values for the rotation and dispersion constants.

The experimental setup, as shown in Figure 2, essentially consisted of the laser, a polarizer, the tube of sucrose solution, and the detector system. The detector used to measure the intensity of the scattered beam was an RCA IP28 photomultiplier tube (PMT) mounted on a monochromator with a second polarizer whose polarization axis was perpendicular to the direction of laser propagation and parallel to the polarization of the incident laser beam. The intensity of the scattered beam was recorded as a function of distance as the detector system, which was mounted on a translation stage, moved along the length of the tube. Due to some reflections from the input and output windows of the cylindrical tube, no measurements were taken near either end. Figure 3 shows plots of the intensity of the scattered beam as a function of position for four different wavelengths. The ORD curve and its fit to the Drude equation are displayed in Figure 4. The two constants were obtained by plotting  $1/[\alpha]_\lambda^T$  versus  $\lambda^2$  (see Figure 5) and performing a linear least-squares fit. The values of the rotation and dispersion constants were found to be  $A=2.17 \times 10^7$ , and  $\lambda_0 = 131 \pm 10$  nm. These values are in reasonable agreement with the values of  $A=2.1648 \times 10^7$ , and  $\lambda_0 = 146$  nm obtained by Lowry and Richards.<sup>9</sup> This method for studying optical activity thus proves to be of some practical benefit as a means for accurately obtaining the specific rotation of chiral molecules in

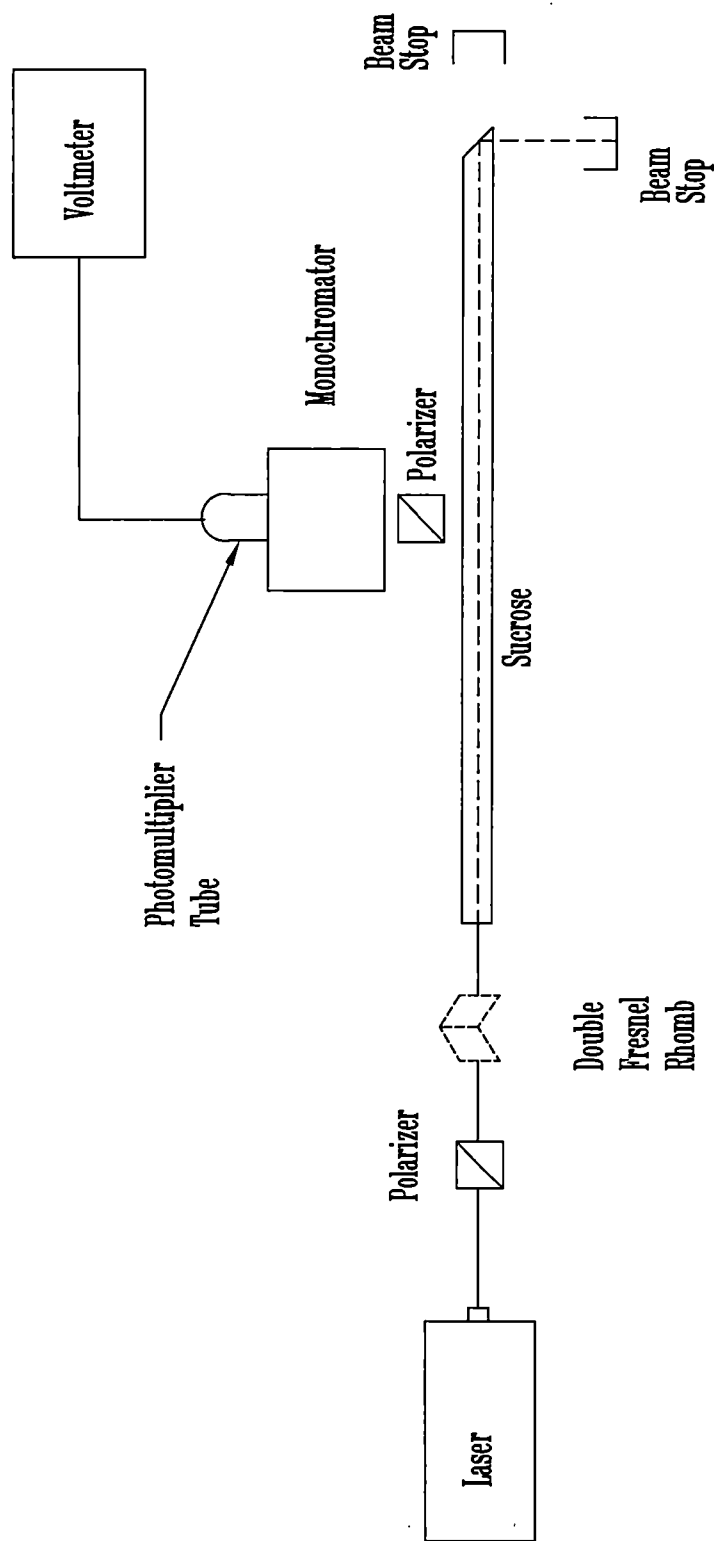


Figure 2. Experimental setup used to measure the optical activity of sucrose.

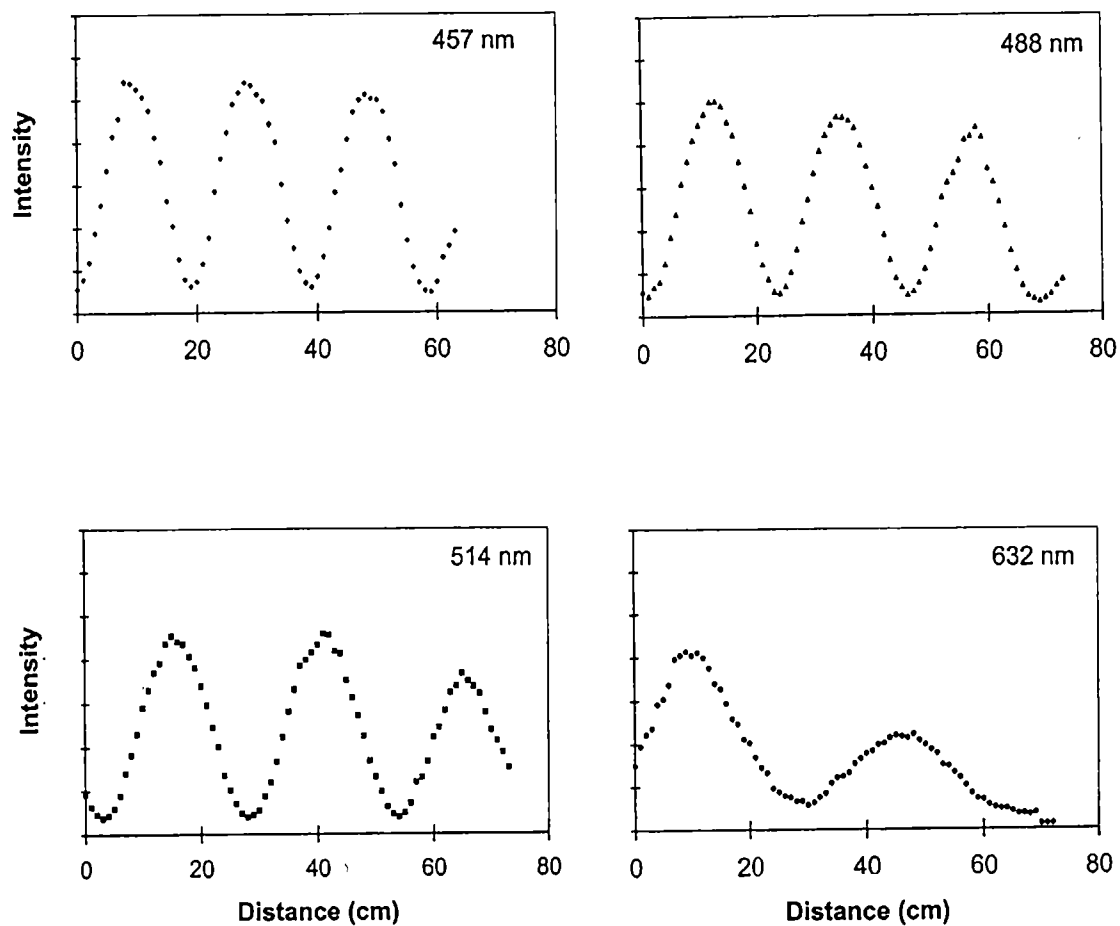


Figure 3. Plots of laser intensity as a function of distance for four different laser wavelengths.

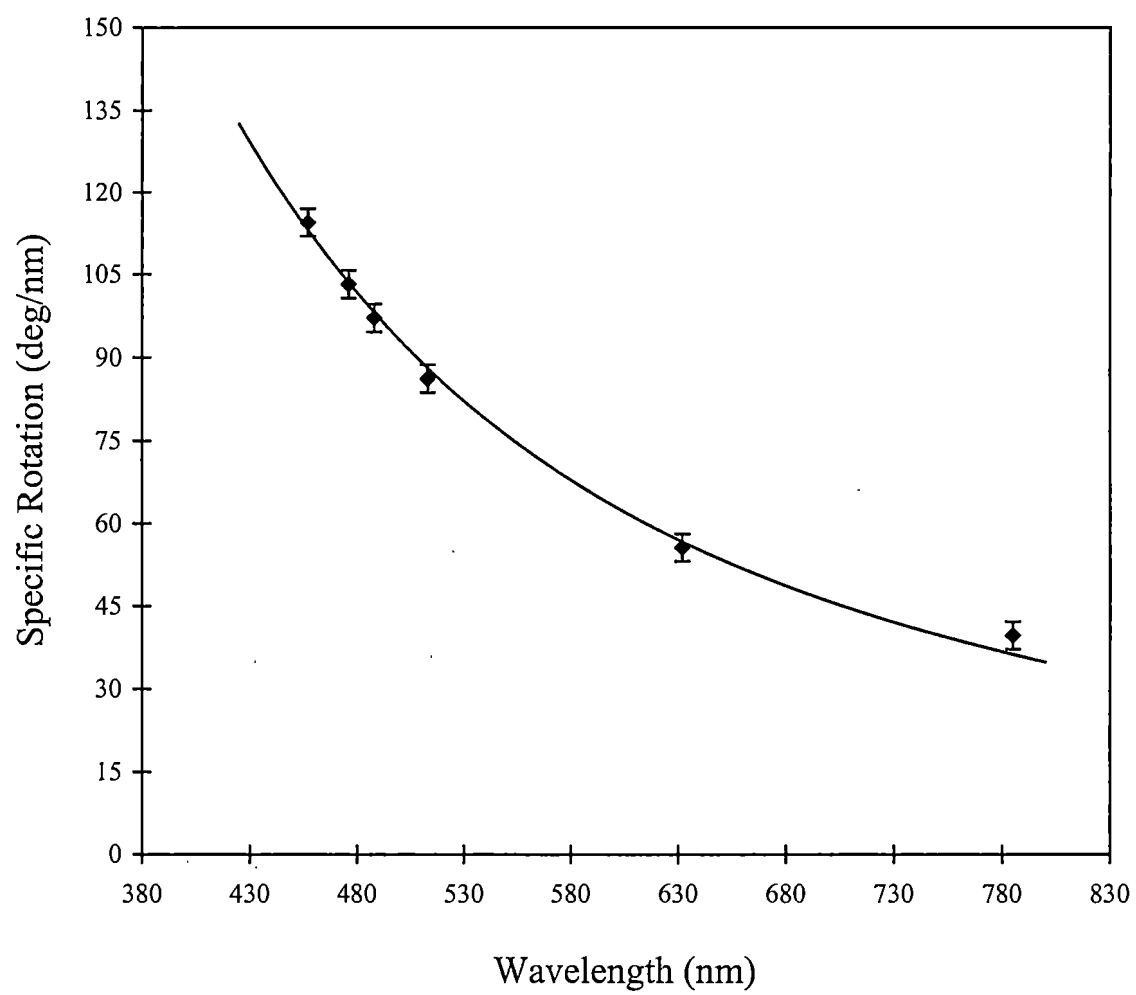


Figure 4. Optical rotatory dispersion (ORD) curve for sucrose. The line represents a theoretical plot based on the Drude equation.



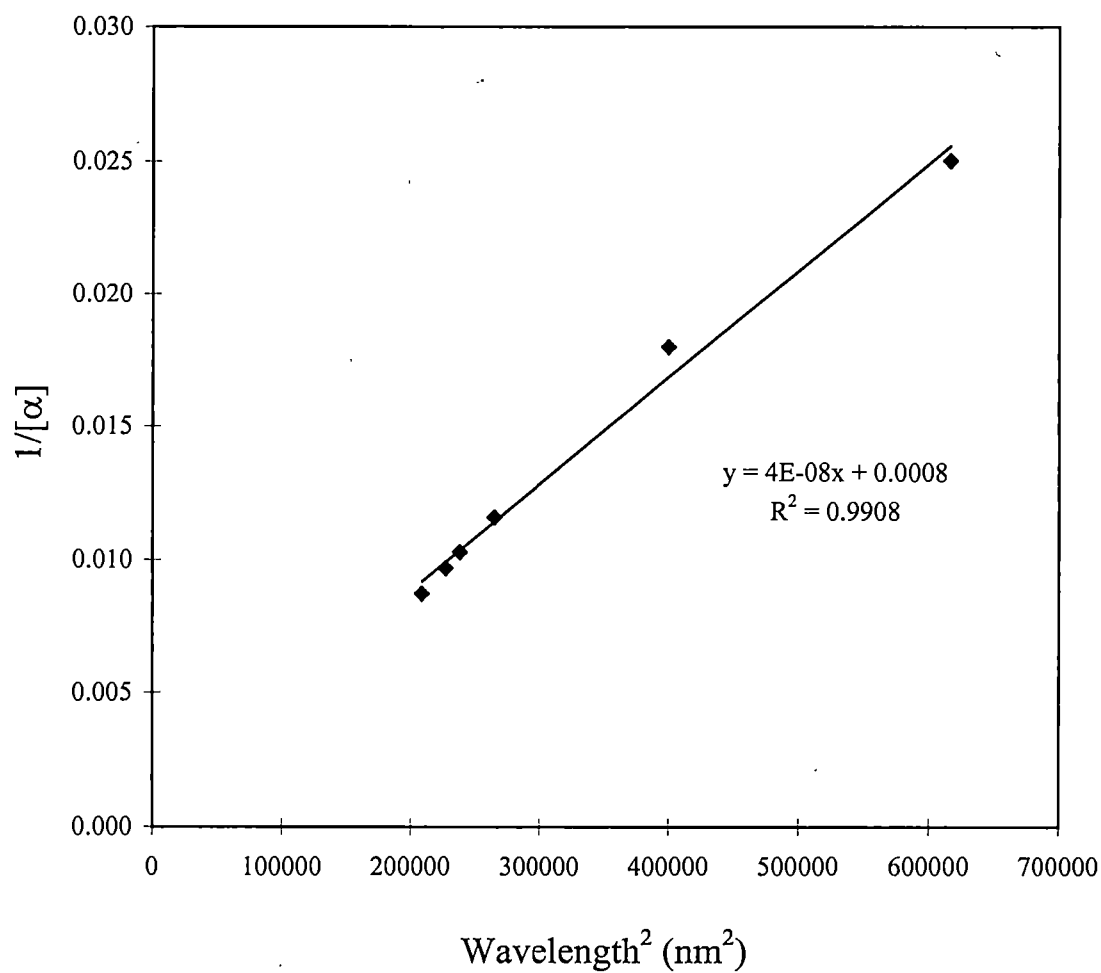


Figure 5. Plot of the inverse specific rotation versus the square of the wavelength (in nanometers). The slope of the line determines the rotation constant.

solution as well as being a visually striking demonstration of the effect. Furthermore, as the light propagates through the medium, it becomes slightly elliptically polarized since right- and left-circularly polarized light are differentially absorbed. In principle, the degree of ellipticity is a measure of the circular dichroism of the medium. This effect could be used in conjunction with long path lengths to measure circular dichroism in dilute samples.

## CHAPTER II

SEARCH FOR PVED IN  $\text{Fe}(\text{phen})_3\text{Sb}_2(\text{C}_4\text{H}_2\text{O}_6)_2$ Introduction

Symmetry is one of the most fundamental concepts in nature and molecular symmetry has become invaluable in the study of spectroscopy. Symmetry is also responsible for the conservation laws. For example, if a system is invariant under translation, the Lagrangian for that system is also invariant under translation, i.e.,

$$\delta L = 0 \quad (2.1)$$

When a single particle confined to one dimension is considered, the following is obtained for a small displacement:

$$\delta L = \frac{\partial L}{\partial q} \delta q + \frac{\partial L}{\partial \dot{q}} \delta \dot{q} = 0 \quad (2.2)$$

Since the displacement is not a function of time, the second term vanishes. In order for  $\delta L$  to be zero:

$$\frac{\partial L}{\partial q} = 0. \quad (2.3)$$

Inserting into Lagrange's equation yields:

$$\frac{d}{dt} \left( \frac{\partial L}{\partial \dot{q}} \right) = \frac{d}{dt} (p) = 0. \quad (2.4)$$

where  $p$  is the generalized momentum. Thus, the symmetry of translation allows for the conservation of momentum. Applying a similar derivation, one finds that the symmetry of rotation leads to conservation of angular momentum while symmetry of time corresponds to the conservation of energy. Furthermore, mirror (or spatial) symmetry is

observed in numerous molecules as well as various physical interactions. Optical rotation, as discussed in the previous chapter, is a property of chiral molecules which preserves mirror symmetry. This can be easily understood by noting that one enantiomer of a chiral molecule will rotate the plane of polarization of linearly polarized light clockwise while its mirror image will rotate the plane of polarization counterclockwise (at the same wavelength), which is identical to the rotation of the other enantiomer. In other words, the mirror image process of the optical rotation of one enantiomer occurs in nature, i.e., the optical rotation of the other enantiomer. In contrast, individual atoms possess no geometrical handedness. It would therefore seem logical to assume that atoms do not exhibit optical rotation or circular dichroism. However, it turns out that this assumption is incorrect.

For many years it was thought that the four fundamental forces in nature (i.e., gravitational, weak, strong, and electromagnetic) conserved parity, or mirror symmetry. In the early 1950's, it was discovered that the K meson would sometimes decay into two pions, which possess negative parity, and sometimes into three. Thus, there was a nonzero probability that the K meson would decay into two final states of opposite parity. In 1956, Lee and Yang<sup>10</sup> postulated that either parity was not conserved in this particular decay process, or the K meson was a parity doublet. They suggested that parity violation in the weak interaction could be proven through an asymmetry in the distribution of electrons emitted via the beta decay of an oriented nucleus in the  $\theta$  direction and the  $180-\theta$  direction (where  $\theta$  is the polarization direction of oriented nuclei). One year later in 1957, Wu, et al.,<sup>11</sup> discovered that spin polarized  $^{60}\text{Co}$  nuclei asymmetrically emitted beta particles, proving that the weak force, which is typically associated with the decay of a

neutron into a proton, an electron ( $\beta^-$ ), and an antineutrino, did in fact violate parity. Clearly, parity violation in the weak interaction, as evidenced in the emission of a spin polarized  $\beta^-$  particle, is accompanied by a change in charge from a neutron, which is charge neutral, to a proton and an electron. Many researchers believed that this change in charge essentially eliminated any possible effect that the weak interaction might have on atomic energy levels since atomic transitions clearly were not accompanied by a modification in the identity of the participating particles.

In the late 1960's, Glashow,<sup>12</sup> Weinberg<sup>13</sup>, and Salam<sup>14</sup> independently proposed that the weak interaction and the electromagnetic interaction were simply different manifestations of the same electroweak force. The electroweak theory was subsequently placed on firm mathematical footing by Gerard 't Hooft<sup>15</sup>. The unification of the electromagnetic and weak interactions resulted in the prediction of a third, neutral gauge boson,  $Z^0$ , which carries no electric charge. These weak neutral currents give rise to an anapole moment for nuclei which has only recently been observed in atomic cesium.<sup>16</sup> As a gauge boson, the  $Z^0$  boson violates parity, but since the interactions mediated by this boson do not involve a change in the identity of the interacting particles, the possibility existed for the  $Z^0$  boson to affect atomic processes, i.e., the exchange of virtual  $Z^0$  bosons between the orbiting electrons and the quarks in the nucleus could result in physically observable effects in the interaction of light with atoms. A variety of experimental methods exist, such as the measurement of a rotation of plane polarized light, that allow for the direct detection of parity violating effects in atoms. Soon after the work of Wu et al., Zel'dovich estimated the magnitude of the optical rotation of linearly polarized light due to the parity nonconserving weak interaction in atomic hydrogen and concluded that the

rotation would be too small to measure.<sup>17</sup> A renewal of interest in parity violating effects in atoms was sparked by the work of Anne Marie and Claude Bouchiat when they pointed out that such effects would undergo a considerable enhancement in heavy atoms.<sup>18</sup> Such parity-violating (P-odd) effects were subsequently observed in the optical rotation for atoms using bismuth vapor.<sup>19</sup> Similar experiments have also been performed on thallium,<sup>20</sup> and lead.<sup>21</sup>

A second method for measuring parity violating effects involves the observation of highly forbidden transitions between atomic states of identical parity like the  $6S_{1/2} - 7S_{1/2}$  transition in atomic cesium. This transition has been observed through fluorescence experiments.<sup>22</sup> In combination with theory, these experimental measurements have provided a sensitive test to the standard model of nuclear physics via the determination of the nuclear weak charge at low energy.<sup>23</sup> Direct weak interaction effects of the type observed in atomic physics have not been reported for molecules, i.e., optical activity of parity forbidden transitions for a homonuclear diatomic such as  $I_2$ .

Interest in parity-violating effects in molecules has focused on the prediction and measurement of the parity-violating energy difference (PVED) between the R and S enantiomers of a chiral molecule. Rein<sup>24</sup> and Letokhov<sup>25</sup> were the first to predict that the parity nonconserving electroweak interaction would lift the degeneracy between enantiomers as predicted by normal quantum electrodynamics. This can be seen quite easily if we consider a total Hamiltonian that contains the parity even electromagnetic part and the parity odd electroweak part.

$$H = H_{\text{even}} + H_{\text{odd}} \quad (2.5)$$

Under the parity operator, the total Hamiltonian transforms as:

$$P^{-1}HP = P^{-1}(H_{\text{even}} + H_{\text{odd}})P \quad (2.6)$$

$$P^{-1}HP = P^{-1}H_{\text{even}}P + P^{-1}H_{\text{odd}}P \quad (2.7)$$

which becomes:

$$P^{-1}HP = H_{\text{even}} - H_{\text{odd}} \quad (2.8)$$

Therefore, the total Hamiltonian does not commute with the parity operator, i.e.,  $[P,H] \neq 0$ .

Consider a state  $A$  such that  $H|A\rangle = E_A|A\rangle$  and the mirror image state  $\tilde{A}$  such that  $|\tilde{A}\rangle = P|A\rangle$  which corresponds to the enantiomer, i.e., the mirror image. The energy of state  $A$  can be calculated as:

$$E_A = \langle A|H|A\rangle \quad (2.9)$$

The energy of the same state in the enantiomer is:

$$E_{\tilde{A}} = \langle \tilde{A}|H|\tilde{A}\rangle = \langle A|P^*HP|A\rangle \neq \langle A|H|A\rangle \quad (2.10)$$

Therefore the degeneracy of energy levels of enantiomers is lifted as a result of the chiral electroweak force.

A number of theoretical calculations of the parity violating energy difference for small molecules have been performed.<sup>26,27,28</sup> As mentioned above, the Hamiltonian for a molecule is composed of the parity conserving electromagnetic part and the parity nonconserving electroweak part. The operator that describes the PVED for a molecule containing  $i$  electrons and  $n$  nuclei is given by:

$$H_{PV} = H_{PV}^1 + H_{PV}^2 \quad (2.11)$$

$$H_{PV} = \left(\frac{G_F}{2\sqrt{2}}\right) \sum_{i,n} Q_{W,n} \gamma_i^5 \rho_n(r_i) + \left(\frac{G_F}{\sqrt{2}}\right) \sum_{i,n} K_n \frac{\kappa_n}{I_n(I_n+1)} \alpha_i \cdot I_n \rho_n(r_i) \quad (2.12)$$

where the summation runs over all electrons,  $i$  and nuclei,  $n$ ,  $G_F$  is the Fermi electroweak coupling constant ( $2.22255 \times 10^{-14}$  a.u. =  $1.16637 \times 10^{-11}$  eV),  $\alpha_i$  are the Dirac matrices in the standard representation,  $\mathbf{I}_n$  is the nuclear spin vector operator,  $K_n$  and  $\kappa_n$  are nuclear parameters for nucleus  $n$ ,  $\gamma^5 = i\gamma^1\gamma^2\gamma^3\gamma^4$  represents a pseudoscalar chirality operator formed from a product of Dirac  $\gamma$ -matrices,  $\rho_n(r_i)$  is the normalized nucleon density, and  $Q_w$  is the weak charge given by:

$$Q_w = -N_n + Z_n(1 - 4\sin^2 \theta_w) \quad (2.13)$$

where  $N_n$  and  $Z_n$  are the number of neutrons and protons, respectively, and  $\theta_w$  is the Weinberg mixing angle.

An order of magnitude estimate of the energy shift has been obtained by Hegstrom, et al.,<sup>29</sup> based on the nature of the operators in the Hamiltonian:

$$\Delta E_{PV} = G\alpha^3 Z^5 \eta \quad (2.14)$$

where  $G$  is the Fermi electroweak constant,  $Z$  is the atomic number,  $\alpha$  is the fine structure constant ( $1/137$ ), and  $\eta$  is a molecular asymmetry constant that takes into account the chiral character of the molecular environment. An important factor in this equation is the  $Z^5$  scaling law, i.e., as the atomic number of the atoms that comprise the molecule increases the parity-violating energy difference increases. For molecules containing atoms with small atomic number, the predicted ratio of the PVED to total energy is  $\Delta E_{PV}/E=10^{-18}$ . In arriving at the  $Z^5$  scaling law, the nonrelativistic limit derived by Hegstrom was employed. However, it has been recently confirmed that by implementing relativistic corrections in the theoretical calculations, a  $Z^6$  scaling law is obtained which



provides a better estimate of the PVED, particularly for chiral molecules composed of high  $Z$  atoms where relativistic effects become more pronounced.<sup>30</sup>

High resolution infrared absorption spectroscopy has been used in two attempts to measure the parity violating energy difference between enantiomers. Because the rotational, vibrational, and electronic energy levels are proportional, a relative change in a rotational or vibrational energy is expected to scale with a change in the electronic energy:

$$\frac{\Delta E_{el}^{PV}}{E_{el}} \approx \frac{\Delta E_{vib}^{PV}}{E_{vib}} \approx \frac{\Delta E_{rot}^{PV}}{E_{rot}} \quad (2.15)$$

The high resolution provided by vibrational spectroscopy has made this area an attractive avenue of experimental pursuit. By utilizing the technique of inverted Lamb dips using infrared laser lines, Arimondo, Glorieux, and Oka<sup>31</sup> measured ro-vibrational transition frequencies of *d*- and *l*- camphor and found them to agree to within an accuracy of  $10^{-8}$ . Daussy et al.<sup>32</sup> recently employed high resolution IR spectroscopy using the  $9.3\mu\text{m}$  line from a  $\text{CO}_2$  laser to show that the carbon-fluorine vibrational modes of the flourochlorobromomethane ( $\text{CHFClBr}$ ) enantiomers are the same to within 13 Hz. This places an upper limit of  $<4 \times 10^{-13}$  on the value of  $\Delta E_{PV}/E$  ( $\Delta E_{PV}=5.5 \times 10^{-14}$  eV). Although this measurement is five orders of magnitude more sensitive than the results obtained by Arimondo et al. for the enantiomers of camphor, recent theoretical studies on  $\text{CHFClBr}$  give an energy difference of only 2 mHz for the C-F vibrational frequency.<sup>33</sup>

In addition to IR spectroscopy, there are other high resolution methods such as Mössbauer and nuclear magnetic resonance (NMR) which represent very sensitive spectroscopic techniques to probe the interactions of electrons surrounding a nucleus and

present considerable promise for measurement of the parity violating energy difference. Barra and Robert<sup>34</sup> considered the existence of parity non-conserving terms (including the nuclear anapole moment) in the molecular Hamiltonian [equation (2.12)] and showed that two enantiomers will exhibit different NMR spectra. By applying a relativistically parametrized extended Hückel method to chiral molecules that contain heavy nuclei such as platinum or lead and omitting the nuclear anapole contribution, they predict a chemical shift of only a few mHz between the enantiomers. At first glance, this difference may seem outside the realm of possibility of current NMR technology. However, Allerhand et al.<sup>35</sup> have reported the measurement of chemical shifts of approximately 10 mHz in <sup>13</sup>C NMR of toluene by eliminating temperature gradients in the sample through improved temperature stability of the air flow used to maintain sample temperature. Despite these improvements in NMR technology, experiments to determine the parity violating energy difference using NMR have yet to be reported.

Due to the high resolution attainable with Mössbauer spectroscopy, some work has been reported in this area in an attempt to measure the PVED. Keszthelyi<sup>36</sup> used Mössbauer spectroscopy to establish an upper limit of  $4 \times 10^{-9}$  eV for the energy difference between *l*- and *d*-tris(1,2-ethanediamine) iridium III complexes using the difference in the uncertainties in the positions of the absorption peaks. It should be pointed out that Keszthelyi did not report the actual Mössbauer spectra and very little details on the experimental procedure were given. The magnitude of the parity violating energy difference for carbon in amino acids has been estimated to be  $\Delta E_{PV} \approx 1 \times 10^{-17}$  kT (where  $kT = .025$  eV at room temperature), which yields a value of  $2.5 \times 10^{-19}$  eV. By multiplying the PVED for carbon by  $(Z/6)^6$ , a value of  $\sim 1.1 \times 10^{-12}$  eV was predicted for the PVED of

iridium in the abovementioned complex. Thus, the measured upper limit is three orders of magnitude higher than the expected Z-scaling result.

There are many reviews on the potential importance of parity violation in chemistry and biology. The most prominent being the implications to *specific* homochirality, i.e., that the building blocks of life have the same handedness, in living organisms through prebiotic asymmetric synthesis. An up to date account of these ideas is provided in a forthcoming review by Frank, Bonner, and Zare.<sup>37</sup> In this thesis, measurements of a very small energy difference in the Mössbauer spectra of the *l* and *d* enantiomers of  $\text{Fe}(\text{phen})\text{Sb}_2(\text{tartrate})_2$  is reported. Possible reasons for this difference, including PVED, will be discussed.

### Synthesis and Characterization

The *l* and *d* enantiomers of the  $\text{Fe}(\text{phen})_3\text{Sb}_2(\text{C}_4\text{H}_2\text{O}_6)_2 \cdot 8\text{H}_2\text{O}$  complex were obtained by initially reacting  $\text{FeCl}_2 \cdot \text{H}_2\text{O}$  with a solution of phenanthroline monohydrate ( $\text{C}_{12}\text{H}_8\text{N}_2 \cdot \text{H}_2\text{O}$ ) to produce a racemic mixture of the  $\text{Fe}(\text{phen})_3^{2+}$  cation. Commercially available potassium antimonyl-(+)-tartrate was added to the solution to produce *l*- $\text{Fe}(\text{phen})_3\text{Sb}_2(\text{C}_4\text{H}_2\text{O}_6)_2 \cdot 8\text{H}_2\text{O}$  where the *l*- designation refers to the counterclockwise rotation of plane polarized light (as one views the light source) for the sodium D line (589 nm). The *d*- enantiomer was synthesized using potassium antimonyl-(-)-tartrate (obtained by some slight modifications of the procedure of Schlessinger<sup>38</sup>) as the resolving agent. Figure 6 shows the molecular structure of the two enantiomers of the  $\text{Fe}(\text{phen})_3^{2+}$  cation as indicated by an initial geometry optimization calculation using PCModel software. The cation consists of a central iron atom with three planar phenanthroline ligands arranged about the iron to form a "propeller" shape. The iron

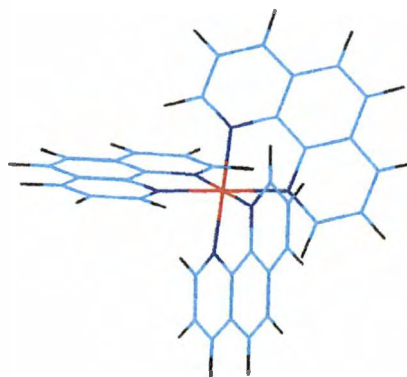
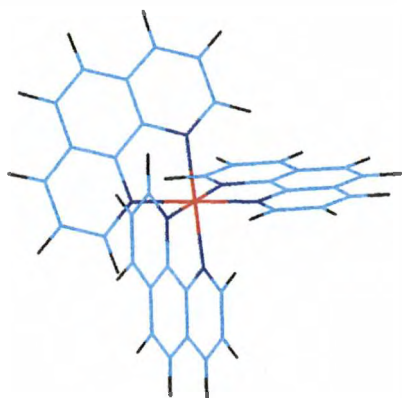
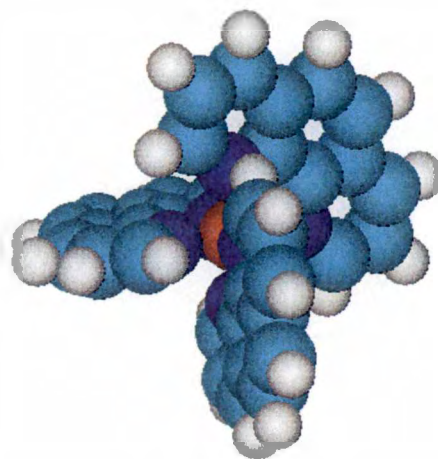
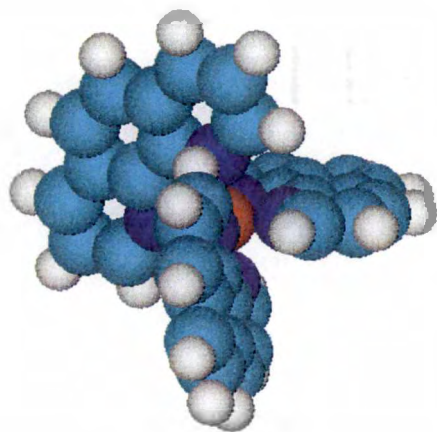


Figure 6. Structures of the l and d forms of the cations showing the propeller shapes of ligands bonded to the central iron atom.

complex possesses  $D_3$  symmetry. An x-ray diffraction measurement of this molecule has shown that the *l*-Fe(phen) $_3^{2+}$  enantiomer is in the form of the left-handed propeller.<sup>39</sup>

The crystal structure for the *l*- and *d*-Fe(phen) $_3$ Sb $_2$ ( $\pm$ )tartrates was examined using a powder x-ray diffraction instrument at the Oak Ridge National Laboratory. The powder sample was placed on a sample holder and suspended in a drop of acetone, which quickly evaporated after application. This sample preparation technique produced uniform sample across the holder as well as consistency between the two enantiomers. The x-ray diffraction patterns (as seen in Figure 7) for both enantiomers were identical to each other as well as to previous literature spectra. Clearly, within the resolution limits of the data, the two enantiomers possess identical crystal structures, which has important implications concerning the validity of the measurement of a parity violating energy difference, i.e., any measured differences in energy are not likely to arise from crystal variations. This topic will be addressed in more detail in a later section.

An important first step towards an attempt to measure a difference in the energies of the two enantiomers of the Fe complex was the characterization of the molecule through various spectroscopies. Since it was necessary to ascertain the exact nature of the chirality of the molecule, a measurement of the circular dichroism and the optical rotatory dispersion was obtained (see Figure 8). This plot clearly shows that the Fe(phen) $_3$ Sb $_2$ (tartrate) is a highly optically active molecule, particularly in the wavelength ranges of 330-400 nm and 420-520 nm. Unfortunately, the precise nature of the relationship between optical activity and the parity violating energy difference has not been firmly established, though it might seem logical to postulate that a larger optical activity might be directly related to a larger PVED.

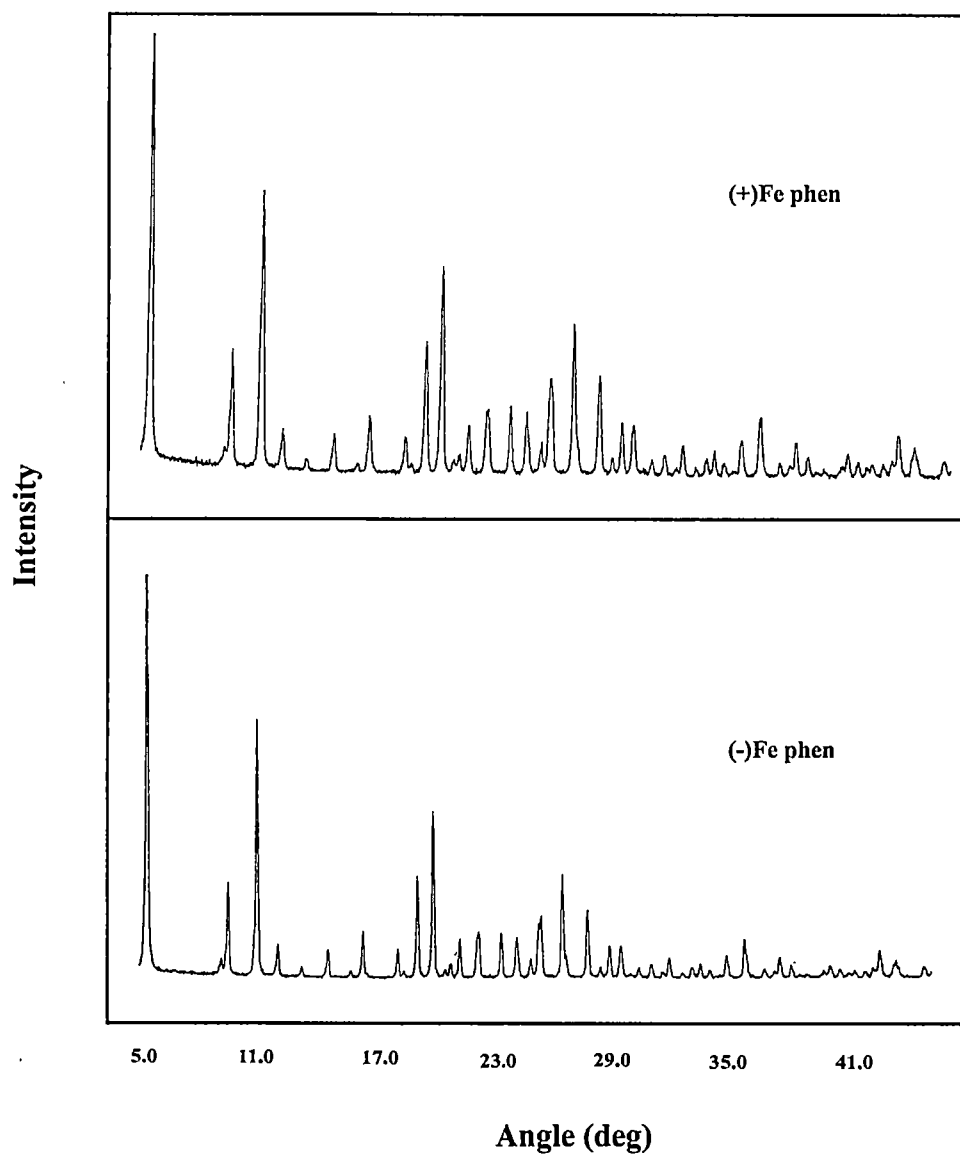


Figure 7. Diffraction patterns for the two enantiomers of the iron complex.

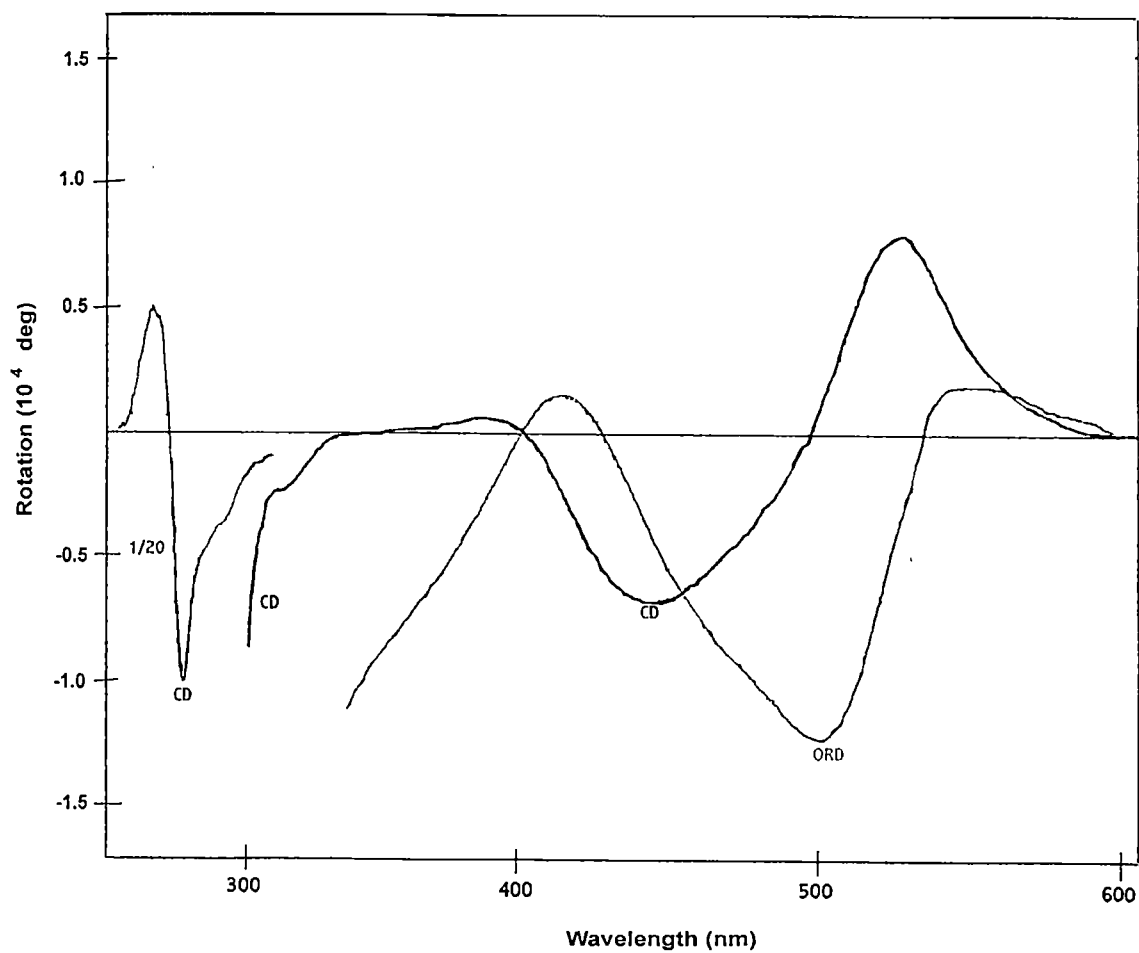


Figure 8. Plot of the circular dichroism (CD) and the optical rotatory dispersion(ORD) for the  $d\text{-Fe(phen)}_3\text{Sb}_2(\text{C}_4\text{H}_2\text{O}_6)_2$ . The mirror enantiomers show the expected opposite CD and ORD.

Despite the large specific rotations exhibited by the Fe complex at wavelengths such as the sodium D line, where the specific rotation is approximately  $\pm 710^\circ$  (depending on which enantiomer is being measured), the two enantiomers are quite unstable with respect to racemization in solution. Figure 9 shows the racemization of *d*- $\text{Fe}(\text{phen})_3^{2+}$  in acetonitrile where the half-life was approximately 2 minutes. The rapid racemization would indicate that the phenanthroline ligands are not strongly bonded to the iron core. This notion is borne out by electrospray ionization and collision induced dissociation studies that were performed on the  $\text{Fe}(\text{phen})_3^{2+}$  ion. From the electrospray data, shown in Figure 10, an important point to notice is that the intensity of the  $\text{Fe}(\text{phen})_3^{2+}$  (which corresponds to  $m/z = 298.1$  amu) peak decreases as the applied voltage (i.e., collisional energy) is increased, thus indicating a weak Fe-phen bond. The mechanism of racemization for coordination compounds containing a central ion has been of considerable interest to researchers. There have been essentially two types of racemization mechanisms that have been considered: (1) a dissociation process, and (2) an intramolecular rearrangement. From kinetic studies, it has been shown that the iron complex racemizes by an intramolecular process since the rate of racemization is more rapid than the rate of dissociation.<sup>40</sup> In particular, the intramolecular pathway involves two successive twists of opposite trigonal faces through an angle of  $60^\circ$ , which is known as a Bailar twist.

The short racemization half-lives present difficulties in performing experiments on the enantiomers in solution (e.g., NMR experiments), unless the experiments are done at low temperatures where the complexes are more stable and possess longer racemization half-lives. However, even at low temperatures, time constraints must be considered since it is



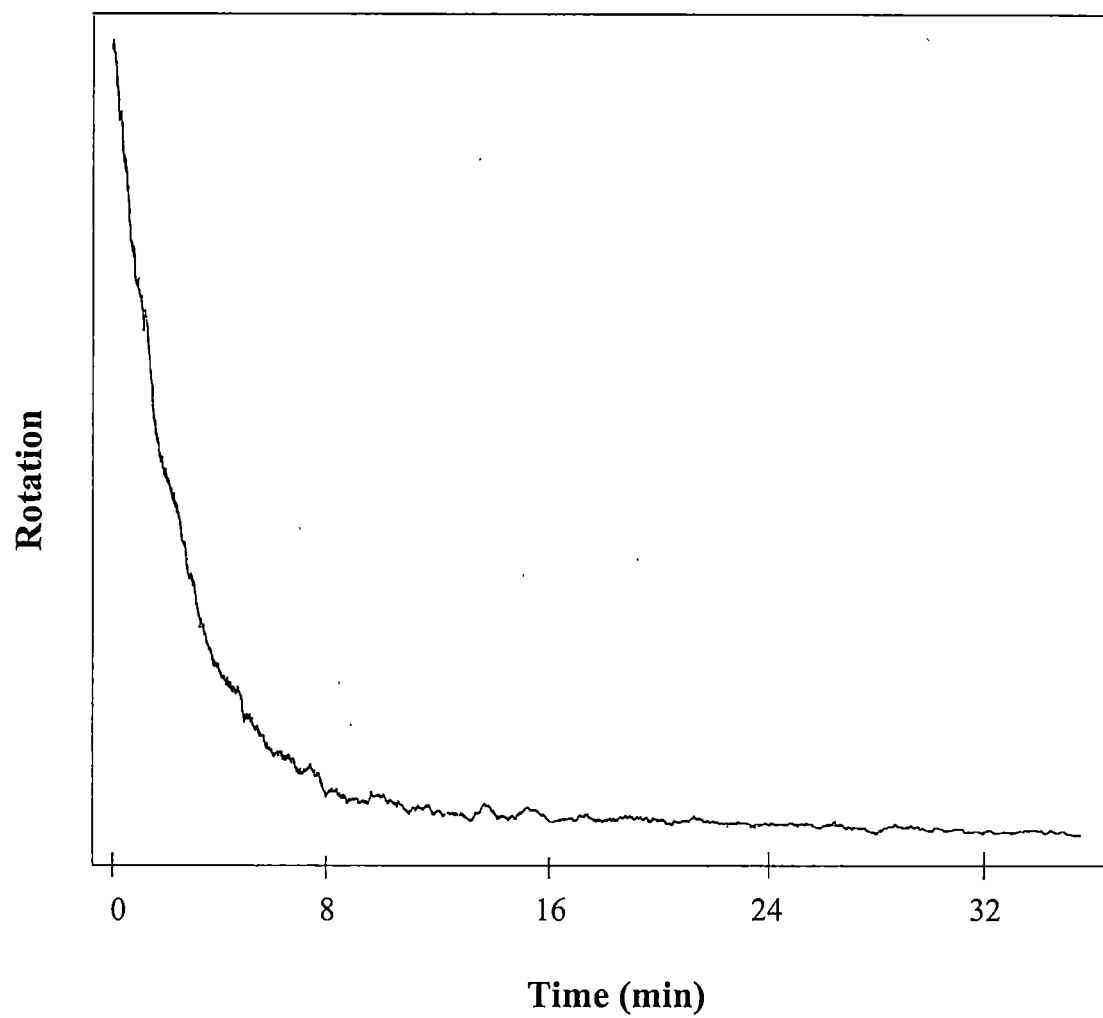


Figure 9. Racemization curve for the Fe complex in acetonitrile.

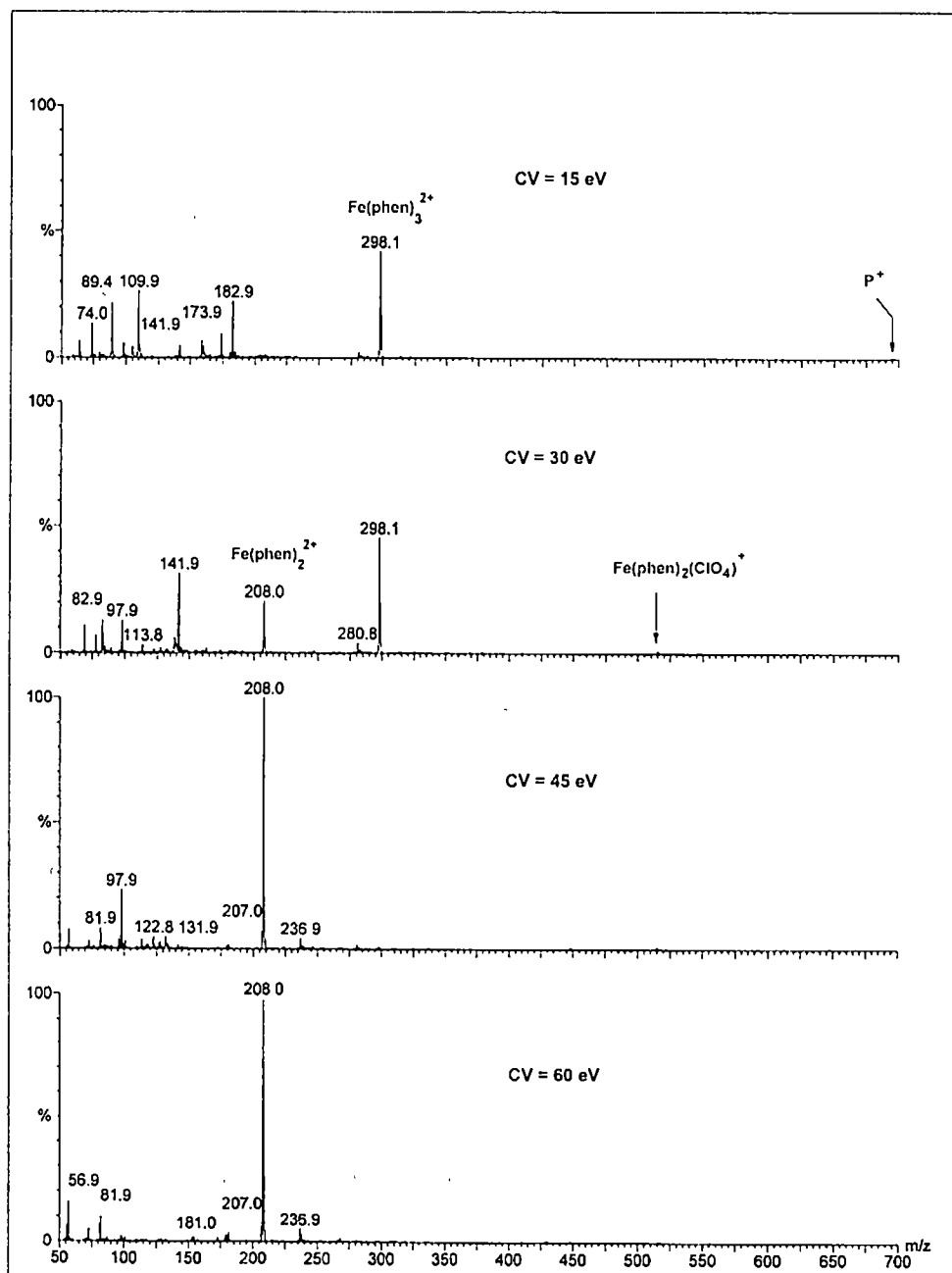


Figure 10. Electro spray time-of-flight mass spectra of the iron complex.

often necessary to acquire measurements over extended periods of time in order to obtain the resolution required to offer even a minute probability of observing the PVED. In addition to the inherent difficulties in doing iron NMR (such as the magnetism of iron which broadens the NMR shift), racemization of the Fe(phen) complex would clearly inhibit measurements of high quality iron NMR spectra of the Fe complexes in solution. An attempt was made to acquire an NMR spectrum of the racemic Fe(phen)<sub>3</sub>(ClO<sub>4</sub>)<sub>2</sub> to ascertain if the abovementioned complications could be overcome. Unfortunately, the NMR experiment yielded no results, most likely for the reasons given above.

### Raman

Since the likelihood of observing any PVED effects in the Raman spectrum of the two enantiomers of the Fe(phen) complex was quite low and there was only a small amount of the two enantiomers available, it was decided to perform the experiment on the racemic mixtures simply to characterize the molecule. Data was taken with a Dilor Raman spectrometer using the 514.5 nm line from a Coherent Argon-ion laser. A novel method of acquiring the spectra, developed by Compton et. al,<sup>41</sup> was employed in which the solid sample was attached to a metal holder using silicon glue then submerged in liquid nitrogen. There are many advantages with this method. The liquid nitrogen prevents the sample from being ablated off the surface of the holder by maintaining a very low temperature with the liquid nitrogen covering. Thus, improved signal-to-noise ratios can be attained as a result of higher laser power without damage to the sample. The low temperature also leads to ro-vibrational cooling and narrower linewidths. The resolution of the spectra shows marked improvement over conventional room temperature Raman spectroscopy. In order to assign the Raman peaks, it was first

necessary to determine if the counter ion possessed any peaks in this region. To that end, Raman spectra were also collected for  $\text{Fe}(\text{phen})_3(\text{ClO}_4)_2$  and  $\text{Fe}(\text{phen})_3\text{I}_2$ . Figure 11 shows the spectra obtained for these two complexes. Clearly, the Raman peaks observed are only due to the  $\text{Fe}(\text{phen})_3^{2+}$  ligand since the peaks are identical for each of the three different counter ions.

### ESCA

Further characterization of the molecule was obtained using electron spectroscopy for chemical analysis (ESCA), or x-ray photoelectron spectroscopy (XPS). ESCA, now widely used as an analytical tool, involves the removal of a core electron from a solid sample using monoenergetic  $\text{MgK}\alpha$  x-rays (1253.5 eV). The binding energy of the electron can be found by determining the kinetic energy of the ejected electron using a hemispherical energy analyzer and by noting that the binding energy is related to the kinetic energy of the electron via the following:

$$\text{KE} = h\nu - \text{BE} - \phi_s \quad (2.16)$$

where  $h\nu$  is the energy of the x-ray, BE is the binding energy of the electron, and  $\phi_s$  is the spectrometer work function. Typically, the spectrometer is calibrated using a gold foil. Unfortunately, measuring the PVED effect using this type of spectroscopy is virtually impossible since it is limited to energy differences of  $\sim 1$  eV.

The iron complex was mixed with toluene and shaken to produce a somewhat homogeneous mixture. It did not dissolve since toluene is a nonpolar solvent while the iron complex is polar. It was important that the compound not be allowed to dissolve since it racemized so quickly in solution. The mixture was placed on a molybdenum sample holder where the toluene was allowed to evaporate leaving the iron complex

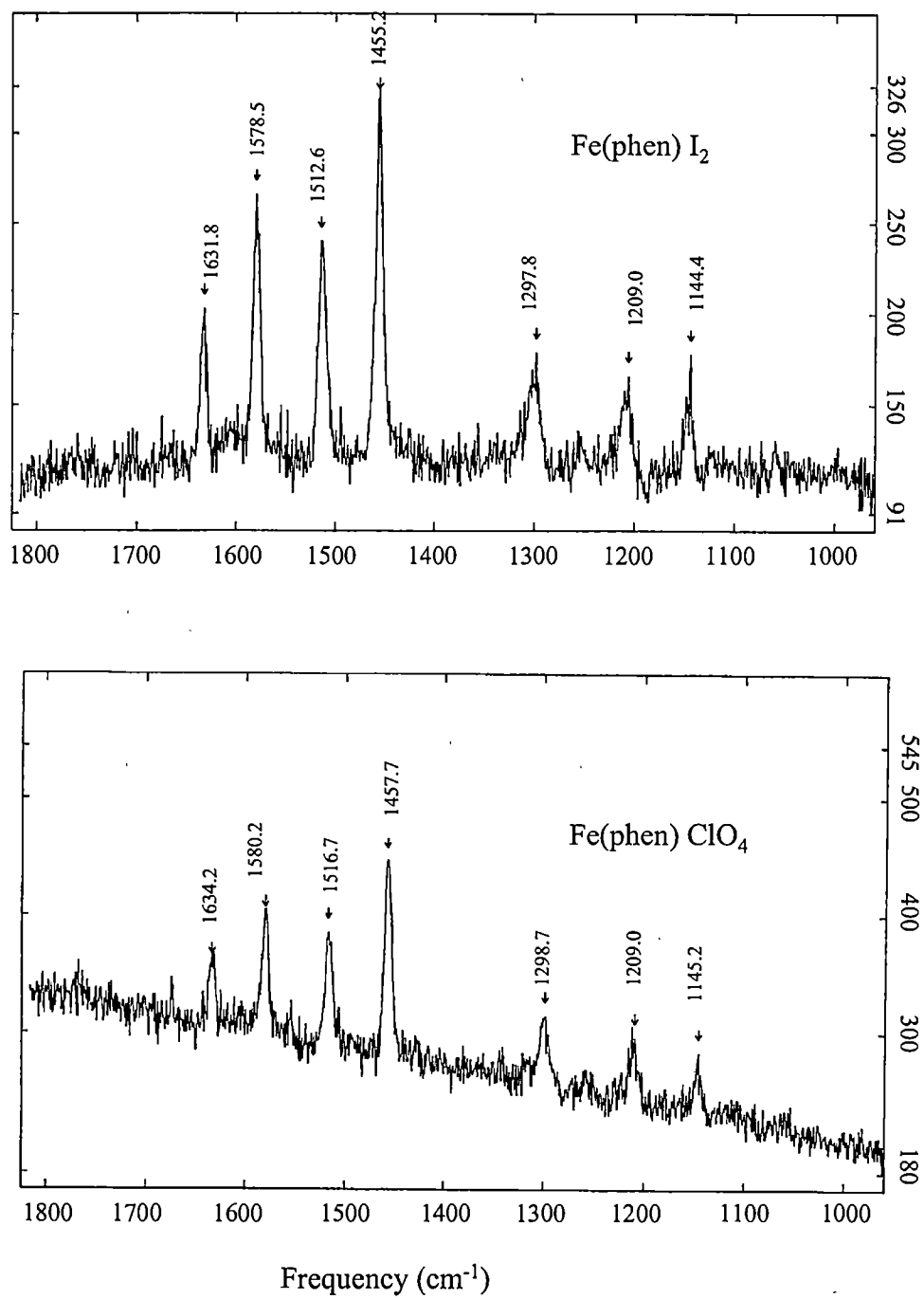


Figure 11. Raman spectra for the iron complex with two different counter ions.

attached to the holder. Data was taken with a Perkin-Elmer model 5100 commercial ESCA instrument. Figure 12 shows the spectra obtained for the two enantiomers. The energies of the  $2p_{3/2}$  peak of iron were measured to be 710.9 eV and were identical for the *l* and *d*  $\text{Fe}(\text{phen})_3(\text{tartrate})$  complexes. Calibration of the instrument was established using gold foil as the standard. During initial attempts to determine the calibration, an interesting phenomenon was discovered. Figure 13 shows the data collected while using gold foil. The accepted value for the gold  $4f_{7/2}$  peak is 83.8 eV which is 1 eV lower than the value presented in the data. The accepted values for the oxygen and carbon peaks are also approximately 1 eV lower than the measured value. The doublet at approximately 100 eV corresponds to a mercury peak. Apparently, a minute amount of mercury vapor from the lab had adsorbed onto the gold foil and was detected using the ESCA apparatus. Due to the atomic makeup of the iron phenanthroline complex, iron, nickel, oxygen, antimony and carbon were expected in the spectrum. From the data, it is clear that this is in fact the case. Adams et al.<sup>42</sup> previously determined the binding energy of the  $\text{Fe } 2p_{3/2}$  peak in the Fe complex to be 706.6 eV which is approximately 4 eV lower than the experimentally determined value presented here. Even when the 1 eV adjustment is made to the data as a calibration based on the position of the gold peak, the experimental value is still 3 eV higher than that previously obtained by Adams et al. As a further test of the sample, it was sent to Oak Ridge National Laboratory where the iron peak was measured to be 711.08 eV, which is  $\sim 6$  eV higher than the value we determined. It should be noted that the literature value of the  $2p_{3/2}$  peak for oxidized iron ( $\text{FeO}$ ) is 710.3 eV. Although a conclusive correlation has not been established, the position of the iron

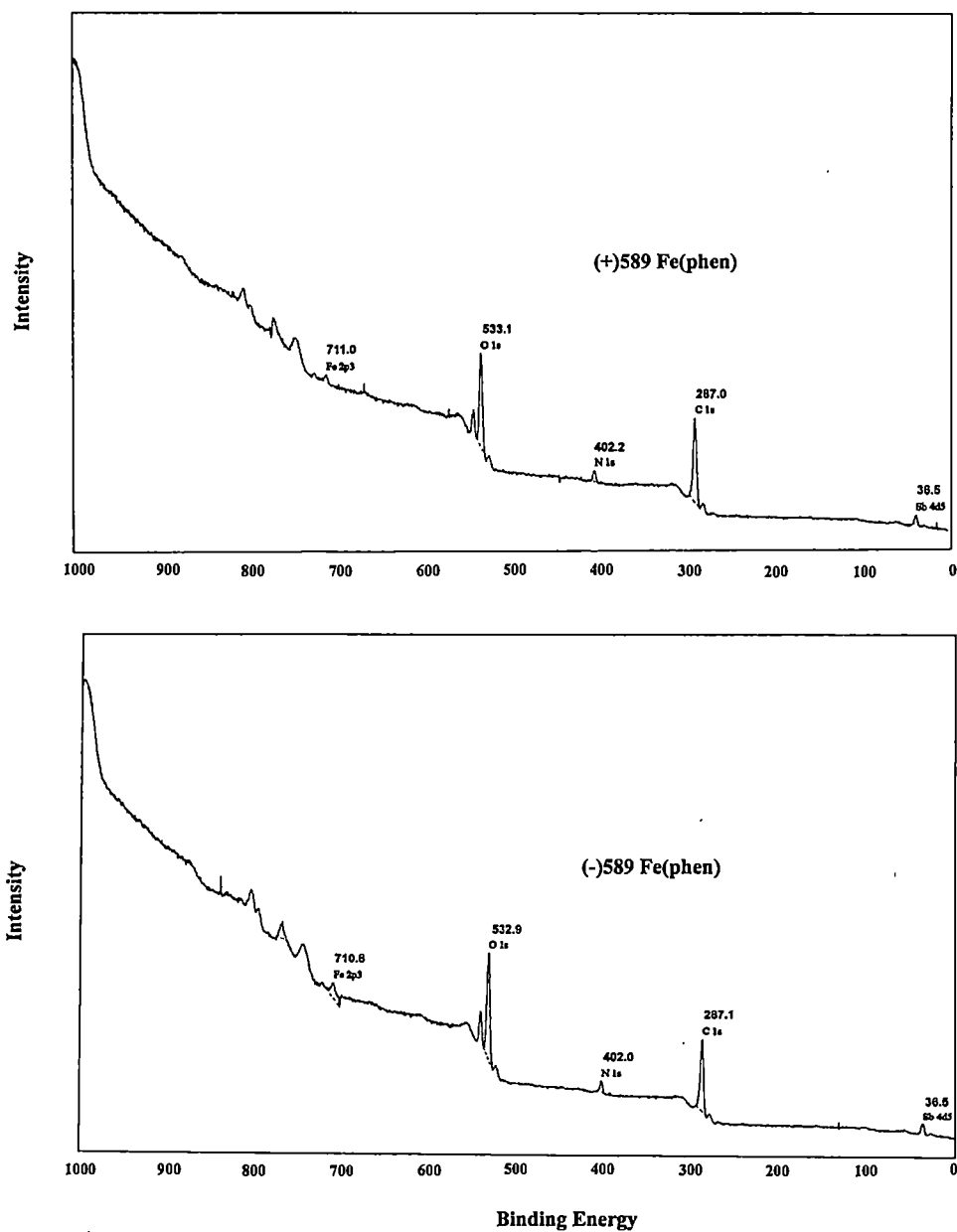


Figure 12. ESCA spectra for the two enantiomers of the iron complex.

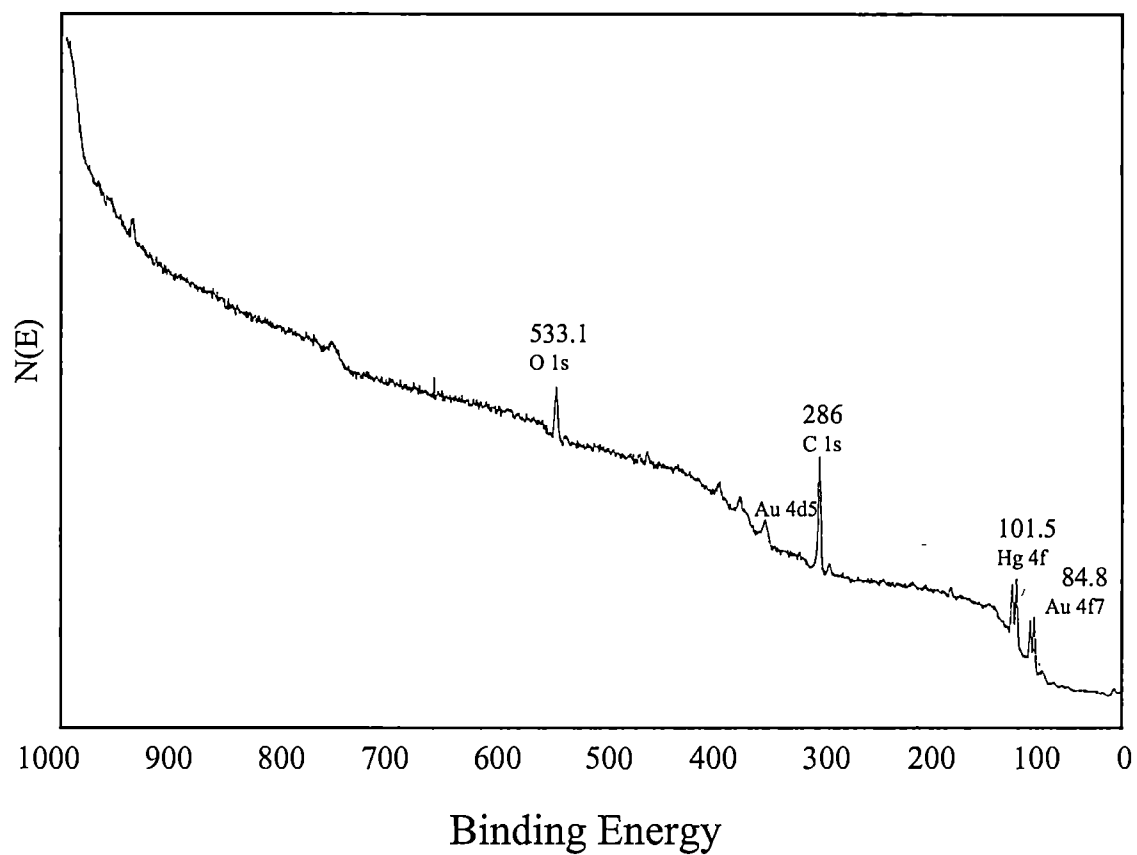


Figure 13. ESCA spectrum for the gold foil used as a calibration (note the mercury peak).



peak could indicate that the iron in the sample has become oxidized by ambient air. There was no significant difference between the energies of the iron peaks for the two enantiomers, which was expected.

### Mössbauer

Mössbauer spectroscopy is a powerful technique which can be used to discern the interactions between orbiting electrons and the nucleus. In Fe Mössbauer spectroscopy, the radioactive source is a  $^{57}\text{Co}$  nucleus which undergoes an electron capture process to decay into an excited state  $^{57}\text{Fe}$  nucleus. From the decay scheme shown in Figure 14, the decay mechanism typically leaves the  $^{57}\text{Fe}$  nucleus in the  $I=5/2$  nuclear excited state, where  $I$  is the nuclear spin of the iron nucleus. The excited iron nucleus then emits gamma rays whose energy depends on which transition occurs. The 14.4 keV gamma ray produced by the transition from the first excited state with  $I=3/2$  to the ground state with  $I=1/2$  is primarily used in iron Mössbauer spectroscopy where the sample to be studied must contain iron. In order to fulfill conservation of momentum, the iron nucleus experiences a certain amount of recoil when the gamma ray is emitted. This momentum gain comes at the expense of a loss of momentum from the gamma ray which serves to alter its energy. A reduction of this effect, known as “recoilless loss,” is obtained by fixing the radioactive  $^{57}\text{Co}$  source in a lattice comprised of rhodium atoms. The 14.4 keV energy of the emitted gamma ray is modulated by applying a “Doppler velocity” of a few mm/s for resonance absorption by the sample. This is achieved by mounting the source on a drive unit that is capable of oscillating the source back and forth at the required speed thus shifting the energy of the gamma ray according to the standard equation for the non-relativistic Doppler shift:

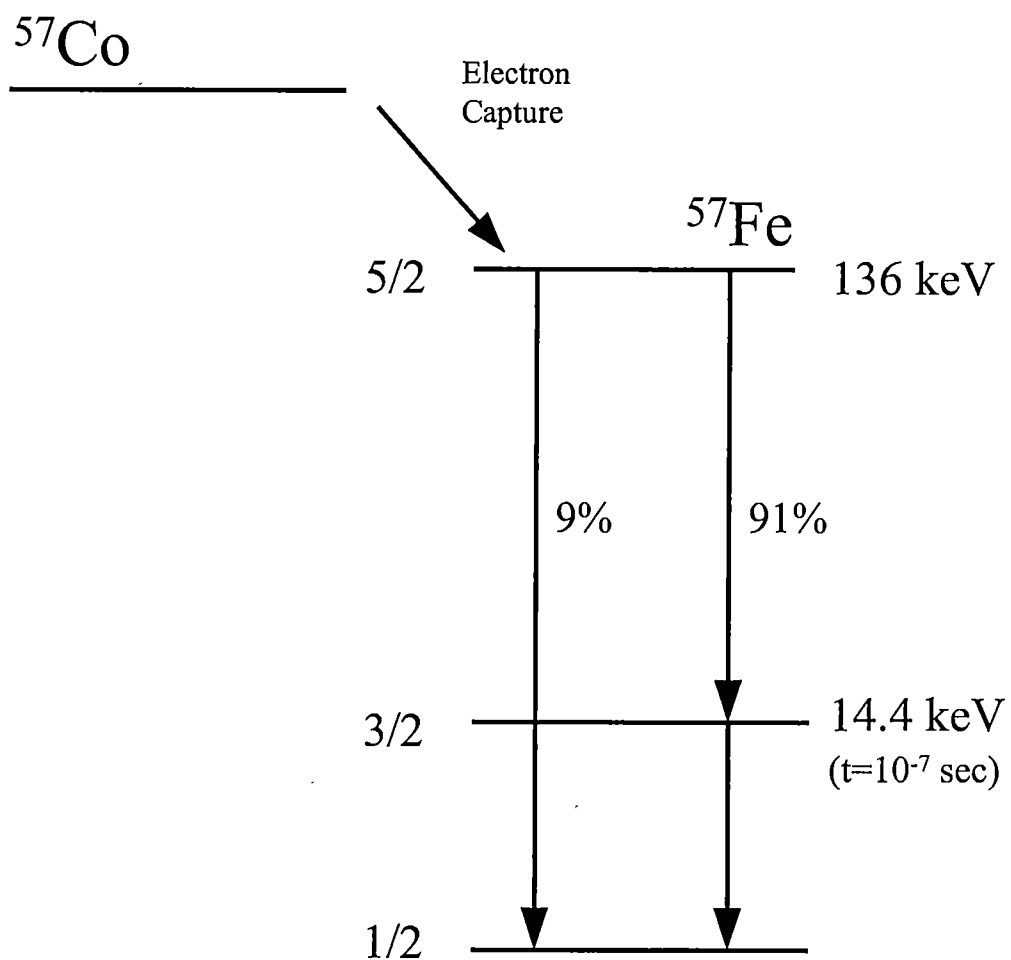


Figure 14. Decay scheme of  $^{57}\text{Co}$  to produce a 14.4 keV gamma ray.

$$E = E_\gamma \left( 1 + \frac{v}{c} \right) \quad (2.17)$$

where  $E_\gamma$  is 14.4 keV and  $v$  is the velocity provided by the drive unit. A plot of the transmitted gamma radiation versus the applied velocity (which corresponds to the changing energy of the gamma ray) constitutes a Mössbauer spectrum. Each energy within the range will be obtained twice, once when the source is moving in the forward direction and once when the source is moving in the reverse direction. If, for example, an absorber has one transition in the energy range, two peaks will be observed which correspond to the two directions of motion. The two peaks are then folded to form one peak. From the Mössbauer spectrum, one can determine (i) the isomer (chemical) shift which is due to the s-electron density at the nucleus, (ii) the quadrupole interaction (splitting) which is due to the interaction between the electric field gradient tensor and the quadrupole moment of the iron nucleus, and (iii) the magnetic hyperfine interactions of the iron site which is due to the electron and nuclear spin interactions. The isomer shift is the quantity of interest since it gives the interaction of the s-electron density with the nucleus and in a chiral molecule the electron density is expected to differ for the two enantiomers. The isomer shift is given by the following equation:

$$\delta = \frac{Ze^2 R^2}{5\epsilon_0} \frac{\Delta R}{R} \left( \left| \Psi_s(0)_{\text{absorber}} \right|^2 - \left| \Psi_s(0)_{\text{source}} \right|^2 \right) \quad (2.18)$$

where  $\Psi_s(0)$  refers to the wavefunction at the center of the nucleus,  $e$  is the electron charge,  $Z$  is the atomic number,  $\Delta R/R$  takes into account any small increments in nuclear size during excitation, and  $\epsilon_0$  is the permittivity of free space.

The use of Mössbauer spectroscopy as a method of measuring PVED effects is quite attractive due to the high resolution attainable as well as to the fact that small variations in the s-electron density at the nucleus possibly as a result of weak interaction effects could be measured. It is particularly important to note that any parity nonconserving effects due to the weak interaction would be felt primarily by the s electrons since these electrons have a larger probability for being at the nucleus and the weak interaction possesses such a short range of influence.

The Mössbauer absorbers were prepared from the *l*- and *d*- enantiomers of the  $\text{Fe}(\text{phen})_3\text{Sb}_2(\text{C}_4\text{H}_2\text{O}_6)_2 \cdot 8\text{H}_2\text{O}$  complexes with densities of the order of 0.1482 mg and 0.1812 mg, respectively. The room temperature  $^{57}\text{Fe}$  Mössbauer effect spectra were obtained using the aforementioned  $^{57}\text{Co}$  in a rhodium matrix source and a Wissel system II constant acceleration spectrometer (see Figure 15) which had an intrinsic linewidth of 0.12 mm/s. The detector consisted of aluminum plates to reduce background x-rays and a proportional counter connected to a multichannel analyzer and computer, where the spectra were collected and analyzed. Each spectrum was accumulated over 2 million counts per channel to ensure high signal-to-noise ratios. Four different experiments were performed over a period of one year. It is important to note that in each set of experiments all conditions of the apparatus remained the same and only the *l* and *d* samples were exchanged.

### Results and Discussion

Room temperature  $^{57}\text{Fe}$  Mössbauer effect spectra observed for the two enantiomers during one trial are shown in Figure 16. The spectra were analyzed using two sets of quadrupole doublets. Spectra were fitted and the isomer shifts of the larger peak for the *l*

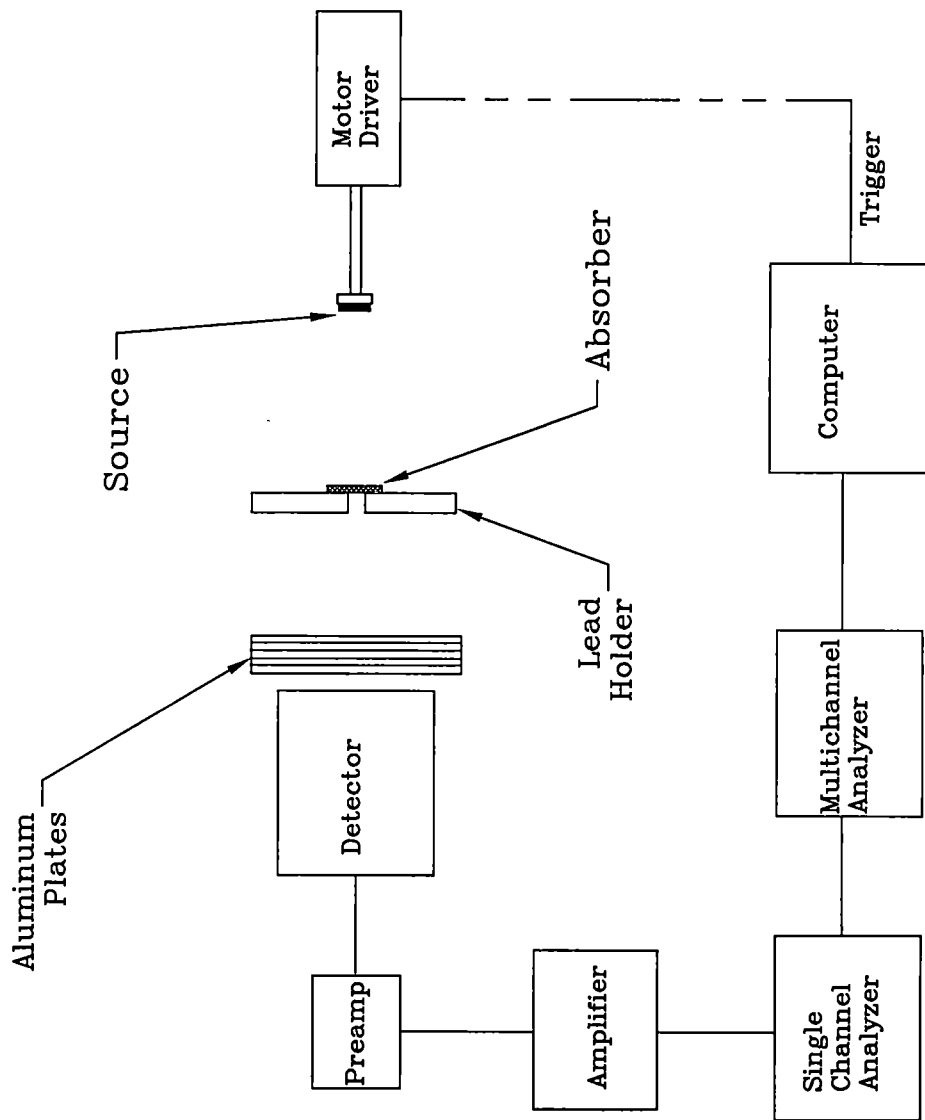


Figure 15. Setup for the Mössbauer experiment.

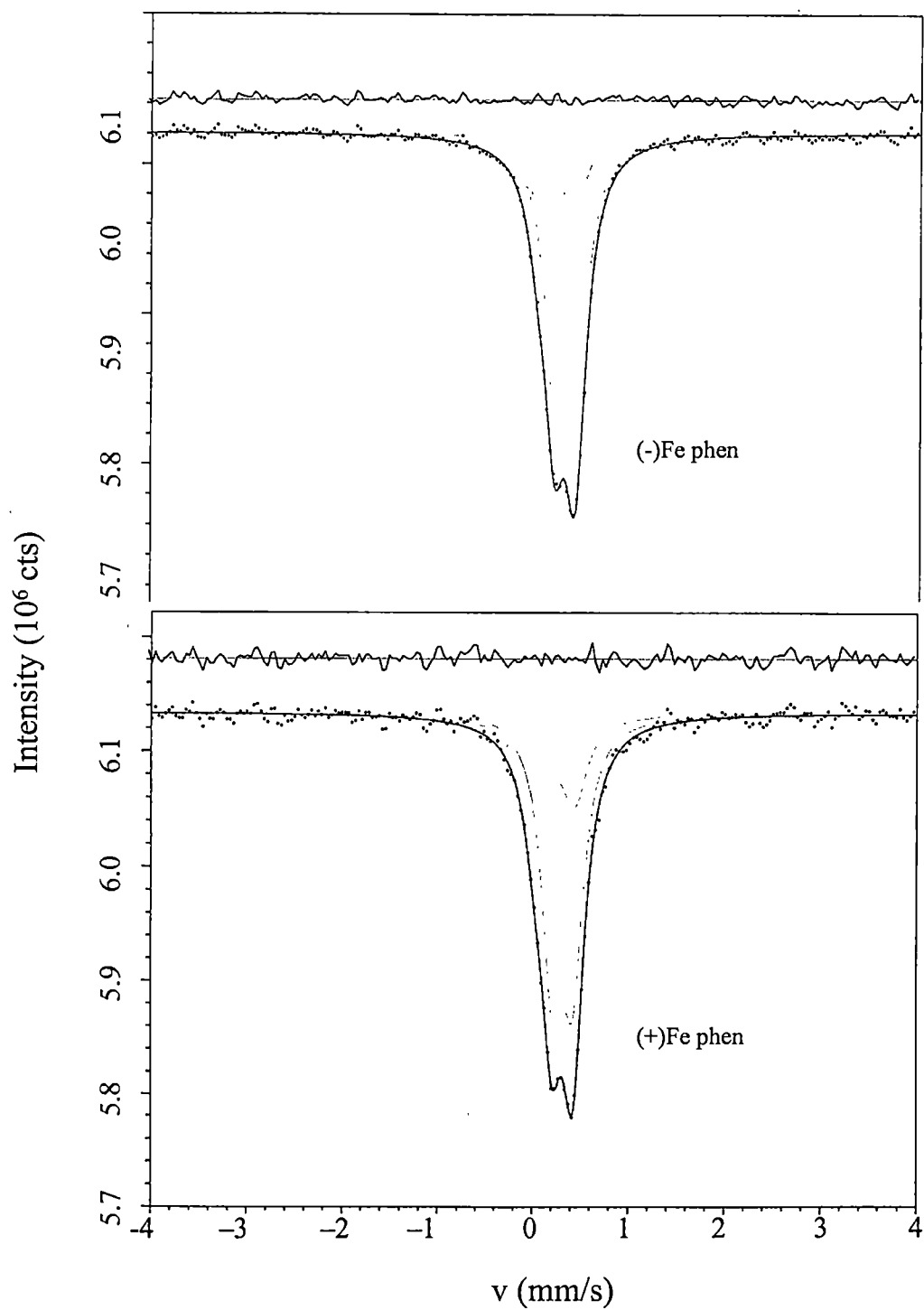


Figure 16. Mössbauer spectra for the two enantiomers of the iron complex.

and *d* enantiomers were compared. The results of the fits to the larger peaks are shown in Table I. Analysis of all the data on the isomer shift of the major peaks yields a difference in their isomer shift of  $.004 \pm .002$  mm/sec (obtained by simply taking the average and standard deviation of the four shifts). This corresponds to an energy difference of  $1.9 \times 10^{-10}$  eV. It is important to note that while this difference is extremely small, with each trial the *d* enantiomer consistently possessed a slightly lower energy than the *l* enantiomer.

An order of magnitude estimate of the PVED of an iron atom can be obtained by applying the  $Z^6$  scaling law in conjunction with the equation derived by Hegstrom [see equation (2.14)]. If the values for the Fermi constant and the fine structure constant are inserted into equation. (2.14), the following equation is obtained:

$$\Delta E_{pV} = 8.5 \times 10^{-21} \eta Z^6 Ryd \quad (2.19)$$

where the  $Z^5$  dependence has been modified to include the new scaling law and the equation is in terms of atomic units. It should be noted that the asymmetry factor,  $\eta$ , is somewhat ambiguous and will vary for each molecule. Since it describes the chiral character of the molecular environment, it seems reasonable to assume that this constant may be related to the optical rotation. For the purposes of an order of magnitude calculation, this constant was taken to be large (approximately unity) since the iron complex displays such a large optical rotation. Plugging in  $Z=26$  for iron and converting to SI units yields  $\Delta E_{pV} \sim 10^{-11}$  eV, which approaches the energy differences found in this study. Any spectroscopic measurement determines the difference in energy levels (see Figure 17). It is thus reasonable to associate this energy shift with the difference in

Table I. Summary of Mössbauer data

Run Number	Enantiomer	$\delta$ (mm/s)	$\delta_l - \delta_d$ (mm/s)
1	<i>l</i>	.3241	.007
	<i>d</i>	.3170	
2	<i>l</i>	.3191	.002
	<i>d</i>	.3174	
3	<i>l</i>	.3160	.005
	<i>d</i>	.3110	
4	<i>l</i>	.3177	.002
	<i>d</i>	.3160	



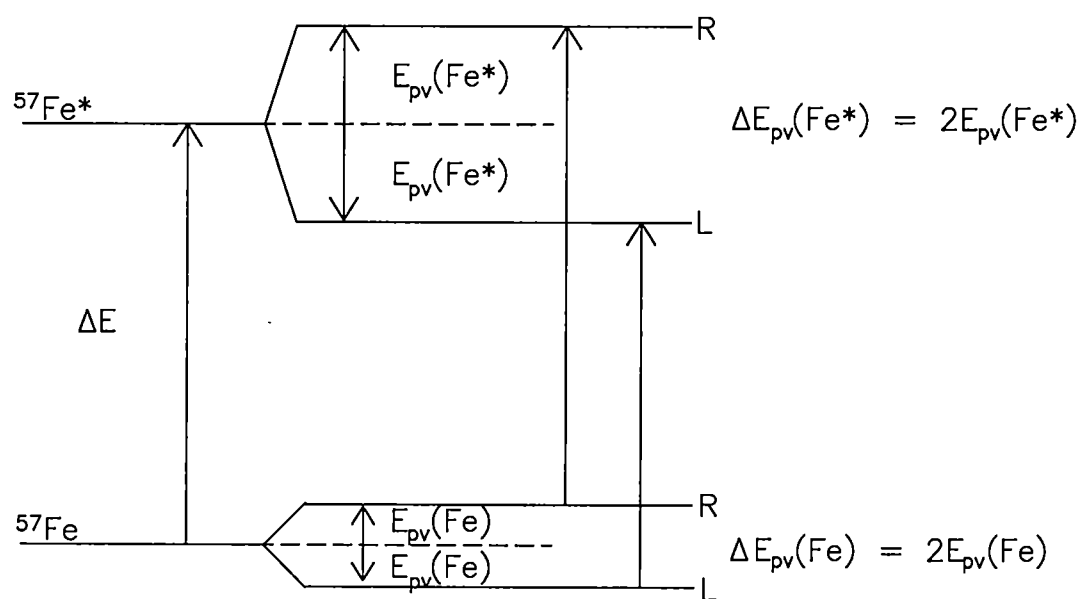


Figure 17. Diagram showing the parity violating energy difference in the two enantiomers of a chiral molecule.

PVED for the two levels. However, initial theoretical considerations place this interpretation in some doubt.

Calculations performed by P. Schwerdtfeger (University of Auckland)<sup>43</sup> show that the PVED for this particular iron complex is expected to be much smaller than the value obtained experimentally since the Fe moiety is a spin doublet. It is therefore unlikely that the difference measured in the Mössbauer spectrum between the two enantiomers is due to PVED effects. The influence of the chiral antimony tartrate counter ion was not considered in the calculation since it would require the inclusion of solid-state effects which is computationally not feasible. The presence of the chiral tartrate anions could conceivably be responsible for this shift through its PVED interaction. Measurements of a racemic mixture of  $[\text{Fe}(\text{phen})_3]^{+2}[\text{ClO}_4]^{-2}$  gave a spectrum very similar to that obtained with the chiral tartrate with an isomer shift of .3220 mm/sec, thus indicating that the counter ion does not appreciably interact with the iron nucleus. It is reasonable to assume then that the small energy difference may be due to some as yet undetermined property of the crystal, though the x-ray diffraction data indicate that the two enantiomers are structurally identical, within the limits of resolution.

Mössbauer spectroscopy represents a unique opportunity to measure the exceptionally small energy differences produced by the chiral weak interaction. At this point, it is not certain that the first parity violating energy difference has been measured. We consider this as a first step toward its measurement. Further steps are under consideration. Since this parity-violating energy difference scales with the atomic number,  $^{119}\text{Sn}$  Mössbauer spectroscopy may be used to measure the energy differences for  $\text{Sn}(\text{phen})_3\text{Sb}_2(\text{C}_4\text{H}_2\text{O}_6)_2 \cdot 8\text{H}_2\text{O}$  enantiomers. The larger Z of the tin would predict an

increase over the present results by a factor of  $\sim 70$  using the  $Z^6$  scaling law making it a prime candidate for a further search for PVED.

## CHAPTER III

## CRYSTALLIZATIONS OF SODIUM CHLORATE AND SODIUM BROMATE

Introduction

Sodium chlorate ( $\text{NaClO}_3$ ) is an achiral ionic molecule consisting of spherical sodium cations and pyramidal chlorate anions of  $C_{3v}$  symmetry that crystallizes in the  $P2_13$  space group which is chiral.  $\text{NaClO}_3$  crystals are optically isotropic, i.e., the magnitude of the optical rotation is independent of the crystal axis. Nearly one hundred years ago Kipping and Pope<sup>44</sup> demonstrated that unstirred crystallizations of sodium chlorate from aqueous solution (which is optically inactive) yielded statistically equal numbers of dextrorotatory and levorotatory crystals, i.e., approximately half the crystals rotated linearly polarized visible light clockwise while the remaining half rotated linearly polarized visible light counterclockwise. For crystals, enantiomeric excess is simply the excess number of levo- or dextro-rotatory crystals, i.e.,

$$\frac{N_d - N_l}{N_d + N_l} \times 100\% \quad (3.1)$$

where  $N_d$  and  $N_l$  refer to the number of dextrorotatory and levorotatory crystals, respectively. The probability distribution of enantiomeric excess is expected to be Gaussian about zero for processes that do not break symmetry. It is instructive to note why a random distribution of levo- and dextro-rotatory  $\text{NaClO}_3$  crystals should form in the absence of any chiral perturbation. Crystallization depends on primary nucleation which occurs in two ways:<sup>45</sup> heterogeneously, where a foreign body such as a speck of dust in the solution induces crystallization of the solute, and homogeneously, where no foreign body induces crystallization. Though poorly understood, homogeneous

nucleation appears to involve two sequential processes: the coming together of solute molecules into a quasi-amorphous state followed by a shift into the primary crystalline nucleus. For non-symmetry breaking crystallizations such as occur with  $\text{NaClO}_3$ , this should produce levorotatory and dextrorotatory crystals with equal probability. Any excess of one hand over the other produced in a particular crystallization experiment is strictly statistical in nature.

Symmetry in crystallizations can be broken in a variety of ways. Kipping and Pope<sup>46</sup> showed that seeding the solution with either dextrorotatory or levorotatory crystals produced substantial enantiomeric excesses. For example, seeding an aqueous solution of  $\text{NaClO}_3$  with dextrorotatory  $\text{NaClO}_3$  crystals produced an excess of dextrorotatory crystals. Enantiomeric excesses of nearly 100% can be achieved simply by seeding the solution with small crystals of the appropriate handedness. Furthermore, Kondepudi<sup>47</sup> showed in an exceedingly simple experiment that symmetry can also be broken by stirring the solution as it crystallized. When the sodium chlorate solution is stirred during the crystallization process, each dish yielded almost entirely levo- or dextro-rotatory crystals (the direction of stirring had no effect on the type of crystal found in the dish). As more dishes were examined, it was noted that the number of levo and dextro rotatory crystals equilibrated, i.e., the enantiomeric excess of the combined dishes was zero.

Kondepudi et al.<sup>47</sup> have developed a model to describe the kinetics of crystallizations including possible symmetry breaking mechanisms. Crystallization is a result of several concurrent processes: primary nucleation (both heterogeneous and homogeneous), secondary nucleation, evaporation, and crystal growth. Secondary nucleation occurs when new crystal nucleation sites are generated from existing crystals. The secondary

sites possess the same handedness as the original crystal. Thus, the handedness of a crystal formed from primary nucleation can be propagated through a localized volume of the solution. Seeding breaks the symmetry of the process by yielding a multitude of primary nucleation sites of identical handedness (the seed crystals) that are propagated via secondary nucleation. Stirring alone, however, is not sufficient to produce an excess of primary nucleation sites of one handedness. There is an equal probability for levo- and dextro-rotatory crystals to be formed during the primary nucleation process when there are no chiral perturbations and secondary nucleation simply builds on crystals that are already present. Hence, there must be a second aspect of stirring that breaks the symmetry. Kondepudi<sup>47</sup> postulated that there must be competition between the two enantiomeric crystals such that the formation of one suppresses the formation of the other. This competition is achieved through the dependence of nucleation rates on saturation.

The rate of primary nucleation for l and d crystals,  $P_l$  and  $P_d$ , was derived by Randolph<sup>48</sup> and is given by:

$$P_l = P_d = B \exp \left[ \frac{-16\pi N_A \sigma_B v^2}{3(RT)^3 [\ln(C/C_s)]^2} \right] \quad (3.2)$$

where B is a constant that depends on the number of nucleation sites,  $N_A$  is Avogadro's number,  $v$  is the molar volume of the solid, R is the gas constant, T is the temperature,  $\sigma_B$  is a surface energy constant, C is the concentration expressed as a molar ratio, and  $C_s$  is the concentration at saturation. Randolph has further suggested that the rate of secondary nucleation is given by:

$$S_i = s \sigma_i K_s (C - C_s)^\alpha \quad (3.3)$$

where  $s$  is the rate of stirring,  $\sigma_i$  is the surface area of either  $l$  or  $d$  crystals,  $K_s$  is a temperature dependent constant, and  $\alpha$  is a constant that depends on the compound. Stirring tends to reduce the concentration of the solution more quickly since it affects the evaporation rate as well as the rates of primary and secondary nucleation. Thus, stirring effectively breaks the symmetry of crystallization through competition via secondary nucleation once a primary nucleation site has formed.

In this thesis, a third method that used polarized electrons and positrons from radioactive decay to break the symmetry in sodium chlorate crystallization will be described. Mechanisms of symmetry breaking will be described, including bremsstrahlung and possible stirring effects.

In addition to experiments with sodium chlorate, sodium bromate, which is a molecule that is quite similar to sodium chlorate in that it also is an achiral molecule that crystallizes in the  $P2_13$  space group, was also crystallized. It is interesting to note that the sodium bromate and sodium chlorate crystals that have the same direction of optical rotation have opposite absolute configurations.<sup>49</sup> Thus, seeding aqueous  $\text{NaClO}_3$  solutions with dextrorotatory  $\text{NaBrO}_3$  crystals yielded predominantly levorotatory  $\text{NaClO}_3$  crystals, while seeding with levorotatory  $\text{NaBrO}_3$  crystals produced an excess of dextrorotatory  $\text{NaClO}_3$  crystals. Due to the similarities between sodium chlorate and sodium bromate it is expected that equal numbers of dextrorotatory and levorotatory crystals should be produced in a crystallization experiment. However, an unexpected bias in the crystallization of sodium bromate will be presented along with possible explanations.

## Experimental

Sodium chlorate and sodium bromate (shown stereographically in Figure 18) were obtained from Aldrich and used without further modification. Solutions were prepared by dissolving  $\text{NaClO}_3$  and  $\text{NaBrO}_3$  in high purity, research grade water well below the saturation limit. In a typical experiment, approximately 70 g of  $\text{NaClO}_3$  was dissolved in 100 mL of HPLC water, while 15 g of  $\text{NaBrO}_3$  was dissolved in 100 mL of HPLC water. In order to ensure that the solution was homogeneous and there were no small crystals present, the solution was stirred and heated at approximately  $40^\circ\text{C}$  for 2 hours.

Once solutions were prepared, they were placed in clean Petri dishes where the water was allowed to evaporate at room temperature ( $\sim 20^\circ\text{C}$ ) with no stirring. Evaporation to complete dryness generally required two to three days. The crystals were then removed with forceps and placed in a second Petri dish where the direction of rotation was determined with a polarimeter. The polarimeter consisted of a light bulb and two sheets of polarizing film. One sheet was placed above the white light source to act as a simple polarizer and the second sheet was used as the analyzer. The crystal was placed on the first polarizing sheet. The second polarizing sheet was oriented above the crystal and rotated such that no light passed through the two polarizing films (see Figure 19). By rotating the second polarizer with respect to the first one, it was a simple matter to determine which direction the crystal rotated the plane of polarization, either clockwise or counterclockwise. By convention, a crystal that rotates the light counterclockwise is designated levorotatory while a crystal that rotates the light clockwise is dextrorotatory. It should be noted that the reason white light can be used in place of monochromatic light in the polarimeter for the sodium chlorate and sodium bromate crystals is that the optical



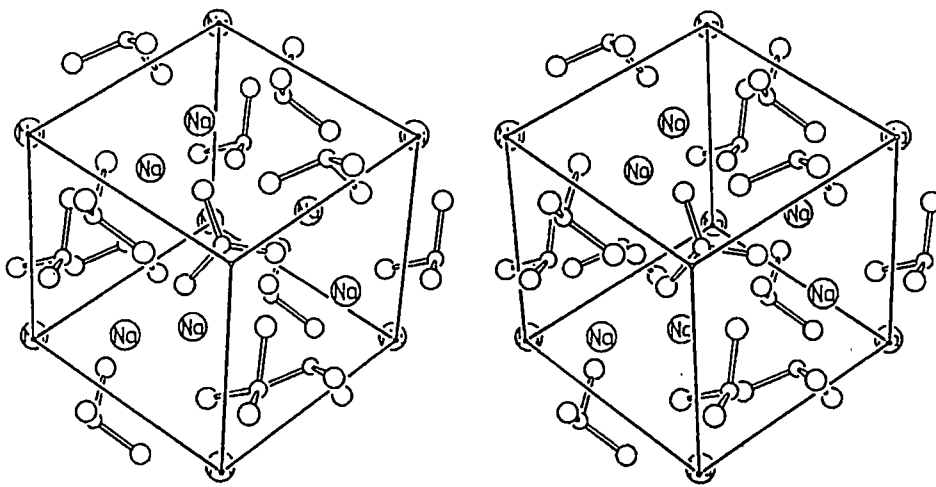
Sodium Chlorate/Bromate  $P2_13$ Sodium Chlorate/Bromate  $P2_13$ 

Figure 18. Stereographic view of the sodium chlorate and sodium bromate crystals.

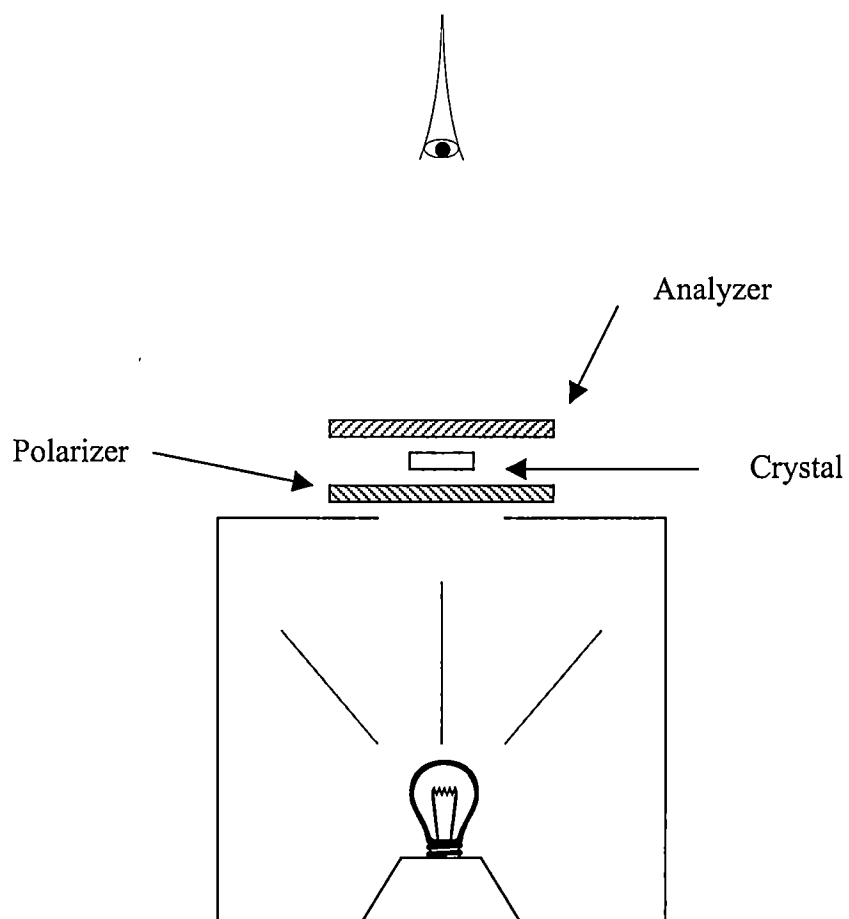


Figure 19. Setup used to determine the handedness of  $\text{NaClO}_3$  and  $\text{NaBrO}_3$  crystals.

rotatory dispersion curve does not change sign in the visible region of the spectrum (it follows a normal curve).

The effects of beta radiation on the crystallizations of sodium chlorate and sodium bromate were determined by allowing the solutions to evaporate to dryness under a strong beta emitter. The beta source was  $\text{Sr}^{90}$  which has a half-life of 28.1 years and yields polarized electrons with 0.546 MeV of energy.  $\text{Sr}^{90}$  decays to  $\text{Y}^{90}$  which has a half-life of 64 hours and emits beta particles with 2.27 MeV of energy. The activity of the  $\text{Sr}^{90}$  source was  $1.6 \times 10^9$  Bq. The beta source was approximately 12 cm above the Petri dishes in which the crystallizations occurred. Figure 20 shows the setup for crystallizations under the beta source. The effects of positron radiation were studied using a  $\text{Na}^{22}$  source (half-life was 2.602 years) with an activity of  $10 \times 10^7$  Bq. The source emitted positrons with energies of .54 MeV. Due to parity violation in the weak interaction, electrons and positrons are spin polarized when they are emitted, and the degree of polarization is dependent on the energy. For the beta source used in this study, approximately 80% of the electrons are left-handed, i.e., the spin vector is anti-parallel to the momentum vector.

### Results and Discussion

In order to confirm the accuracy of previous experiments and to have a set of controls, a series of twenty-four dishes were allowed to crystallize at room temperature in the absence of stirring. The solution was unfiltered and, with the exception of using clean Petri dishes, no special precautions were taken to remove foreign particles. Table II shows the results for these initial crystallizations. As was expected, the unstirred

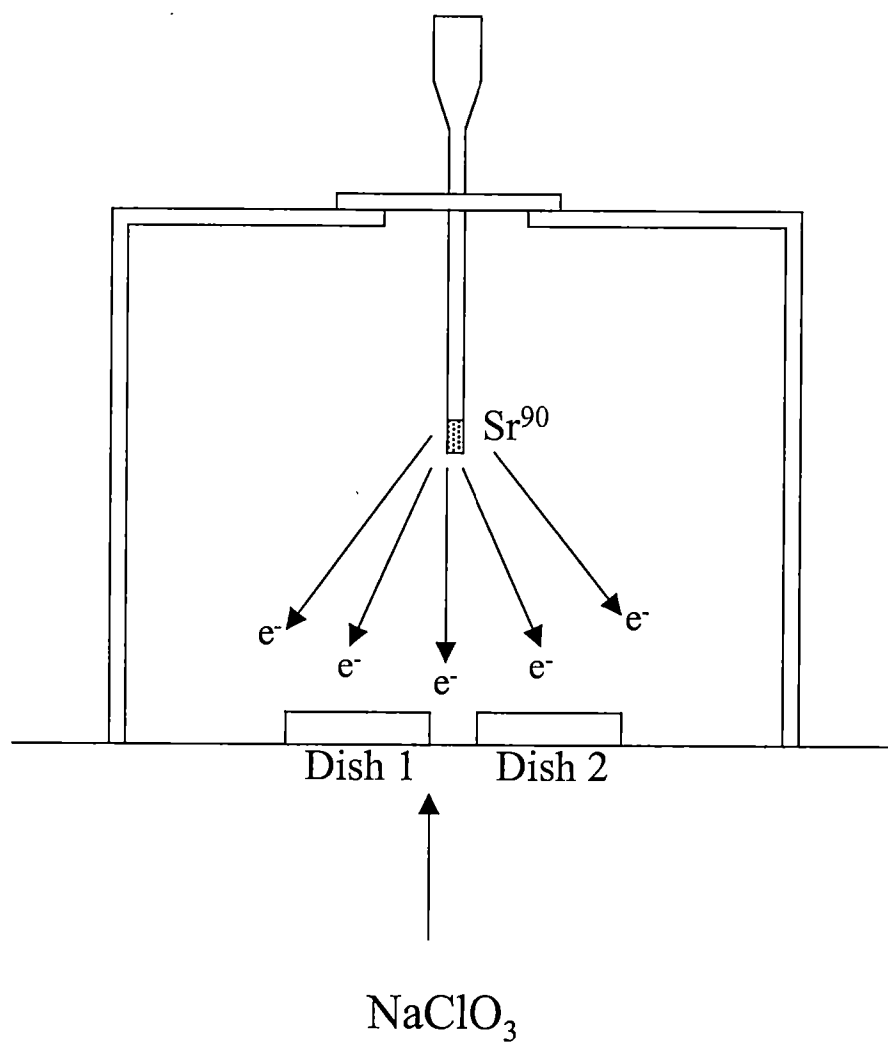


Figure 20. Diagram of the experimental setup used to study the effect of beta radiation on the crystallization of  $\text{NaClO}_3$  and  $\text{NaBrO}_3$ .

Table II. Unstirred crystallizations of sodium chlorate.

Dish	Clockwise	Counter Clockwise	Enantiomeric Excess
1	21	43	-34.4
2	34	17	33.3
3	54	15	56.5
4	6	34	-70
5	12	42	-55.6
6	34	39	-6.8
7	16	16	0.0
8	8	23	-48.4
9	34	15	38.8
10	12	13	-4.0
11	5	19	-58.3
12	13	14	-3.7
13	18	29	-23.4
14	34	37	-4.2
15	16	22	-15.8
16	23	28	-9.8
17	14	29	-34.9
18	26	16	23.8
19	13	13	0.0
20	11	15	-15.4
21	22	18	10.0
22	10	15	-20.0
23	23	16	17.9
24	21	21	0.0
Total	480	549	-6.7

crystallizations produced nearly equal numbers of dextro- and levo-rotatory crystals. Figure 21 presents the data as a histogram of frequency with which an enantiomeric excess occurred versus its enantiomeric excess. The histogram shows a nearly Gaussian distribution, with the dishes yielding excesses of approximately zero being the most frequent. A scatter plot (Figure 22) shows each dish presented as enantiomeric excess. The data show a random distribution about zero which demonstrates the random and statistically equivalent nature of homogeneous primary nucleation.

A similar control experiment was performed with sodium bromate. The results are shown in Table III. In this case, the crystallizations did not yield the expected equal numbers of dextro and levorotatory crystals. There is a substantial bias towards dextrorotatory crystals, as is more clearly shown in the histogram (Figure 23). At this point, the source of the bias, though evidently quite strong, is unclear. The bromate crystallizations were performed in an identical manner as the chlorate crystallizations. Once again, no special precautions were taken to remove impurities. However, NMR spectra were taken of the bromate samples and no chemical impurities were found. In order to see if the particular lot had been contaminated with chiral particulates, new samples were ordered from Aldrich Chemical Company. The results were the same, i.e., all dishes produced almost exclusively dextrorotatory crystals. Furthermore, sodium bromate samples, purchased from other companies, also exhibited the same bias. Whatever the chiral influence, the effect is clearly much stronger in the bromate crystallizations than in the chlorate crystallizations since the two experimental methods were identical.

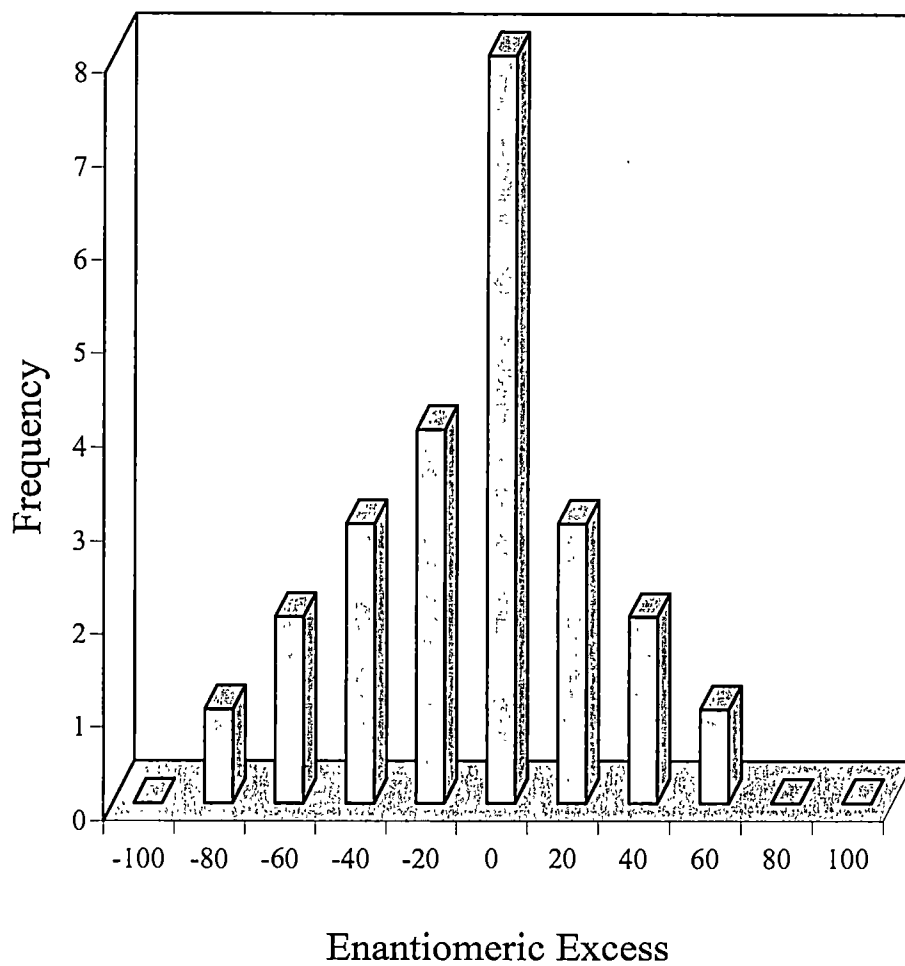


Figure 21. Histogram of the unstirred crystallizations of NaClO<sub>3</sub>.

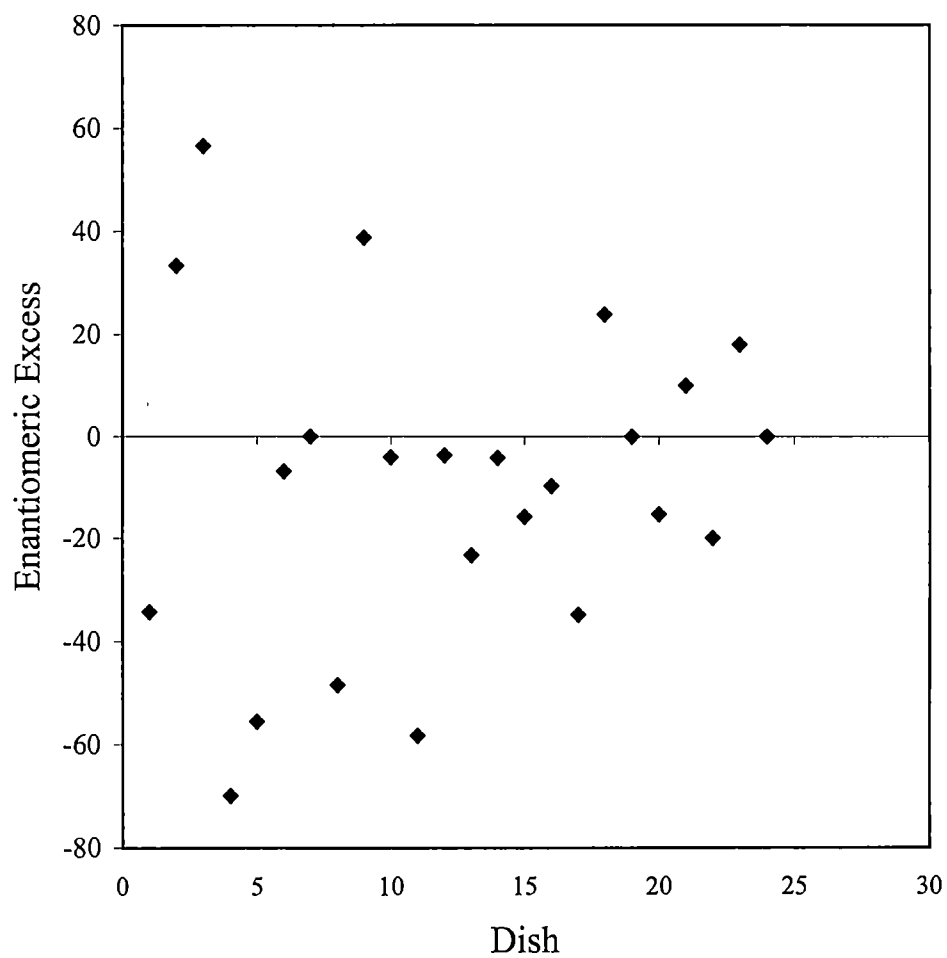


Figure 22. Scatter plot of the crystallizations of NaClO<sub>3</sub> showing the random nature the primary nucleation.



Table III. Unstirred crystallizations of sodium bromate.

Dish	Clockwise	Counter Clockwise	Enantiomeric Excess
1	53	1	96.3
2	49	1	96.0
3	52	0	100
4	34	0	100
5	66	0	100
6	23	2	84.0
7	41	0	100
8	13	0	100
9	31	4	77.1
10	17	3	70.0
11	34	0	100
12	23	22	2.2
13	18	4	63.6
14	17	0	100
15	42	3	86.7
16	15	8	30.4
17	57	0	100
18	21	0	100
19	98	0	100
20	63	0	100
21	112	1	98.2
22	61	0	100
23	131	1	98.5
24	108	13	78.5
Total	1179	63	89.9

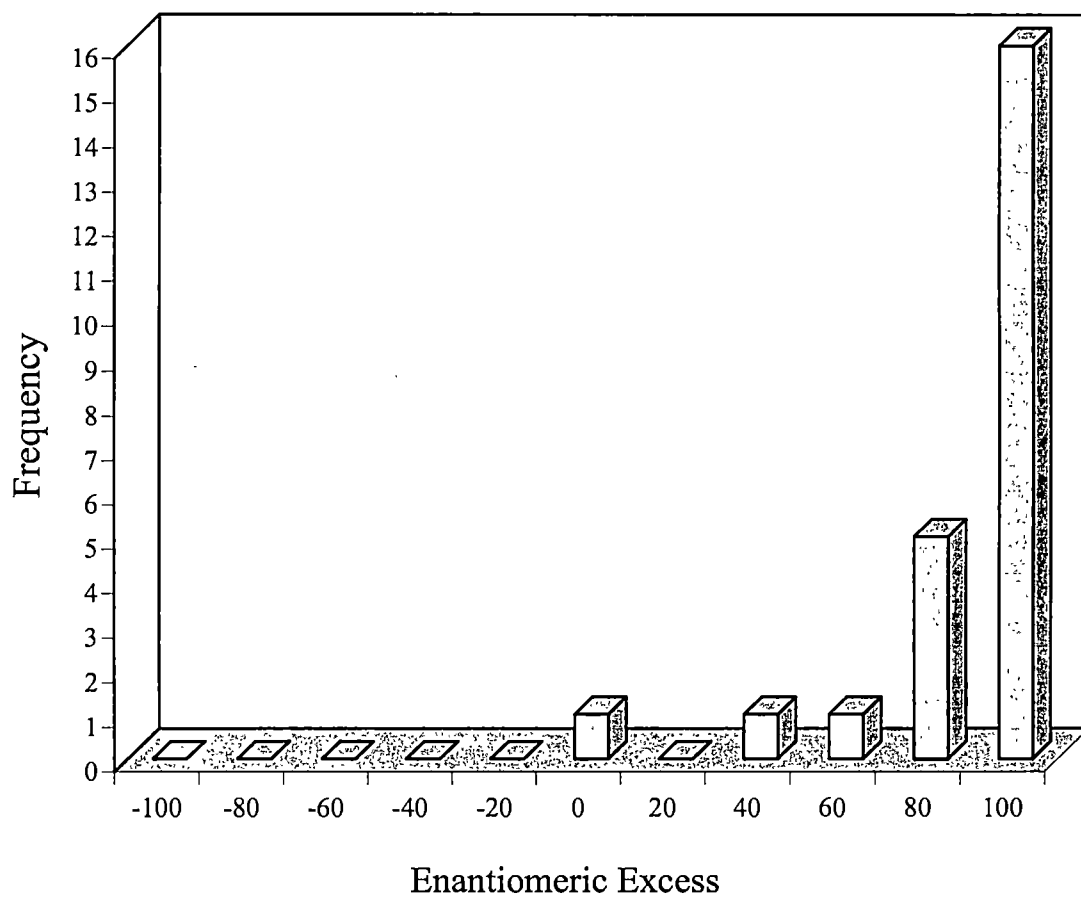


Figure 23. Histogram of the unstirred crystallizations of NaBrO<sub>3</sub>.

It is interesting to note that the bromate has a higher atomic number than the chlorate at the chiral center and the parity violating energy difference has a  $Z^6$  dependence. It has also been pointed out that crystallizations can amplify this difference.<sup>50</sup> Despite the amplification produced by crystallization, it is rather unlikely that the bias observed in the crystallizations of sodium bromate is due to parity violation in part since the molecule itself is achiral. The most feasible explanation is that some chiral impurity has been introduced into the sample that influences the crystallization.

Over the course of two years, a total of sixty-one dishes of sodium chlorate were crystallized under the beta source at Oak Ridge National Laboratory under the direction of Jim Bogard. The results are presented in Table IV. A bias of approximately 33 per cent towards the formation of dextrorotatory crystals was measured in these crystallizations. It should be pointed out that twenty-four of the dishes were crystallized by Mike McGinnis under a slightly weaker beta source. From the histogram of the data (see Figure 24), there are two effects that warrant discussion. First, the data appear to be skewed towards enantiomeric excesses of either +100 or -100, i.e., there is no longer a Gaussian shape to the data. This is somewhat reminiscent of Kondepudi's stirring experiment in that approximately half of the dishes were predominantly one hand or the other, rather than most dishes producing equal numbers of each hand. It therefore seems reasonable to conclude that the beta particles were heating the solution to produce convection. One can obtain a crude idea of the temperature increase by assuming that the beta particles lose all their energy (.54 MeV) to heating. The change in temperature is related to the energy through the equation:

$$E = mc\Delta T. \quad (3.4)$$

Table IV. Sodium chlorate crystallizations under Sr<sup>90</sup> source.

Dish	Clockwise	Counter Clockwise	Enantiomeric Excess
1	14	4	55.6
2	29	23	11
3	13	22	-25.7
4	17	2	78.9
5	2	4	-33.3
6	7	0	100
7	0	9	-100
8	25	0	100
9	25	0	100
10	11	0	100
11	11	0	100
12	17	6	47.8
13	20	12	25.0
14	20	7	48.1
15	21	6	55.6
16	12	0	100
17	21	0	100
18	13	0	100
19	20	1	90.5
20	30	23	13.2
21	29	27	3.57
22	14	13	3.70
23	39	16	41.8
24	13	3	62.5
25	15	0	100
26	15	0	100
27	19	0	100
28	10	1	81.8
29	0	10	-100
30	0	12	-100
31	2	4	-33.3
32	13	7	30.0
33	14	6	40.0
34	11	26	-40.5
35	11	12	-4.34
36	13	5	44.4
37	8	13	-23.8
38	1	0	100
39	7	0	100
40	21	0	100

Table IV. Continued

41	31	1	93.8
42	39	0	100
43	50	50	0
44	50	50	0
45	55	0	100
46	50	50	0
47	39	0	100
48	48	0	100
49	0	39	-100
50	28	10	47.4
51	24	4	71.4
52	62	2	93.8
53	0	51	-100
54	33	7	65
55	25	0	100
56	1	0	100
57	1	20	-90.5
58	1	0	100
59	28	0	100
60	27	27	0
61	1	9	-80
Total	1176	594	32.9

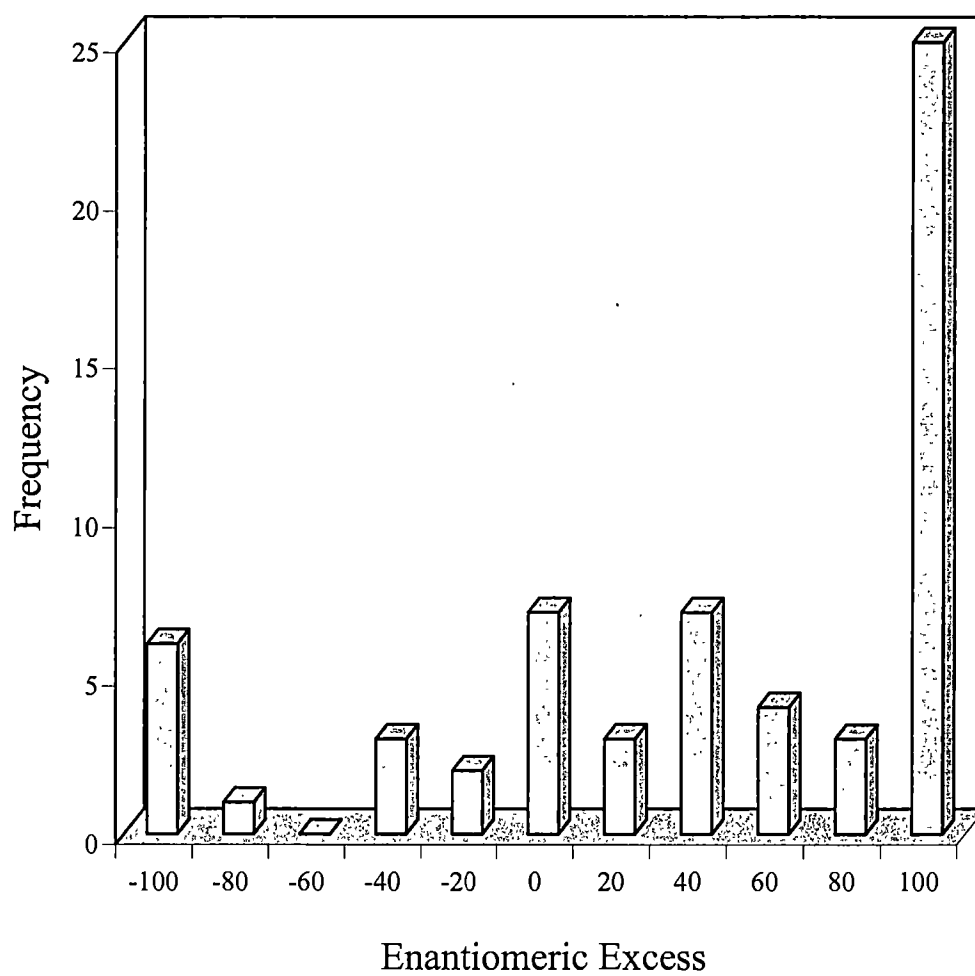


Figure 24. Crystallizations of NaClO<sub>3</sub> under the influence of a 41 mCi Sr<sup>90</sup> beta source.

The range of .54 MeV electrons in water is approximately  $R=.1$  mm and is strongly dependent on the electron's energy. If the specific heat and density of water are taken to be  $c=3900$  J/kg·K and  $\rho=1024$  kg/m<sup>3</sup> (where these values are for seawater since that more closely approximates a sodium chlorate solution), then the localized heating of the solution, or the heating that occurs within the volume of the electron's path, can be estimated by noting that for one electron the path radius can be approximated by the Bohr radius ( $r=.529$  Å). The mass of water that is heated by the single electron can then be determined from the density and the volume (where the volume is simply given by  $V=\pi r^2 R$ ). Inserting these values into equation (3.4) yields a temperature increase of  $2.5 \times 10^4$  °C, which is a substantial increase. This value is exaggerated since the energy lost by the electron will be quickly dissipated in the solution. A more realistic value can be obtained by using the entire surface of the solution in the Petri dish and noting that the activity of the beta source is  $1.6 \times 10^9$  electrons/sec. If the mass of water to be heated is calculated using the radius of the Petri dish ( $r_p=.044$ m) and the range of electrons in water ( $R=.1$ mm), the temperature increase becomes  $\Delta T = .00006$  °C/sec. If one assumes that all the energy lost by the beta particles goes into heating, this value translates into a temperature increase of .2 °C/hour. Though the above treatment is an over estimation and represents only a maximum temperature effect, it nonetheless provides some validation of a stirring mechanism produced by heating, particularly in the localized volume of the electron's path in the solution.

The second point to notice is that the total number of crystals show an enantiomeric excess of +33, which cannot be explained by a simple stirring mechanism since in Kondepudi's stirring experiments the total data showed no enantiomeric excess. The

stirring simply propagates the primary nucleation, which has an equal probability of producing levo- or dextro-rotatory crystals, throughout the solution. The histogram shows that the frequency of producing +100 was four times that of producing -100. As was previously pointed out, approximately 80% of the beta particles are left-handed as a result of parity violation in beta decay (mediated by the chiral weak interaction). A possible mechanism is that the spin polarization of the beta particles influences the formation of dextrorotatory crystals during primary nucleation through the emission of radiation as will be discussed later. These dextrorotatory nucleation sites are then propagated as a result of stirring caused by a heating of the solution. It should be pointed out that a few experiments yielded excesses of nearly zero. These may be indicative of crystallizations in which primary nucleation was not influenced by the polarized beta particles, or that there were simultaneous influences of the left- and right-handed spin polarized electrons which were then propagated throughout the solution.

In order to validate the data, i.e., to ensure that there were no spurious influences within the building that housed the beta source, a set of controls were performed. Nineteen dishes were crystallized under identical conditions with the only difference being the absence of the beta source. The results are shown in Table V. The data show a somewhat Gaussian shape (see Figure 25) and the clear bias towards large enantiomeric excesses is no longer present. The total enantiomeric excess is nearly zero, which is in agreement with controls previously acquired. Due to the statistical nature of the experiment many crystallizations were needed in order to draw meaningful conclusions. If left-handed electrons initiate the crystallization of predominantly dextrorotatory sodium chlorate crystals, one would expect positrons to yield predominantly levorotatory



Table V. Sodium chlorate controls (at RADCAL)

Dish	Clockwise	Counter Clockwise	Enantiomeric Excess
1	16	0	100
2	39	36	4.0
3	0	20	-100
4	11	16	-18.5
5	26	11	40.5
6	12	14	-7.7
7	6	4	20.0
8	13	21	-23.5
9	8	16	-33.3
10	13	12	4.0
11	7	8	-6.7
12	10	3	53.8
13	3	6	-33.3
14	10	6	25.0
15	10	7	17.6
16	13	14	-3.7
17	9	12	-14.3
18	11	11	0
19	6	10	-25
Total	223	227	-89

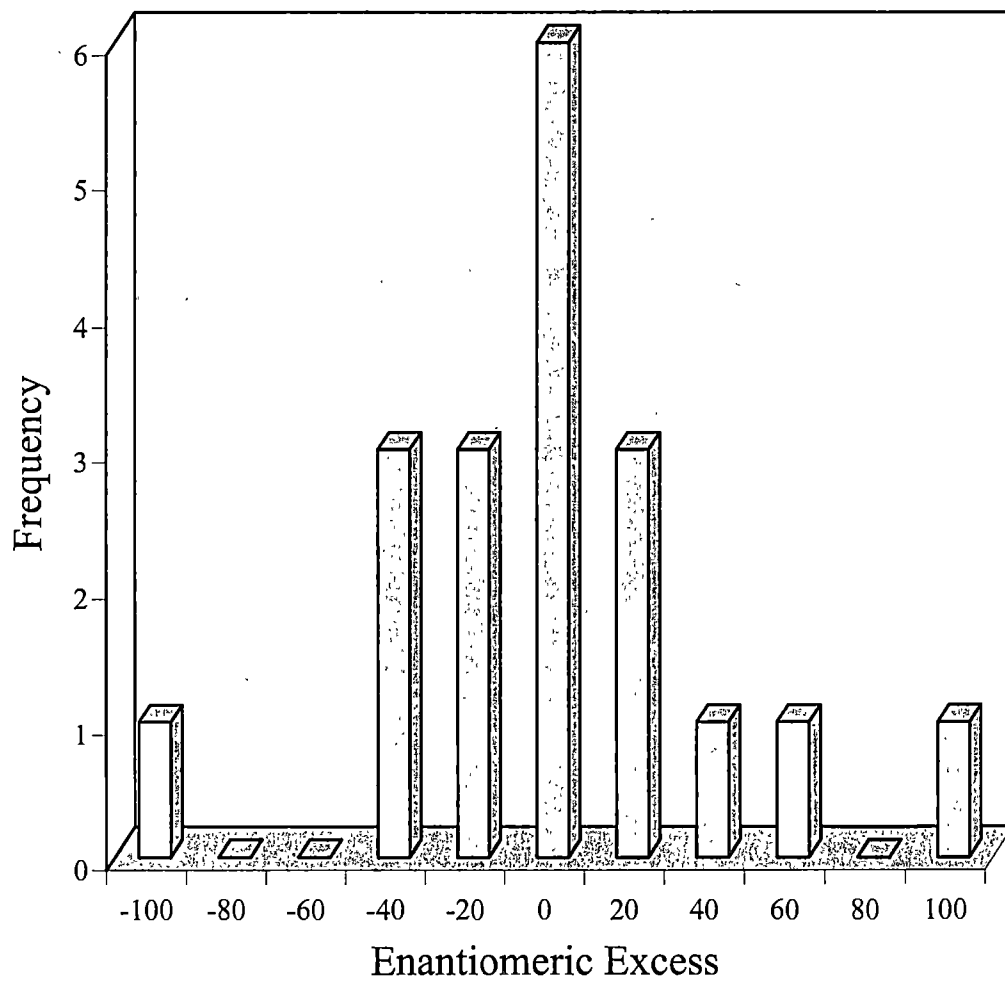


Figure 25. Sodium chlorate control experiments performed at the same site as the beta radiolysis experiments.

crystals since positrons produced from radioactive decay are mainly right-handed. Due to limited access to the positron source, a small number of chlorate crystallizations were performed. The seven crystallizations (see Table VI) yielded an excess of  $-55.7\%$  which is in the opposite direction to that produced by the beta particles. However, the small number of trials prohibits definitive conclusions despite the fact that the results are consistent with expectations. The bar graph of the data (Figure 26) shows the same skew as was seen in the beta radiation experiments, i.e., most of the dishes yielded enantiomeric excesses of either  $+100$  or  $-100$  indicative of an enhanced stirring mechanism.

Beta radiolysis of water has been studied extensively for sixty years and is quite complex.<sup>51</sup> The range of electrons and positrons in matter can be quite ill defined. Large statistical fluctuations in their path length are due to large fluctuations in their energy loss. This is due to greater energy losses per collision allowed for electrons as well to the emission of bremsstrahlung radiation which occurs when a charged particle undergoes acceleration or deceleration. This process is important for electrons and positrons since these particles undergo significant decelerations when interacting with matter. The radiation that is emitted from the slowing down of spin polarized electrons and positrons will be circularly polarized.<sup>52</sup> This circularly polarized radiation can further influence primary nucleation as it progresses into the solution. Since water has significant stopping power for electrons, any effect that the beta and positron particles have on primary nucleation will occur at or near the surface. In addition to bremsstrahlung, when an electron encounters the surface a variety of ionization and dissociative phenomena occur.

Table VI. Sodium chlorate crystallizations under Na<sup>22</sup> source.

Dish	Clockwise	Counter Clockwise	Enantiomeric Excess
1	0	24	-100
2	0	15	-100
3	0	18	-100
4	0	10	-100
5	11	0	100
6	4	5	-11.1
7	13	25	-31.6
Total	28	97	-55.2

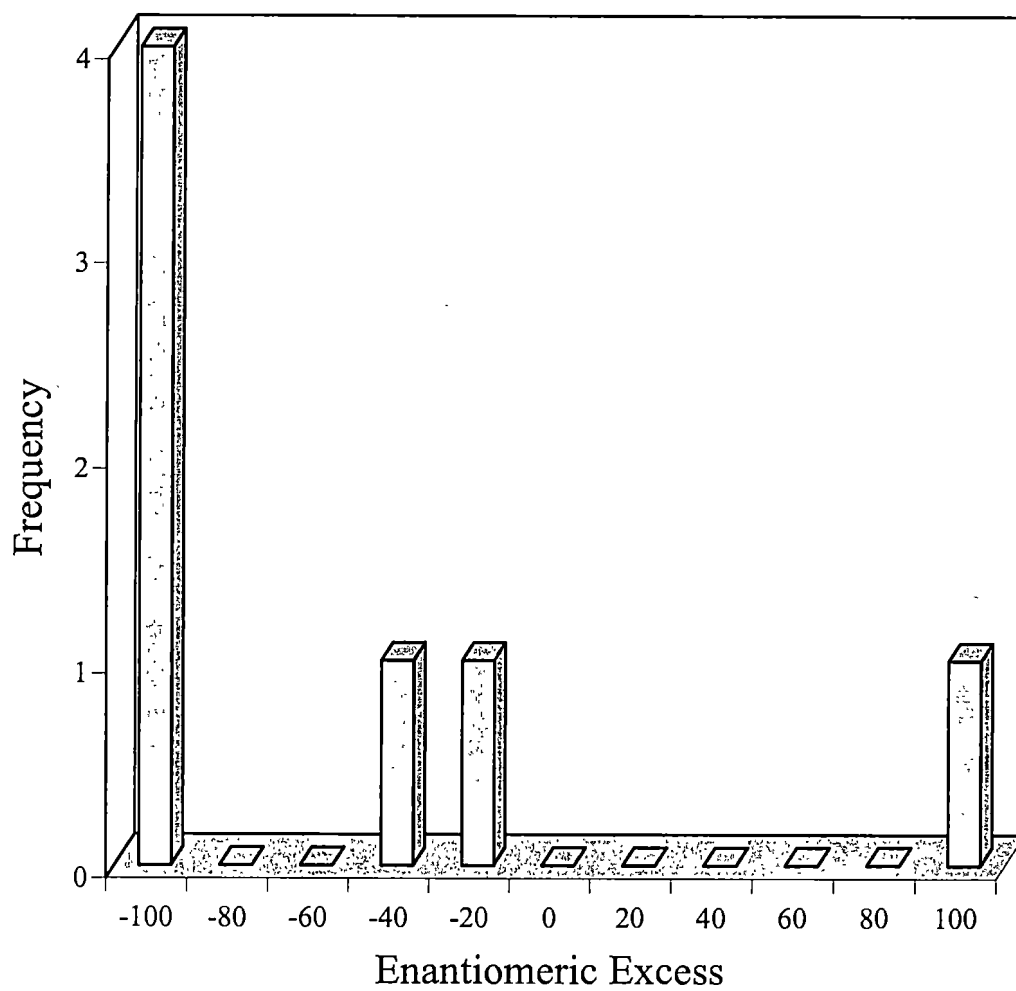


Figure 26. Histogram of the crystallizations of  $\text{NaClO}_3$  under the influence of  $\text{Na}^{22}$  positron source.

Ionization will produce tracks of secondary polarized electrons and  $\text{H}_2\text{O}^+$  and  $\text{HO}^+$ , all of which undergo subsequent chemistry.

While the electrons and positrons are slowing down and emitting bremsstrahlung and radiation chemistry is occurring, primary nucleation can occur independently, thus yielding levo- and dextro-rotatory crystals. However, the experimental results can be explained by assuming that the circularly polarized bremsstrahlung influences primary nucleation a significant number of times. Electrons and positrons (and their accompanying radiation) would be expected to influence primary nucleation in opposite ways for identical experimental conditions, and the data show this. The influence of the circularly polarized radiation emitted by the decelerating beta particles may occur through a number of mechanisms: by providing a chiral solvent cage around the quasi-amorphous state attained during primary nucleation, photointerconversion of a primary nucleation site with one absolute configuration into its mirror image, or preferential decomposition of one enantiomer over the other.

### Conclusion

The effect of spin polarized electrons and positrons emitted during radioactive decay on the crystallizations of sodium chlorate have been studied. Left-handed electrons induced an excess of dextrorotatory sodium chlorate crystals while right-handed positrons produced an excess of levorotatory sodium chlorate crystals. A feasible symmetry breaking mechanism is that the circularly polarized bremsstrahlung emitted during the deceleration of the charged particles influenced the primary nucleation sites while heating of the solution induced convection which propagated the primary nucleation sites. The crystallizations of sodium bromate showed an overwhelming bias towards the formation

of dextrorotatory crystals. At this point, the source of the bias is unclear, though contamination is suspected.

## CHAPTER IV

## EXPERIMENTAL APPARATUS

Introduction

Linear time-of-flight mass spectroscopy (TOFMS) has become widely used as an analytical tool due to the relative ease of construction and speed with which spectra can be obtained. With the development of the laser, investigation of multiphoton processes such as multiphoton absorption and ionization in atoms and molecules expanded rapidly. A combination of multiphoton ionization and time-of-flight mass spectroscopy provides a convenient way to probe various ionization and dissociation pathways in molecules as well as accurately determine ionization potentials. If some multiple of the photon energy is in resonance with an allowed transition of the molecule, a considerable enhancement of the ionization signal is achieved. This enhancement is known as resonantly enhanced multiphoton ionization (REMPI). If the wavelength of the laser is tuned while ions are being detected, the energies of the allowed transitions are effectively mapped out. Thus, REMPI-TOFMS has become a versatile tool in many spectroscopic studies.

One goal of this thesis was to investigate the effect of laser polarization on the rate of ionization for a chiral organic molecule. In particular, the difference in the rate of ionization for right and left circularly polarized light, which constitutes a circular dichroism in the multiphoton ionization, was to be studied. The ability to ionize the molecule and accurately identify the products, such as fragments and clusters, of the multiphoton process was crucial. The design and construction of a linear time-of-flight mass spectrometer with a laser as the ionization method was the optimal way to meet the requirements of this particular study.



## Laser System

The source of multiphoton ionization for the time-of-flight mass spectrometer was provided by a Continuum Optical Parametric Oscillator (OPO) Mirage laser system which was pumped by an injection-seeded Nd:YAG (Neodymium doped yttrium-aluminum-garnet) laser. The Mirage OPO utilizes the optical parametric process which is a three photon process whereby the pump photon interacts with a nonlinear medium and splits into two less energetic photons, known as the signal and idler. The three photons (the pump, the signal, and the idler) must satisfy both energy and momentum conservation. Energy conservation is satisfied when the pump frequency is equal to the sum of the frequencies of the signal and the idler. Momentum conservation is much more difficult to satisfy since the two output photons have different frequencies and velocity is frequency dependent. However, it must be noted that to conserve total momentum, the angular momentum of the photons must also be taken into account in addition to the linear momentum. If a nonlinear birefringent crystal such as potassium titanyl phosphate, or KTP, is used, there is a particular angle in which refractive indices of the crystal allow conservation of momentum, linear and angular, to be satisfied. By simply adjusting the angle of the crystal (and the optics in the oscillator cavity) with respect to the polarization of the pump laser, a wide range of output frequencies are attainable. Through the use of the frequency tripled output from the Nd:YAG pump laser, the Mirage is capable of producing single longitudinal mode (SLM) laser light, with a bandwidth of approximately  $.02 \text{ cm}^{-1}$ , over a span of wavelengths that ranges from 425 nm to 2120 nm. The oscillator and amplifier crystals as well as the tuning mirror are mounted on motor driven stages which are connected to a personal computer complete

with the requisite software to control the motors. This particular design allowed for complete computer control of the lasing crystals in order to optimize the output power of the beam via phasematching, achieve single longitudinal mode (i.e., minimize the bandwidth), and tune the wavelength.

#### Time-Of-Flight Mass Spectrometer

The linear time-of-flight mass spectrometer, depicted in Figure 27, was constructed using standard stainless steel parts from a variety of sources. The interaction region was contained within a stainless steel Conflat six-way cross (Huntington Labs) with 8" outer diameter ports available for introducing the laser beam and the gas sample as well as attaching the pumping system. There were four additional ports with 2.75" Conflat flanges at 45° with respect to the 8" ports through which electrical feedthroughs could be mounted in order to supply voltages to the system. Connected to the main chamber was a linear chamber 4" in diameter with 6" O.D. Conflat flanges at each end and a 6" O.D. access port in the center to form an exaggerated tee.

The entire system was brought to a rough vacuum with two 158 L/min mechanical pumps (Fisher Scientific) capable of pressures of approximately  $10^{-2}$  Torr. The chamber pressure was further reduced using a Varian V500 turbomolecular pump mounted onto the six-way cross that housed the interaction region as well as a Varian V250 turbomolecular pump connected to the center access port on the linear chamber. The pressure in the system was monitored using an ionization gauge attached near the V250 turbo pump. The base pressure in the chamber was typically  $1 \times 10^{-8}$  Torr.

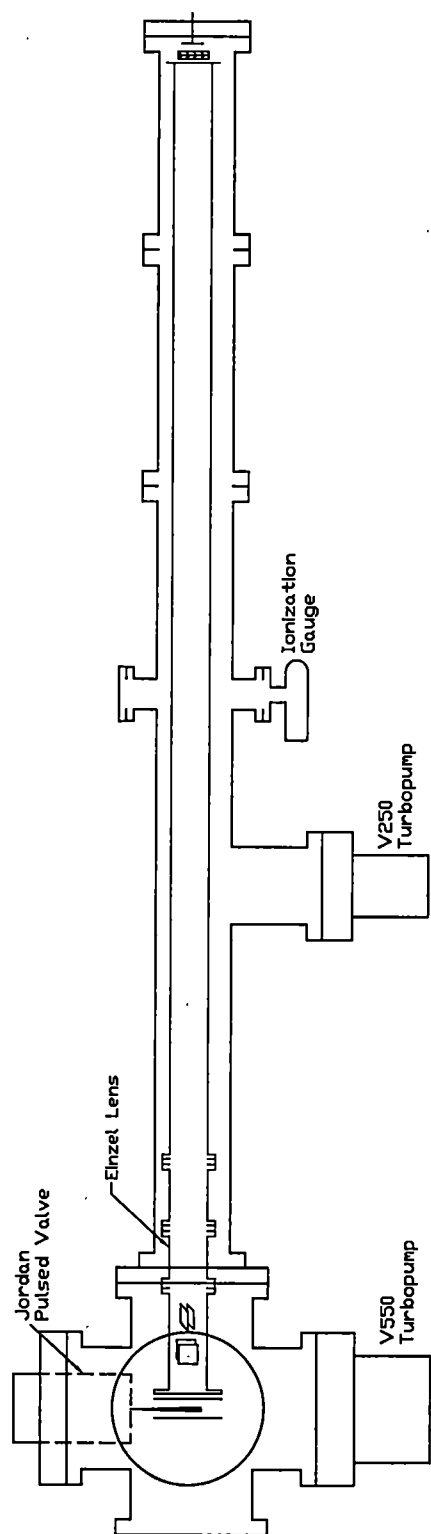


Figure 27. Diagram of the time-of-flight mass spectrometer .

The interaction region consisted of a stainless steel repeller plate with along with a similar plate (the extraction grid) with a 1" diameter hole in the center and grid material spot-welded over the hole. The repeller plate and extraction grid are separated by a distance of 2.5 cm. A third grid was separated from the extraction plate by a distance of .65 cm and was set to ground. In order to minimize Doppler broadening, it was necessary that the laser beam, the gas pulse, and the flight tube be arranged in such a manner as to be orthogonal to each other. The gas pulse was introduced into the spectrometer via an R. M. Jordan pulsed valve system mounted vertically on the six-way cross. The pulsed valve was located approximately 8 cm from the center of the interaction region and produced a 360  $\mu$ s gas pulse expanded in a free-jet expansion (no skimmer was used) through a .5 mm orifice. An advantage of having the pulsed valve directed towards the aforementioned V500 turbo pump was the substantial reduction in chamber pressure even with gas being pulsed into the interaction region. In order to obtain signal, the gas pulse from the Jordan pulsed valve had to be temporally and spatially synchronized with the laser pulse. The spatial overlap was attained simply by centering the laser through the entrance and exit ports. It was assumed that the pulsed valve was already centered on the flange. Temporal overlap of the two pulses was achieved by using a Stanford Research System delay generator (DG535) to trigger both the Nd:YAG laser which pumped the Mirage OPO and the Jordan pulsed valve. Since the time required for the gas pulse to reach the interaction region was considerably longer than the time for the laser pulse, the pulsed valve was triggered first. The time delay needed before triggering the laser was determined using a crude calculation of the time required for the gas pulse to reach the center of the interaction region, assuming a

nominal value of 200 m/s for the speed of the gas pulse. Coarse adjustments were made to the timing sequence based on the above calculation and taking into account the time between the firing of the flashlamps and the opening of the Q-switch (optimal delay time was 340  $\mu$ s). The time for the laser pulse to reach the interaction region was negligible (approximately 80ns). After obtaining signal, fine adjustments were made on the temporal overlap of the two pulses using the magnitude of the signal obtained as a guide. Essentially, maximum overlap of the two pulses corresponded to maximum signal obtained as the triggering of the pulsed valve was adjusted. Figure 28 shows a diagram of the timing sequence when the system was operating at maximum overlap between the laser and the gas pulse.

The drift region consisted of a 2" O.D. stainless steel flight tube that was 175 cm in length mounted within the linear chamber using aluminum holders with Teflon feet attached to maintain stable position of the flight tube in the center of the chamber. Since we were only studying positive ions, the flight tube was set to ground, although the option to apply any voltage necessary to the flight tube was available, thus allowing for the possibility of studying negative ions. Horizontal and vertical (i.e., XY) deflector plates were mounted near the entrance of the inner flight tube to compensate for the initial downward velocities of the ions created by the laser. In addition, an Einzel lens was placed just after the deflector plates to allow for focusing of the ions to improve resolution. The Einzel lens was constructed by dividing the initial portion of the inner flight tube into three separate elements using stainless steel mounts with Teflon spacers. The first and third elements were set to ground along with the remainder of the flight tube while the middle element, electrically isolated from the others, could be set to the voltage

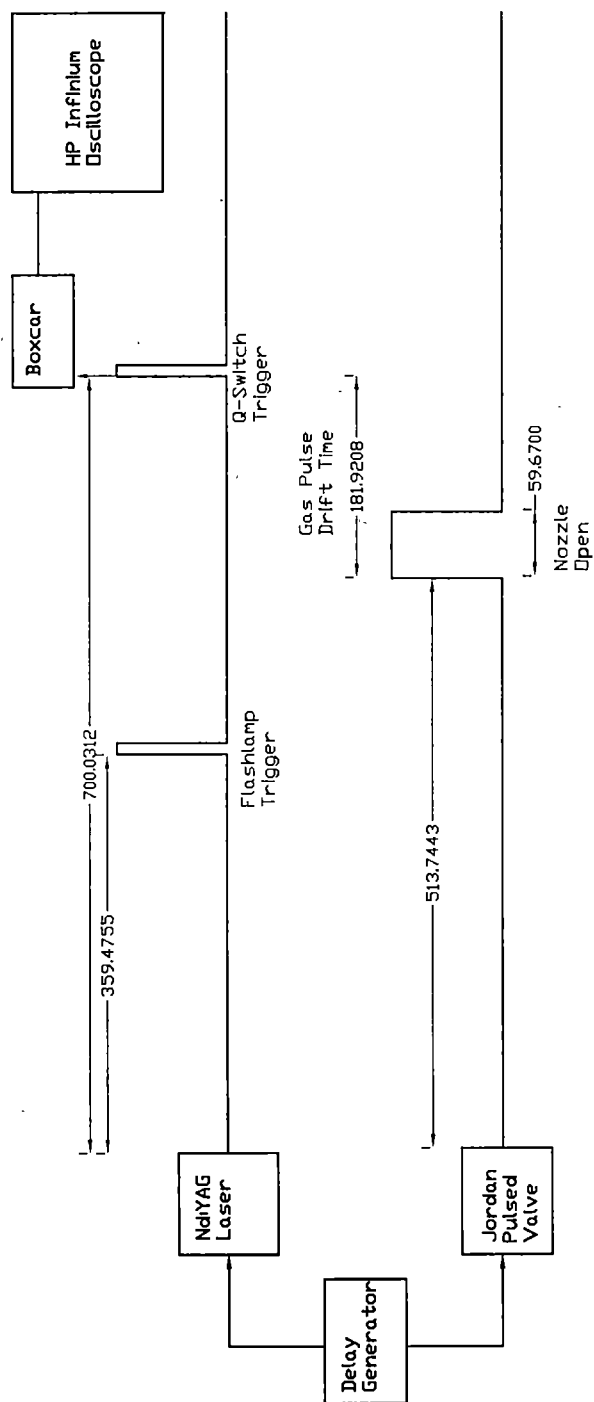


Figure 28. Diagram of the timing sequence for triggering the gas pulse and the laser system.

necessary to achieve maximum resolution. Under typical operating conditions, however, the Einzel lens was not used since the resolution of the spectrometer was sufficient for all studies performed.

The detector system, shown in Figure 29, was an R. M. Jordan detector assembly with two Galileo microchannel plates with a usable area of 18mm mounted in a Chevron configuration. Power to the detector system was provided by an R. M. Jordan time-of-flight power supply. This particular instrument also provided the voltages to the repeller plate, the extraction grid as well as to the deflector plates and Einzel lens. The entrance microchannel plate voltage, designated as VD1, was typically set at -2100 volts. The design of the power supply was such that a second voltage, VD2, was applied between the two channel plates at 54.5% that of the voltage of the first. A third voltage, VD3, was placed on the back of the second channel plate and was 9.1% of the first voltage. Thus, the voltage in the middle of the two channel plates would be  $VD2 = -1145$  volts while the exit voltage would be  $VD3 = -191$  volts, producing an applied voltage across the channel plates of approximately -1900 volts. Ions produced in the interaction region fly the length of the flight tube and are attracted to the entrance channel plate. When the ions collide with the channel plates, electrons are produced which fall through the potential difference across the channel plates. Amplification of the signal is accomplished through subsequent collisions which generate secondary electrons. Upon exiting the second channel plate, the amplified signal is collected by a grounded conical electron collector connected to a  $50\Omega$  feedthrough on the 6" Conflat flange. The signal was then processed through an EG&G Ortec model 9301 preamplifier which was connected close to the electrical feedthrough. Further amplification was achieved with an EG&G model 474

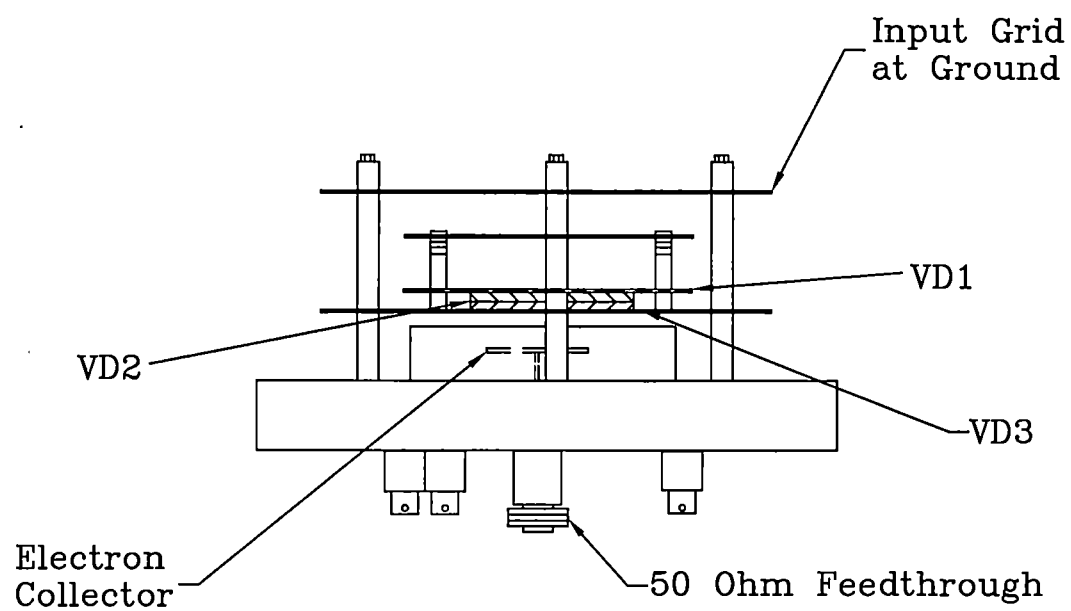


Figure 29. Diagram of the microchannel plate system used to detect ions in the mass spectrometer.



Timing Filter Amplifier. Complete time-of-flight spectra were viewed with a Hewlett-Packard Infinium digital oscilloscope, which was externally triggered using the Q-switch output from the laser. The oscilloscope possessed a variety of features which allowed the waveforms to be averaged and saved to disk for subsequent data manipulation. A complete view of the TOFMS system, including the electronics, is presented in Figure 30. Note that while the TOFMS has the versatility to acquire negative ion mass spectra, it was designed to operate primarily in the positive ion detection mode.

### Testing and Initial Measurements

Since the first multiphoton ionization spectrum of nitric oxide was obtained in 1975 by Johnson and coworkers,<sup>53</sup> extensive work has been performed on this molecule due to its low ionization potential, its well-characterized excited states, and the rich variety of features observed in the spectrum. Thus, it was initially decided to test the operation of the TOFMS using nitric oxide. The energy levels of nitric oxide, shown in Figure 31, have been well documented<sup>54, 55</sup> by numerous groups. Resonantly enhanced multiphoton ionization (REMPI) from the  $X^2\Pi$  ground state through the  $A^2\Sigma^+$  excited state using two photons to reach the transition with two more photons being required to ionize was chosen due to large ionization signals obtained by other investigators. In the terminology of multiphoton ionization this type of transition is known as a (2+2) REMPI transition. An advantage in using NO was provided by the large number of vibrational and rotational states contained within the excited electronic state. Consequently, the number of degrees of freedom was reduced because nearly any wavelength that fell within the range of the  $A^2\Sigma^+$  state (which covered the 450 nm to 455 nm wavelength range) in two photons would produce ions, essentially eliminating the wavelength dependence and simplifying

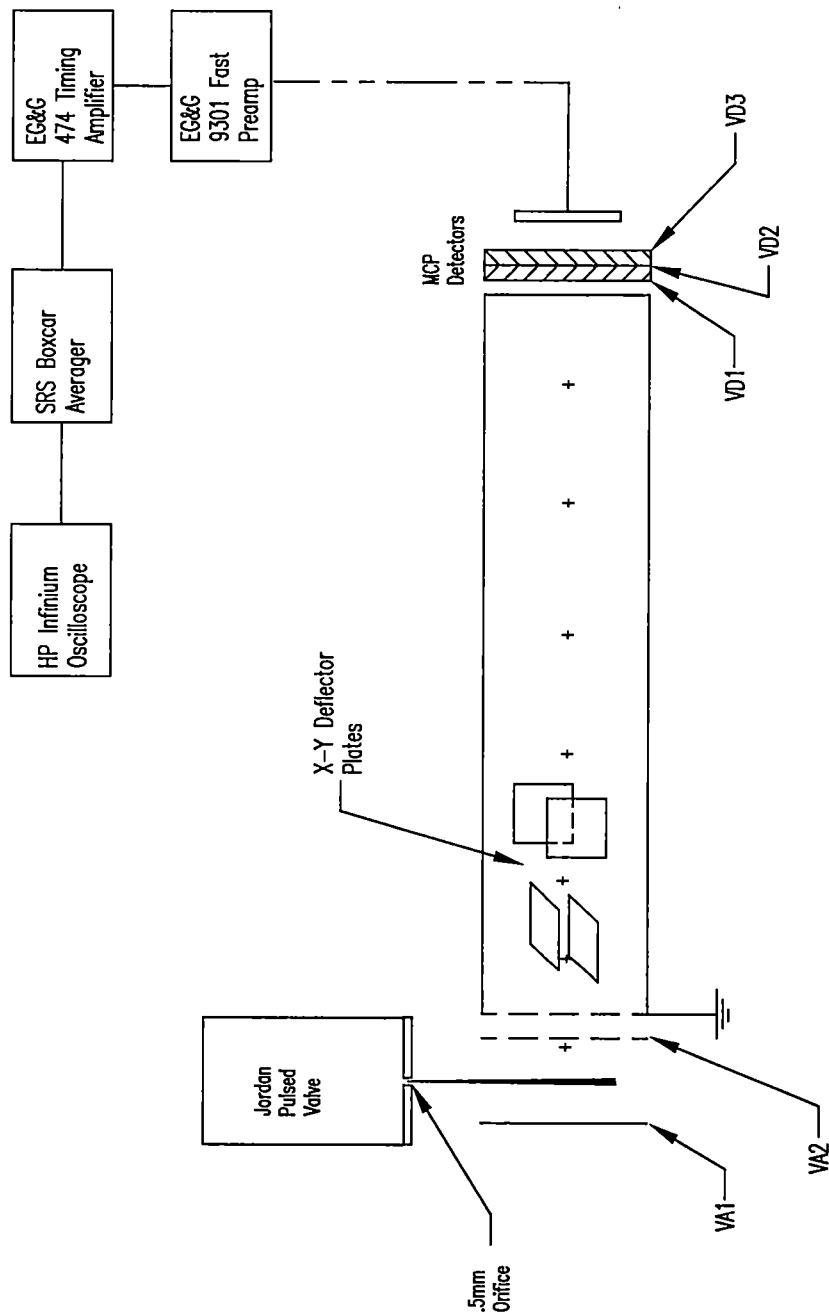


Figure 30. Diagram of the mass spectrometer along with the electronics used to acquire data.

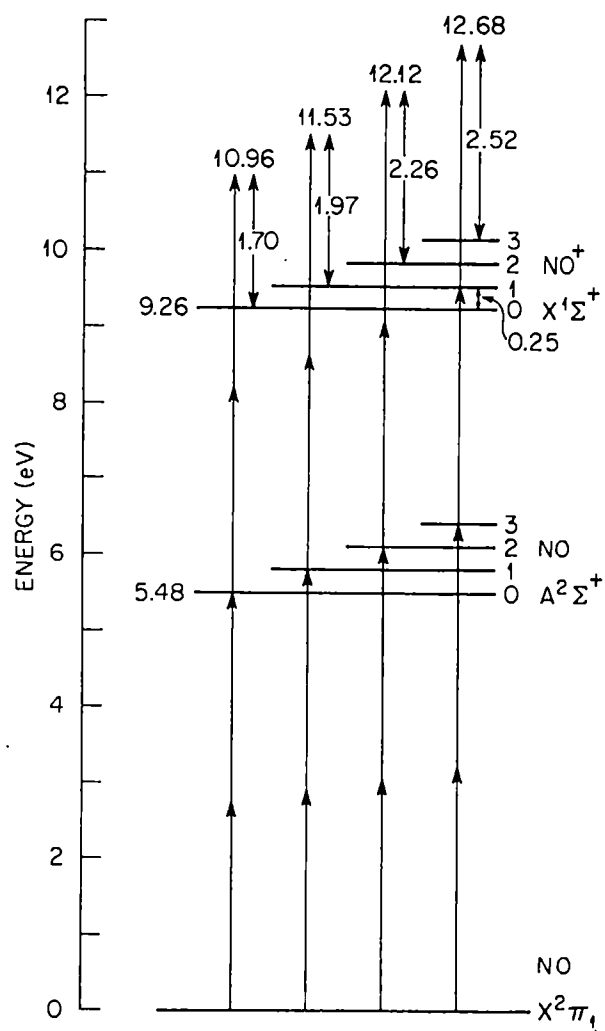


Figure 31. Energy level diagram for nitric oxide (NO).

the task of obtaining signal. The laser was aligned through the interaction region and focused with a 7.5 cm focal length lens mounted internally using a stainless steel lens mount at the entrance of the TOFMS to give a power density of  $1 \times 10^{11}$  W/cm<sup>2</sup>. After adjusting the various voltages to the extractor and repeller plates as well as the voltages to the XY deflector plates, a mass spectrum of nitric oxide was obtained. Since <sup>14</sup>N and <sup>16</sup>O are the primary isotopes of nitrogen and oxygen, the mass spectrum consisted of a single NO peak.

The temperature of the nitric oxide can be found by using the equation for the adiabatic free expansion of a gas at constant entropy given by Haberland et al.<sup>56</sup>

$$c_p T_0 = c_p T + \frac{1}{2} m v^2 \quad (4.1)$$

where  $c_p$  is the specific heat at constant pressure,  $T_0$  is the gas reservoir temperature,  $T$  is the temperature after the expansion,  $m$  is the mass of the sample, and  $v$  is the velocity.

Using thermodynamic relations for an adiabatic expansion, Haberland has shown that the temperature of the gas is given by the expression:

$$T = \frac{T_0}{\left[1 + \frac{1}{2}(\gamma - 1)M^2\right]} \quad (4.2)$$

where  $M$  is the local Mach number of the expanded gas and  $\gamma$  is the specific heat ratio (i.e.,  $\gamma = c_p/c_v$ ). The local Mach number is the ratio of the stream velocity,  $v$ , to the local speed of sound and can be approximated by:<sup>57</sup>

$$M \approx \left(\frac{\gamma + 1}{\gamma - 1}\right)^{\frac{\gamma + 1}{4}} \left(\frac{z}{D}\right)^{\gamma - 1} \quad (4.3)$$

where  $z$  is the distance from the orifice, and  $D$  is the orifice diameter. An estimate of the temperature can be obtained if nitric oxide is assumed to follow the general prediction that  $\gamma$  is approximately 1.40 for a diatomic gas. The distance from the orifice to the interaction region is  $\sim 5.5$  cm, while the orifice diameter is .5 mm. Applying these values to equation (4.3) yields a value of  $\sim 40$  K for the temperature of NO in the interaction region. The velocity of the NO beam was determined to be 295 m/s by noting that the time required for the gas pulse to reach the center of the interaction region was 186  $\mu$ s.

In order to ensure that the system was operating properly, a scan of the NO signal as a function of wavelength was taken. This was accomplished by routing the MCP output signal through a Stanford Research Systems Gated Integrator and Boxcar Averager, a.k.a., boxcar, an SR245 computer interface module, and into a CTX laptop computer where the data was collected using a BASIC program written in house (see Appendix I). A typical scan taken over the range of the  $A^2\Sigma^+$  state is shown in Figure 32. Many of these peaks have been previously assigned, so a detailed analysis will not be attempted here. It is sufficient to note that there is a very good agreement between the spectrum obtained here and that presented by other investigators.<sup>58</sup>

In order to maximize the resolution of the spectrometer, i.e., satisfy the Wiley-McLaren<sup>59</sup> condition, it was necessary to look at the mass spectrum of a sample with several closely spaced peaks. Xenon was chosen because it has a well studied (3+2) REMPI peak through the  $6s[\frac{3}{2}]_1^0$  at 440.8 nm (see Figure 33). Thus, the xenon could act as a wavelength calibration for the laser. In addition, xenon has seven isotopes in the mass range from 128 amu to 136 amu which were used to maximize and determine the mass resolution of the TOFMS. The mass resolution primarily depends on the time of flight of

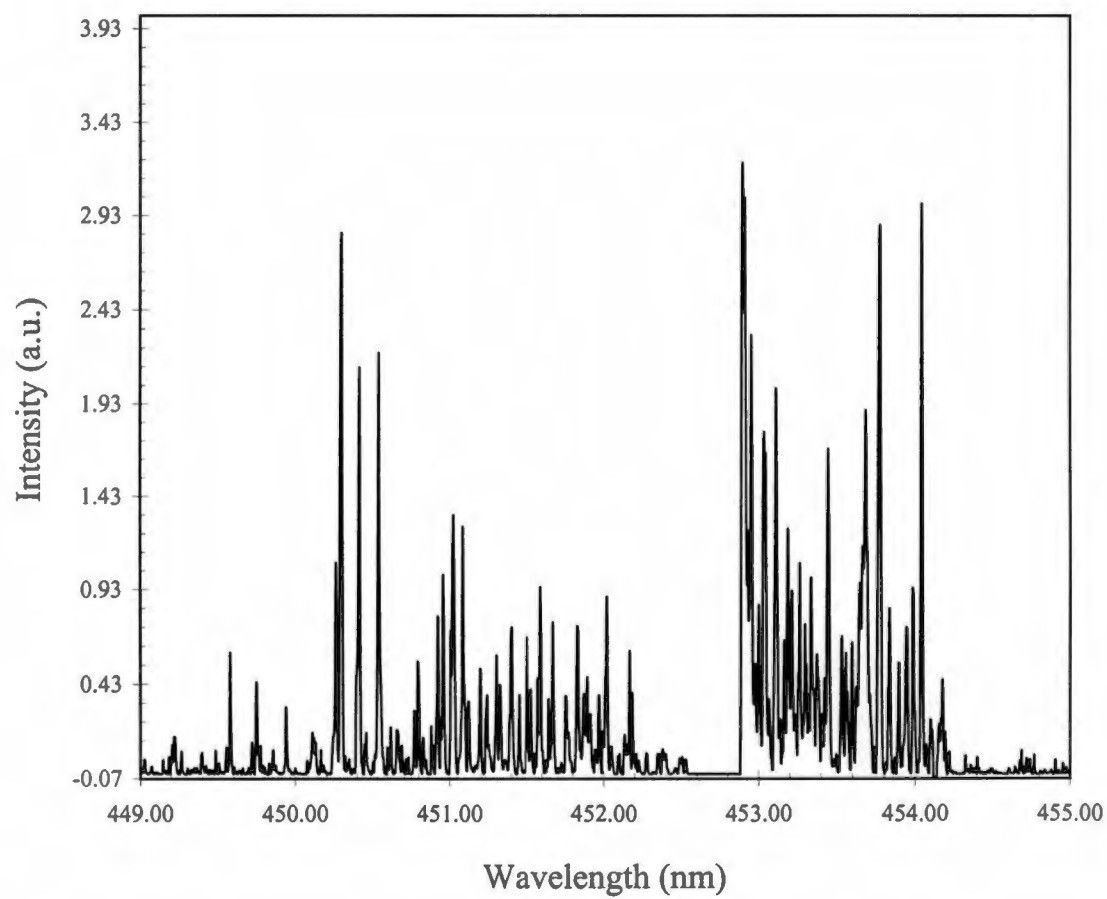


Figure 32. (2+2) REMPI of nitric oxide through the  $A^2\Sigma^+$  state.

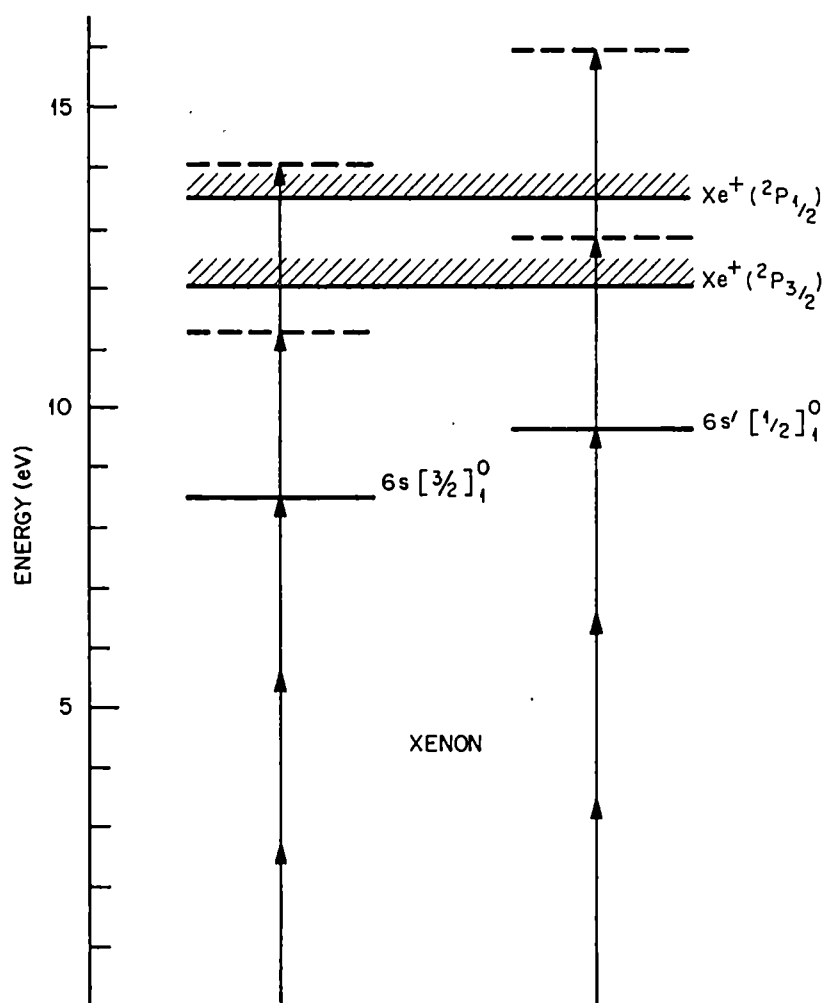


Figure 33. Energy level diagram for (3+2) REMPI through the 6s state of xenon.

the particles as well as the initial kinetic energy. In a field-free region, the standard equation for the kinetic energy of a particle can be rearranged to yield an equation for the flight time in terms of the flight distance,  $L$  (neglecting the distance traveled by the ions in the accelerating region), the mass, and the kinetic energy,  $E$ :

$$t = \left( \frac{L}{\sqrt{2E}} \right) \sqrt{m} \quad (4.4)$$

Differentiating equation (4.4) while assuming that the ions gain the same amount of kinetic energy (which is constant) yields:

$$dt = \left( \frac{L}{\sqrt{2E}} \right) \frac{dm}{2\sqrt{m}} \quad (4.5)$$

Dividing both sides by  $t$  yields:

$$\frac{dt}{t} = \frac{dm}{2m} \quad (4.6)$$

This equation relates the mass resolution, which is the standard figure of merit for a mass spectrometer, to the time resolution, which is the experimental quantity that is actually measured.

A typical mass spectrum for xenon is shown in Figure 34. The fifth  $\text{Xe}^+$  mass peak in the spectrum has a flight time of 33.51  $\mu\text{s}$  with a full-width at half max (FWHM) of .037  $\mu\text{s}$ , which gives a  $\Delta t/t$  of .0022083. By applying equation (4.6), the resolution of the TOFMS was determined to be  $\sim 450$ .

Since a primary objective of this thesis was to study polarization effects in multiphoton ionization, i.e., rates of ionization for linearly polarized light versus circularly polarized light as well as right to left circularly polarized light, accurate establishment of the



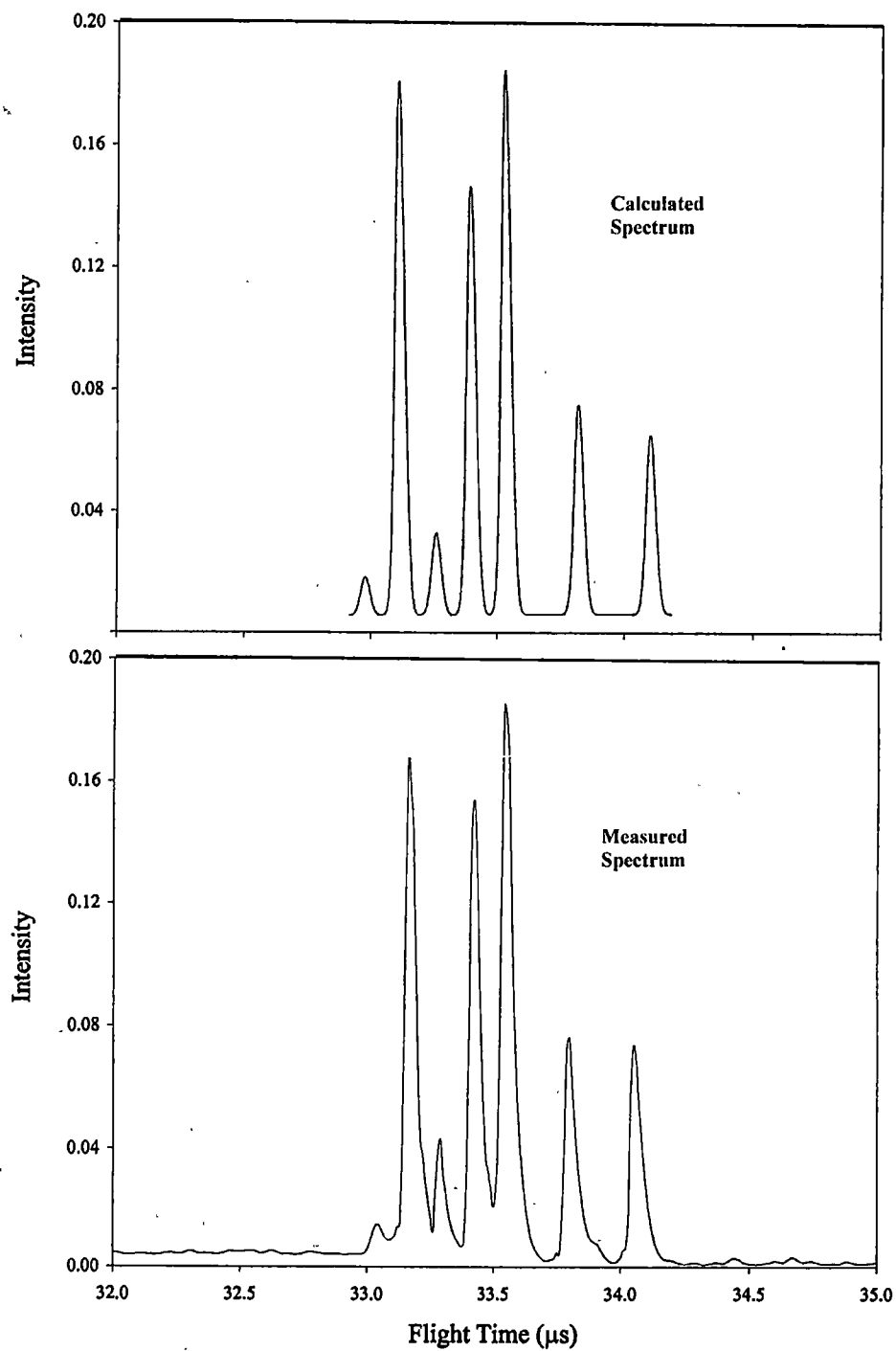


Figure 34. Mass spectrum of xenon. The bottom curve shows data taken with the TOF described in this thesis while the top curve shows a mass spectrum calculated using IsoPro.

polarization of the laser beam as it interacted with the sample was essential. In other words, if the ratio of ionization for linear to circular was obtained, it was absolutely necessary that the molecule did in fact interact with linearly and circularly polarized light. To that end, the xenon was used as a test to ensure that the proper polarizations were being used. The electric dipole selection rules for xenon are  $\Delta J = 0, \pm 1$ , and  $\Delta M = \pm 1$  for each photon transition. The ground state of xenon is a  $5p^6, j = 0$  state while the  $5p^5 6s^1$  state consists of  $j = 1$  and  $j = 2$ . In three photons from the ground state to the  $6s$  state using circularly polarized light (where right circularly polarized light corresponds to  $\Delta M = 1$  while left circularly polarized light corresponds to  $\Delta M = -1$ ), the transition is forbidden. If linearly polarized light (LPL) is used, however, the transition is allowed because linearly polarized is composed of right and left circularly polarized light, and can have a  $\Delta M$  of either  $+1$  or  $-1$ . Thus, a possible scenario using LPL could be

$$j=0 \rightarrow j=1 \rightarrow j=0, 2 \rightarrow j=1, 3$$

Clearly, it is impossible to go from the  $j = 0$  ground state to the  $j = 1$  excited state in three photons using  $+1$  (or  $-1$ ) for each single-photon transition. This forbidden three-photon transition with circularly polarized light provides an ideal method for testing the polarization of the laser beam. It is simply necessary to tune the laser to the  $[3+2] 6s[\frac{3}{2}]_1^0$  REMPI peak in xenon and adjust the beam to circular polarization while observing the ionization signal. Elimination of the xenon signal ensures that the beam does possess the requisite circular polarization.

Left and right circularly polarized light were obtained with linearly polarized light incident at  $+45^\circ$  and  $-45^\circ$  respectively on a single Fresnel rhomb. A continuous range of

polarizations from circular (left or right) through elliptical to linear can be obtained by adjusting the angle which the polarization vector makes with the vertical axis of the single Fresnel rhomb. In order to select between linear and left and right circular polarizations, a double Fresnel rhomb (which simply rotates the plane of polarization of linearly polarized light) was used to control the angle at which the beam was incident on the single Fresnel rhomb. The setup employed to achieve the various polarizations is shown in Figure 35. Initial measurements using the TOFMS showed that the signal did not disappear when going from LPL to CPL. It was soon determined that the sapphire input windows on the TOFMS were depolarizing the laser beam. After changing the input windows to  $\text{LiF}_2$ , the ratio of the ionization for linearly to circularly polarized light was found to be approximately 20 (see Figure 36). Since this ratio ideally should be infinite (i.e., the transition is forbidden for circularly polarized), it was necessary to determine the cause of the small signal obtained with circularly polarized light. The most obvious explanation was simply a slight depolarization of the laser beam due to the lens and window. However, in order to eliminate any effects due to the electric field in the interaction region (which might cause some field mixing of states, thus making the transition slightly allowed), the ionization signal was accumulated for various values of voltage. Initially, 1885 V and 2285 V were applied to the repeller and extraction plates, respectively, which produced a uniform electric field of 120 V/cm. The voltage to the repeller plate was increased to 3285 V, which yielded a field of 520 V/cm. The ionization signal remained constant as the electric field was increased, indicating that there was no field mixing due to the voltages on the plates. Thus, it was taken for granted that the small signal obtained with circularly polarized light was in fact due to a slight

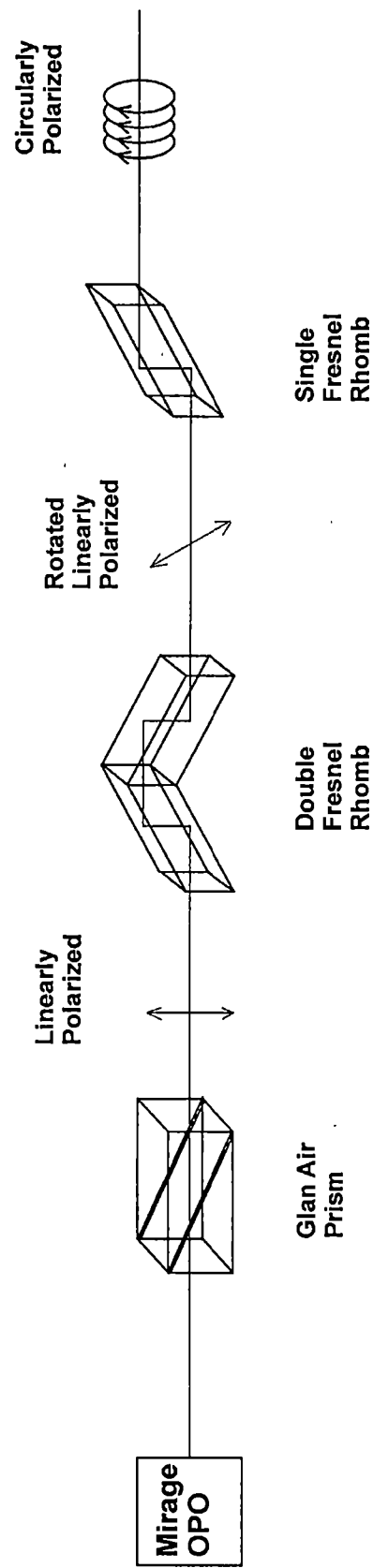


Figure 35. Diagram of the setup used to select various polarizations of the laser beam.

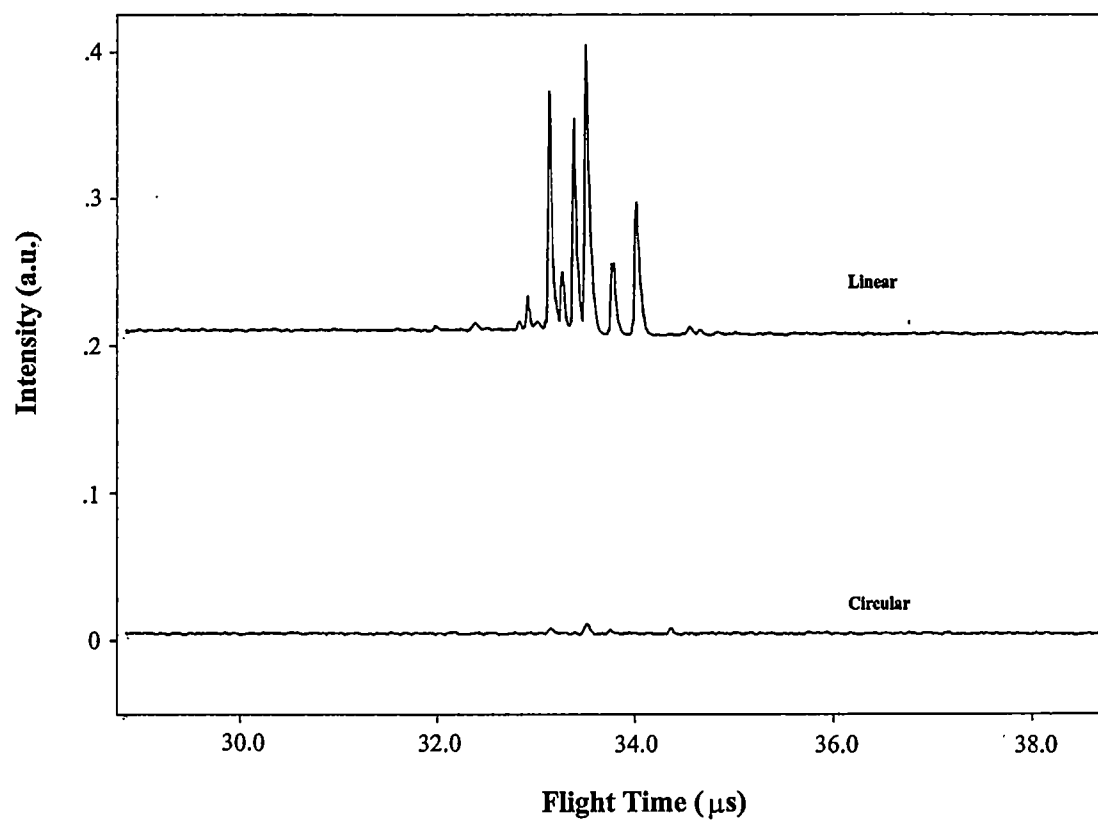


Figure 36. Polarization effects on the (3+2) REMPI of xenon. Note the absence of signal with circularly polarized light.

amount of beam depolarization. The ratio of circular to linear, which was calculated to be .05, provides a measure of the polarization of the incident beam. With the present experimental arrangement, it was possible to achieve circularly polarized light to within 95% purity. A complete picture of the TOF system along with the optical as well as the electronic arrangements is shown in Figure 37.

Further confidence that the system was operating properly was brought about by the measurement of the ratio of CPL versus LPL for the (3+2) REMPI of NO through the  $A^2\Sigma^+$  state. Some theoretical study has been done on multiphoton ionization using linearly and circularly polarized light. Unfortunately, much of the theoretical progress has occurred in the area of low order multiphoton processes, i.e., where the total number of photons required for ionization is less than three and at low laser power. Lowest order perturbation theory has been employed to address the problem of low order multiphoton ionization processes in atoms using linearly and circularly polarized light. A general expression was obtained by Klarsfeld and Maquet<sup>60</sup> for N-photon ionization:

$$\frac{\sigma_c}{\sigma_L} \leq \frac{(2N-1)!!}{N!} \quad (4.7)$$

It should be pointed out that in this equation the ionization signal is predicted to be larger with circularly polarized light than with linearly polarized light. This reflects the fact that for low order transitions into the continuum for linearly polarized light multiple pathways (i.e.,  $\Delta l = \pm 1$ ) can interfere with each other, thus reducing the ionization signal. This effect is virtually eliminated for higher order (larger N), which would explain the fact that for the N=5 process studied here, the ionization signal is smaller for circularly polarized light.

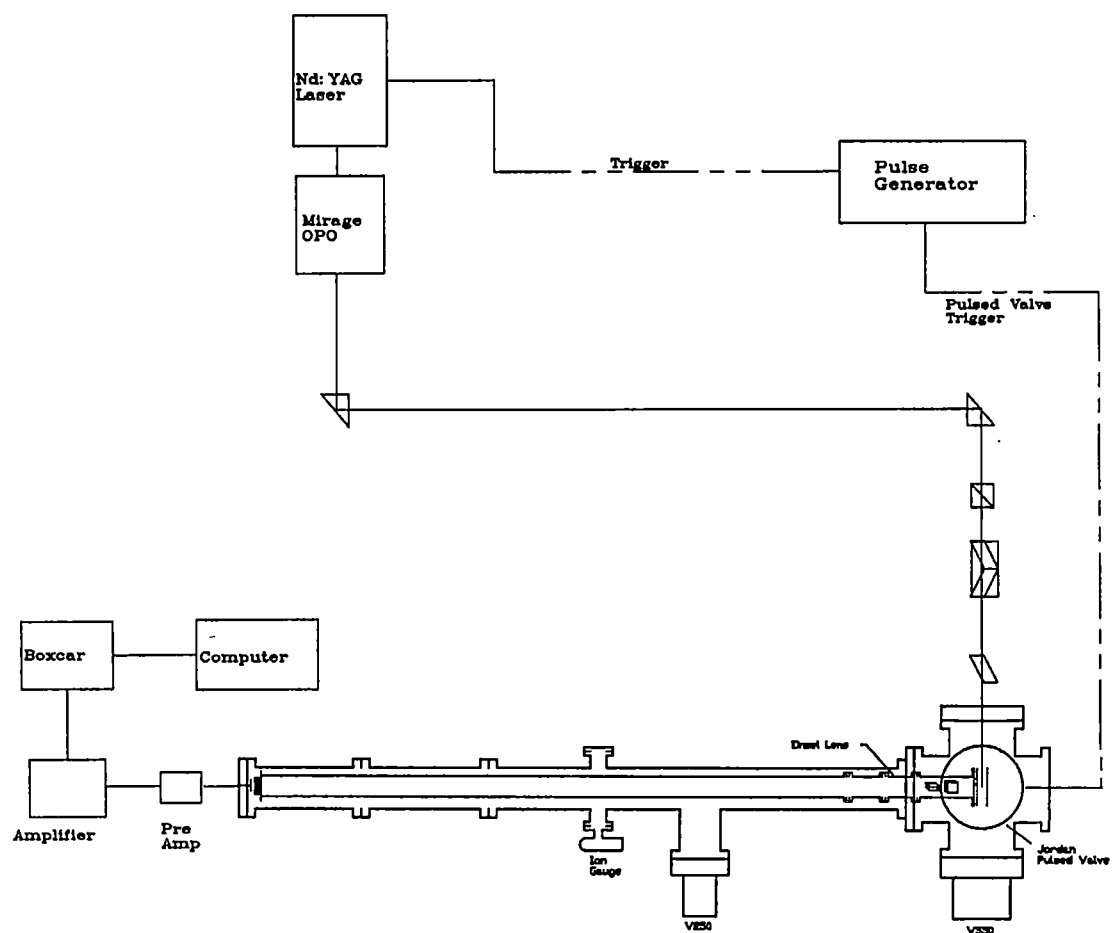


Figure 37. Diagram of the complete setup used to obtain mass spectra as a function of laser polarization.

It has been shown<sup>61</sup> that an upper bound for  $\sigma_C/\sigma_L$  (ratio of circular to linear) can be approximated by:

$$\frac{\sigma_C}{\sigma_L} = \frac{|R_c|^2 A_c^2}{|R_L|^2 A_L^2} \quad (4.8)$$

where R represents integrals over initial and final state radial wavefunctions

$$R = \int_0^\infty \rho^{N+2} R_f^*(\rho) R_i(\rho) d\rho \quad (4.9)$$

where  $\rho = x/a_0$  and A represents integrals over Clebsh-Gordon coefficients. Equation (4.8) can be simplified for large N (where N is the total number of photons required to ionize) and written as:

$$\frac{\sigma_C}{\sigma_L} \cong \frac{(N+1)(N+1)!}{(2N+1)!!} \frac{16}{e^2 (2N^3)^{1/2}} \left(\frac{2e}{N}\right)^{2N} \quad (4.10)$$

where e is Euler's number. For (3+2) REMPI where N=5, equation (4.10) yields a value of  $\sigma_C/\sigma_L=.131$ . Carman and Compton<sup>62</sup> previously measured the circular to linear ratio for the (3+2) REMPI via the  $A^2\Sigma^+$  ( $v=1$ ) state and found it to be  $0.11 \pm 0.05$ .

In order to measure the linear to circular ratio for this particular transition, it was necessary to locate the position of a resonance. Figure 38 gives a wavelength scan of NO in the 642 nm to 647 nm region with 6 mJ/pulse of laser power. The peaks are quite broad and somewhat noisy. The low signal-to-noise ratio is most likely due to the fact that this transition is very weak. It is a total five photon ionization which is not generally strong since it requires the simultaneous absorption of a large number of photons. Thus, a large power density is necessary to see the ionization signal. The circular to linear ratio was determined to be .248 at 644.75 nm, thus indicating that the transition with circularly polarized light is much less allowed. The experimental value obtained in this thesis is in



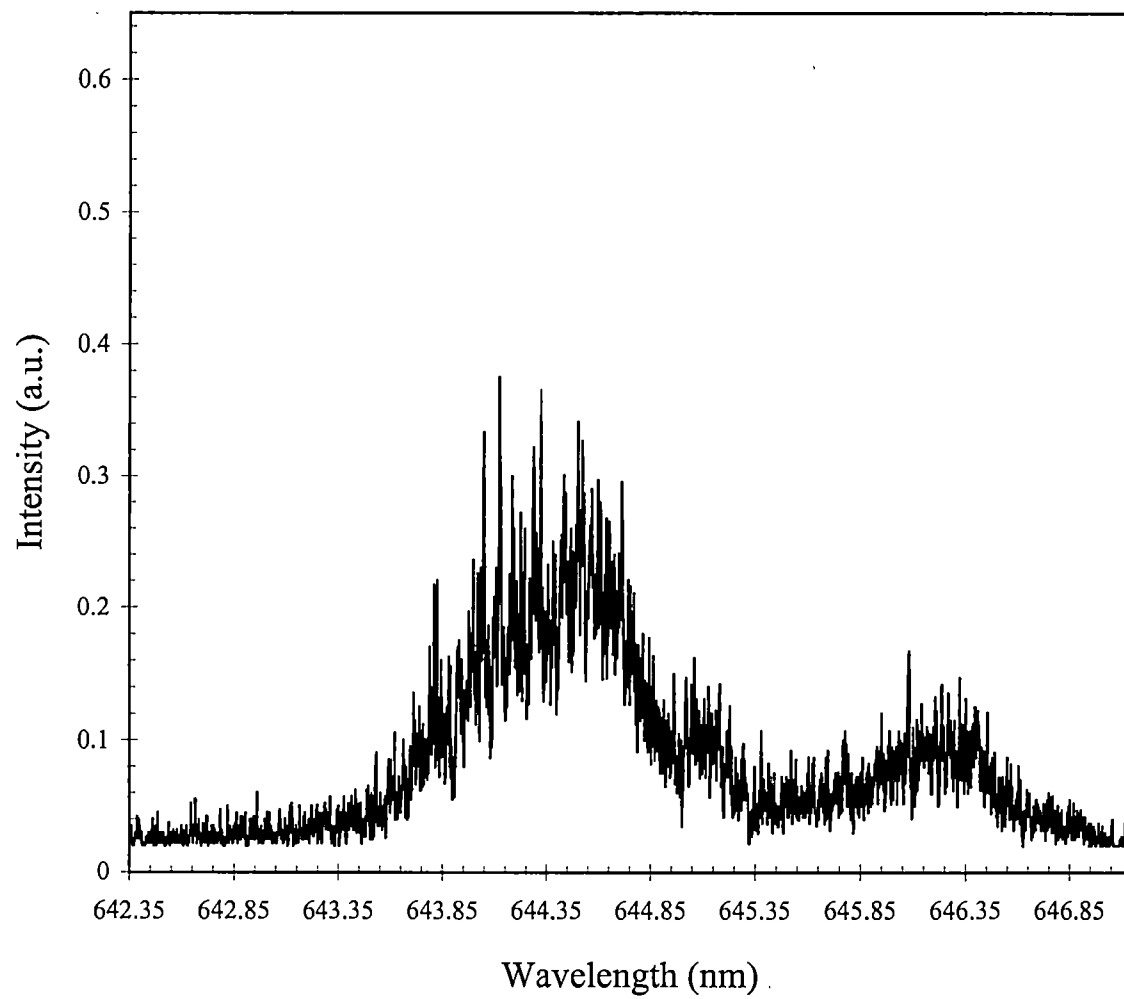


Figure 38. Wavelength dependence of the (3+2) REMPI of nitric oxide.

reasonable agreement with that determined by Carman and Compton and with the theoretical value.

### Conclusion

All data obtained for the xenon and nitric oxide indicated that the TOFMS system was operating properly. The results for the xenon showed that the appropriate laser polarizations were interacting with the sample, the signal-to-noise ratios were acceptable, and the resolution of the TOFMS was sufficient for the study of chiral organic molecules. The next step then was to choose a chiral molecule to look for a circular dichroism in the multiphoton ionization.

## CHAPTER V

## MULTIPHOTON IONIZATION OF 2-BUTYLAMINE

Introduction

One of the objectives of this thesis was the study of laser polarization effects in the multiphoton ionization of chiral molecules, i.e, the ratio of the ionization rate for circularly polarized light to the ionization rate for linearly polarized light as well the ratio of the ionization rates of right to left circularly polarized light, or circular dichroism. A few experiments have been reported on the study of polarization effects in ionization. A large circular dichroism of approximately 10% was recently measured in the one photon ionization of tyrosine nanocrystals.<sup>63</sup> However, this circular dichroism was enhanced because tyrosine crystallizes in a chiral space group. So there was a “double” chirality present: first in the molecule itself, then in the crystal. In addition, Cuellar et al. measured a circular dichroism in the angular distribution of photoelectrons from the  $7p_{3/2}$  state of cesium which had been aligned by the absorption of linearly polarized light.<sup>64</sup> However, circular dichroism in the photoionization (either single photon or multiphoton) of a molecule with no alignment or orientation has not been observed.

Some theoretical and experimental work has been performed in the area of circular to linear ratios,  $\Omega = \sigma_C/\sigma_L$ , as a means of ascertaining the symmetry of the excited electronic state. The following development, based on the work of McClain,<sup>65</sup> was initially used to assign the molecular symmetry of excited states of a randomly oriented fluid using two photon absorption. The two photon absorption strength,  $\delta$ , is given by the following:

$$\delta = |\epsilon_1 \cdot S_{if} \epsilon_2|^2 \quad (5.1)$$

where  $\epsilon_1$  and  $\epsilon_2$  are the polarization vectors of the two photons, and  $S_{if}$  is the two photon transition tensor between the initial and final states. In a randomly oriented system, the absorption strength must be averaged over all orientations which yields:

$$\langle \delta \rangle = \delta_F F + \delta_G G + \delta_H H \quad (5.2)$$

where  $\delta_F$ ,  $\delta_G$ , and  $\delta_H$  are molecular parameters, and F, G, and H are algebraic expressions dependent on the polarization vectors. The molecular parameters can be calculated from the transition tensor in the following manner:

$$\delta_F = S_{\alpha\alpha} S_{\beta\beta}^* \quad (5.3)$$

$$\delta_G = S_{\alpha\beta} S_{\alpha\beta}^* \quad (5.4)$$

$$\delta_H = S_{\alpha\beta} S_{\beta\alpha}^* \quad (5.5)$$

where the indices run over x, y, and z directions and repeated indices indicates summation. McClain has calculated the general form for the transition tensor for the various molecular symmetry groups. If one assumes that the ground state is fully symmetric, it can be shown that transitions which preserve the symmetry of the ground state electronic wavefunction yield  $\delta_F = 0$ , which corresponds to  $\Omega < 3/2$  (typically much less). For transitions which lower the symmetry of the ground state electronic wavefunction, i.e., the electronic state has less than the full molecular symmetry, the ratio becomes  $\Omega = 3/2$ . Application of the above guidelines to multiphoton ionization experiments requires the assumption that the effect of the ionizing photon be small. The ratios become valid at high laser intensity so that every molecule that reaches the two-photon resonance state is ionized. In that case, the ratio is primarily determined by the symmetry of the resonance state in the two photon absorption and not by the ionizing

photon. As the laser power decreases, the above model breaks down because the effect of the ionizing photon becomes more pronounced.

Berg et al.<sup>66</sup> have applied McClain's model to the multiphoton ionization of benzene. The observation of a (2+1) resonantly enhanced multiphoton ionization peak at a wavelength of approximately 391 nm in benzene was first made by Johnson.<sup>67</sup> The two-photon resonance has been assigned as an  $E_{1g}$  Rydberg state. Due to the symmetry of this state, the polarization ratio,  $\Omega$ , was expected to be equal to 3/2. Berg et al. obtained a range of 1.3 – 1.7 for the ratio which is in agreement with the expected value to within experimental errors. The MPI of benzene along with the polarization ratio will have some bearing on data presented later in this thesis.

In addition to the information acquired from circular to linear ratios, it was also a goal of this thesis to attempt to measure a circular dichroism in the ionization (i.e, a difference in the multiphoton ionization rate for left and right circularly polarized light). The observation of a circular dichroism in multiphoton ionization requires that there be a differential population of the resonant state for the two different laser polarizations. Meath and Power<sup>68,69</sup> have applied generalized Einstein B-coefficients to the two photon absorption process in molecules with permanent moments. Circular dichroism can then be related to the difference in the Einstein B-coefficients for right- and left-circularly polarized light:

$$CD \propto B_L - B_R \quad (5.6)$$

For one photon absorption, the Einstein B-coefficient is given by the following:

$$B = \frac{2\pi}{3\hbar^2} |\mu^{ni}|^2 \quad (5.7)$$

where  $\mu^{ni}$  is the electric dipole transition moment between the initial and final states given by:  $\langle n|\mu|i\rangle$ . Calculation of circular dichroism requires the inclusion of the magnetic dipole moment as well as higher order electric moments since the electric dipole term vanishes upon taking the difference in Einstein coefficients for right and left circularly polarized light. The interaction Hamiltonian thus becomes:

$$\hat{H}_{\text{int}} = -\mu \cdot E - m \cdot B - \frac{1}{2} Q \cdot \nabla E \quad (5.8)$$

where  $\mu$  is the electric dipole moment,  $m$  is the magnetic dipole moment,  $Q$  is the electric quadrupole moment, and  $E$  is the electric field. Meath and Power assumed a two level system and averaged over all possible orientations of the molecule to arrive at the following expression for circular dichroism in two photon absorption:

$$\Delta B = B_L^{(2)} - B_R^{(2)} \quad (5.9)$$

$$\Delta B = \frac{8\pi^2}{15\hbar^4 \omega^2 c} [3(\mu \cdot \text{Im} m)d^2 + (\mu \cdot d)(d \cdot \text{Im} m)] \quad (5.10)$$

$$d = \mu^m - \mu^i \quad (5.11)$$

where  $\mu$  is the electric dipole moment,  $m$  is the magnetic dipole moment, and  $d$  represents the difference in the permanent electric moments for the ground and excited states. An actual calculation of the two photon circular dichroism to fit a given experiment is a complicated task requiring knowledge of permanent electric and magnetic dipole moments. Tinoco<sup>70</sup> discussed differential two photon absorption in chiral molecules assuming only *transition* moments of both electric and magnetic dipole character. He defined the two photon circular dichroism in the following manner:

$$\delta_L - \delta_R = |\epsilon_1 \cdot S_{if} \epsilon_2|^2 - |\epsilon_1^* \cdot S_{if} \epsilon_2^*|^2 \quad (5.12)$$

where  $\epsilon_1$  and  $\epsilon_2$  are the polarization vectors of the two photons ( $\epsilon_1$  refers to left circularly polarized light and  $\epsilon_1^*$  refers to right circularly polarized light), and  $S_{if}$  is the two photon transition tensor between the initial and final states similar to the treatment that McClain applied to circular-to-linear ratios in two photon absorption. The two photon circular dichroism in this regime can then be shown to be:

$$\delta_L - \delta_R = \left(\frac{e}{m}\right)^4 \cdot \left(\frac{\pi}{\hbar^2 c^3}\right) \frac{g(2\nu)}{\nu} \frac{4}{15} C \quad (5.13)$$

where  $g(2\nu)$  is a normalized line shape and  $\nu$  is the exciting frequency. For two co-rotating circularly polarized beams, Tinoco has calculated the value of  $C$  to be:

$$C = 4(\beta_{of} - \gamma_{of}) \cdot \alpha_{of} \quad (5.14)$$

where the variables are defined in the following way:

$$\beta_{of} = \sum_i \frac{[p_{oi}(\bar{p} \times \bar{r})_{if} + \bar{p}_{if} \cdot (\bar{p} \times \bar{r})_{oi}]}{\nu_{oi} - \nu} \quad (5.15)$$

$$\gamma_{of} = \sum_i \frac{[(\bar{p} \cdot \bar{r})_{oi} \times \bar{p}_{if} + (\bar{p} \cdot \bar{r})_{if} \times \bar{p}_{oi}]}{\nu_{oi} - \nu} \quad (5.16)$$

$$\alpha_{of} = \sum_i \frac{p_{oi} p_{if} + p_{if} p_{oi}}{\nu_{oi} - \nu} \quad (5.17)$$

where  $\bar{r}$  and  $\bar{p}$  are the position and momentum vectors of the molecule, and  $p_{oi}$ ,  $p_{if}$  are the transition dipole moments summed over all allowed states of the molecule. Once again, actual calculation of a two photon circular dichroism is a difficult task. It is instructive to note that the magnitude of the two photon circular dichroism is expected to be similar to the one photon CD (approximately  $10^{-2}$  to  $10^{-3}$ ).

The chiral molecule 2-butylamine ( $C_4H_{11}N$ ) was chosen for a variety of reasons, including the high vapor pressure of the molecule at room temperature (which reduced possible contamination of the mass spectrometer due to coating of the walls and facilitated introduction of the sample into the chamber without the necessity of heating). Unfortunately, at the time we had no commercial circular dichroism instruments readily available, so the CD spectrum of this molecule was unknown. This posed a problem in determining the wavelength at which to take data. However, the absorption spectrum revealed that all absorption was in the UV. Hence, any circular dichroism would also occur in that region.

While electron impact studies of the fragmentation pathways of the butylamines are well known,<sup>71</sup> spectroscopic data using the multiphoton ionization technique have only recently been reported.<sup>72</sup> Watanabe, et al., determined the ionization potential of 2-butylamine to be 8.70 eV using a photoionization method.<sup>73</sup> The spectra of alkylamines are predominantly composed of Rydberg transitions.<sup>74</sup> Consequently, the lowest singlet excited state of the butylamines has been assigned as an  $X \rightarrow A, n \rightarrow 3s$  Rydberg transition in which the origin lies at approximately 5.21 eV (238 nm).

### Experimental

Mass spectra via multiphoton ionization were obtained using the apparatus described in chapter four of this thesis. Samples of the (R)-(-) and (S)-(+)-2-butylamine were purchased from Aldrich (99% purity) and used without further purification. The optically active sample was loaded into a glass ampoule and subjected to three freeze-pump-thaw cycles before being admitted into the TOFMS via the R. M. Jordan pulsed valve. The sample introduction system consisted of the glass ampoule for the sample as well as a



valved connection to a tank of either argon or xenon which acted as a carrier gas for the chiral sample. The stainless steel tubing and the pulsed valve had the option of heating to allow for greater sample density.

### Results and Discussion

It was first necessary to locate resonantly enhanced multiphoton ionization peaks before any attempts at measuring circular to linear polarization ratios or a circular dichroism in the ionization be made since these measurements are predicated on absorption to produce electronically excited states. A typical time-of-flight mass spectrum of the 2-butylamine (taken at 440.62 nm) is shown in Figure 39. Before continuing, there are several things of interest in the mass spectrum of this molecule that should be briefly mentioned. The first point is the substantial amount of fragmentation. Earlier data obtained using electron impact reveals a similar pattern. It is somewhat unusual to find that the mass spectrum acquired with laser ionization is so similar to that using electron impact ionization. From these electron impact studies, it was noted that 2-butylamine undergoes significant fragmentation via cleavage between the second and third carbon atoms in the chain. Analysis of the TOF data presented here confirms the presence of the  $C_2H_6N^+$  ( $m/z = 44$ ) that would result from cleavage of the molecule. A second strong peak occurs at  $m/z = 58$  which corresponds to the loss of a methyl group leaving the  $C_3H_8N^+$  fragment. A log-log plot of the signal versus power for the fragments produced a slope of approximately four, which indicates that the parent ion is the source of fragmentation. Through the use of a deuterated sample, Siuzdak and BelBruno<sup>72</sup> also concluded that ionization of the parent amine preceded fragmentation.

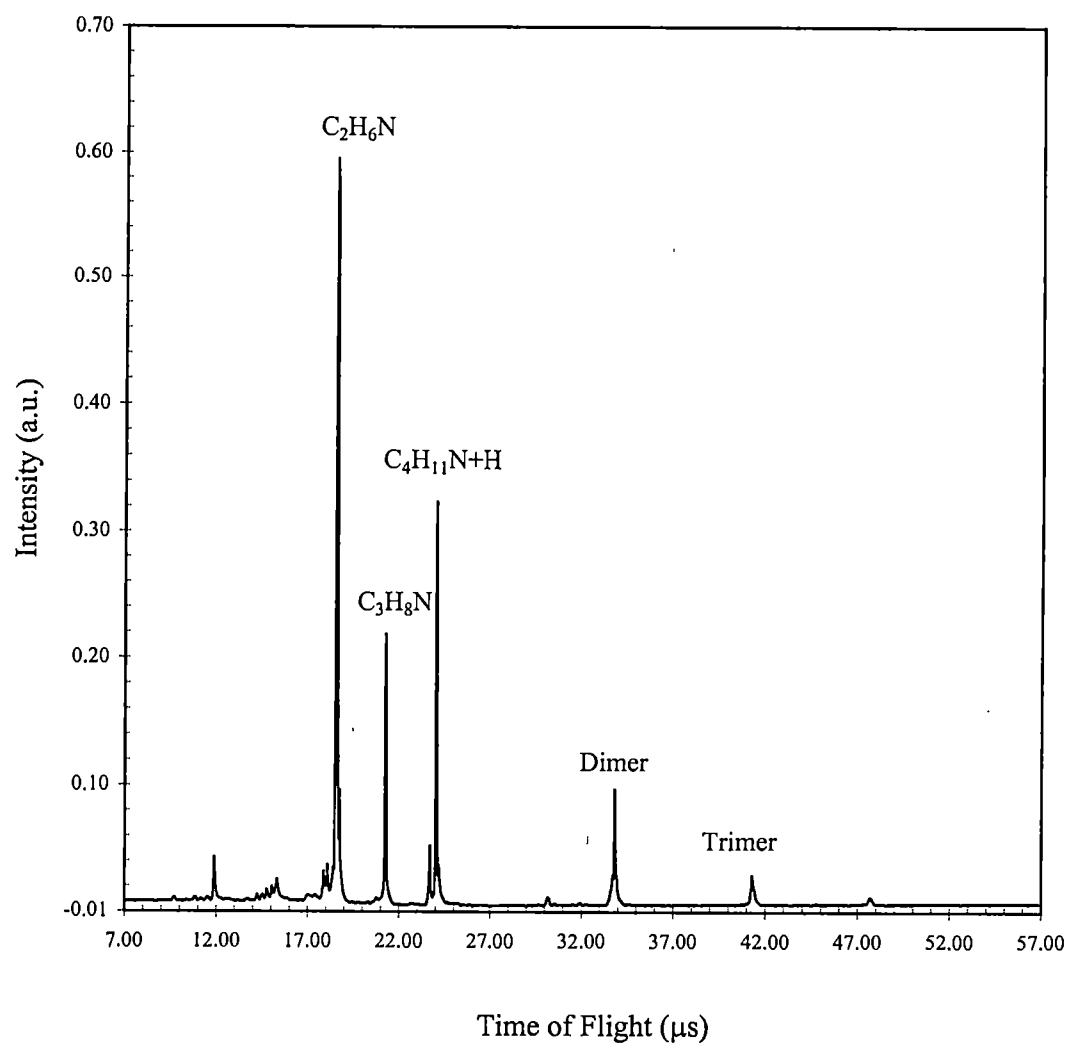


Figure 39. Mass spectrum of 2-butylamine.

A second point to notice in the mass spectrum is the presence of the dimer, trimer, and tetramer at higher backing pressures. As one would expect, the formation of these clusters was highly pressure dependent. In addition, careful inspection of the mass spectrum reveals that there is no evidence of the parent ion. The mass of the parent is 73 amu. However, the mass spectrum shows a peak at 72 amu which corresponds to the parent minus one hydrogen and a peak at 74 amu which corresponds to the parent plus one hydrogen. It has been shown that the loss of a hydrogen from an amine group (by comparison with ammonia) is a feasible fragmentation pathway,<sup>75</sup> so that peak is not entirely unexpected. However, the  $M^+H$  peak is somewhat surprising. A study of the pressure dependence of the clusters revealed that the pressure dependence of the  $M^+H$  peak closely resembled that of the clusters which indicated that this peak was being formed by the dissociation of the clusters. It should also be pointed out that the dimer peak corresponds to two 2-butylamine peaks plus a hydrogen, indicating that the clusters were hydrogen bonded. To verify that the  $M^+H$  ions were in fact being produced from the clusters, mass spectra were recorded using two different carrier gases (xenon and argon) since the carrier gas can serve to enhance or impair the formation of clusters. Of particular importance is the mass of the carrier gas. If the mass of the expansion gas matches that of the molecule, cluster formation can be enhanced. Figure 40 shows mass spectra taken with the two different carrier gases. Note that when argon (which has a mass of 40 amu) was used as the carrier, the cluster peaks are present along with the  $M^+H$  peak. In contrast, when xenon (which has isotopes that range in mass from 128 amu to 136 amu) was used as the carrier gas, there are no cluster peaks and the only peak

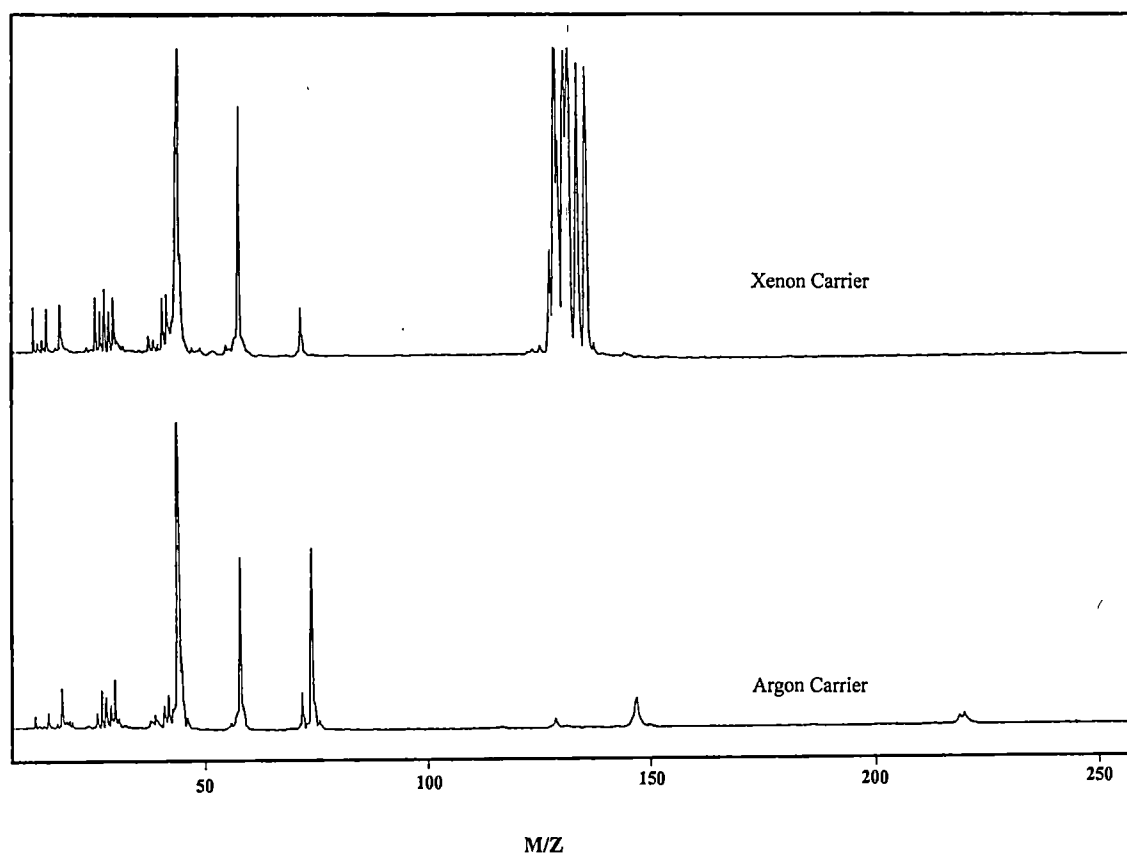


Figure 40. Mass spectra of 2-butylamine using xenon and argon as carrier gases.

near the parent ion is the  $M^+ - H$  peak. The  $M^+ + H$  is no longer present, thus indicating that the clusters were the source for this particular ion.

A final point to be made concerns the nature of the ionization, i.e., the nonresonant multiphoton ionization of 2-butylamine was quite prominent over a wide range of photon energies. In fact, when the laser was scanned from 430 nm up to 500 nm, there was a constant nonresonant background signal that slowly decreased in intensity as the wavelength increased. The intensity decrease is clearly indicated in Figure 41, which shows mass spectra taken at two different wavelengths. The top spectrum was taken at a wavelength of 451.74 nm with the laser power at 8.8 mJ/pulse, while the bottom spectrum was obtained at 483.00 nm with the laser power at 13.0 mJ/pulse. The sample pressures in the two cases were identical. The signal at 451.74 nm is noticeably stronger than the signal at 483.0 nm even though the longer wavelength laser pulse had much higher power.

The nonresonant signal was not optimum for studying polarization effects in ionization, so it was necessary to find resonance states within the nonresonant background. The observation of the  $n \rightarrow 3s$  Rydberg transition at approximately 474 nm in a (2+2) REMPI experiment by Siuzdak and BelBruno<sup>72</sup> prompted a closer inspection of the 475 nm to 465 nm wavelength range. Figure 42 shows several peaks in the  $C_2H_6N^+$  fragment ion (the boxcar was adjusted to monitor this particular fragment). The fragment ions showed structure identical to that in the  $M^+ - H$  peak, and since the fragment peaks were much stronger and easier to measure, it was decided to acquire data using the fragment. The two larger peaks are separated by  $680 \text{ cm}^{-1}$  which agrees with the spacing of

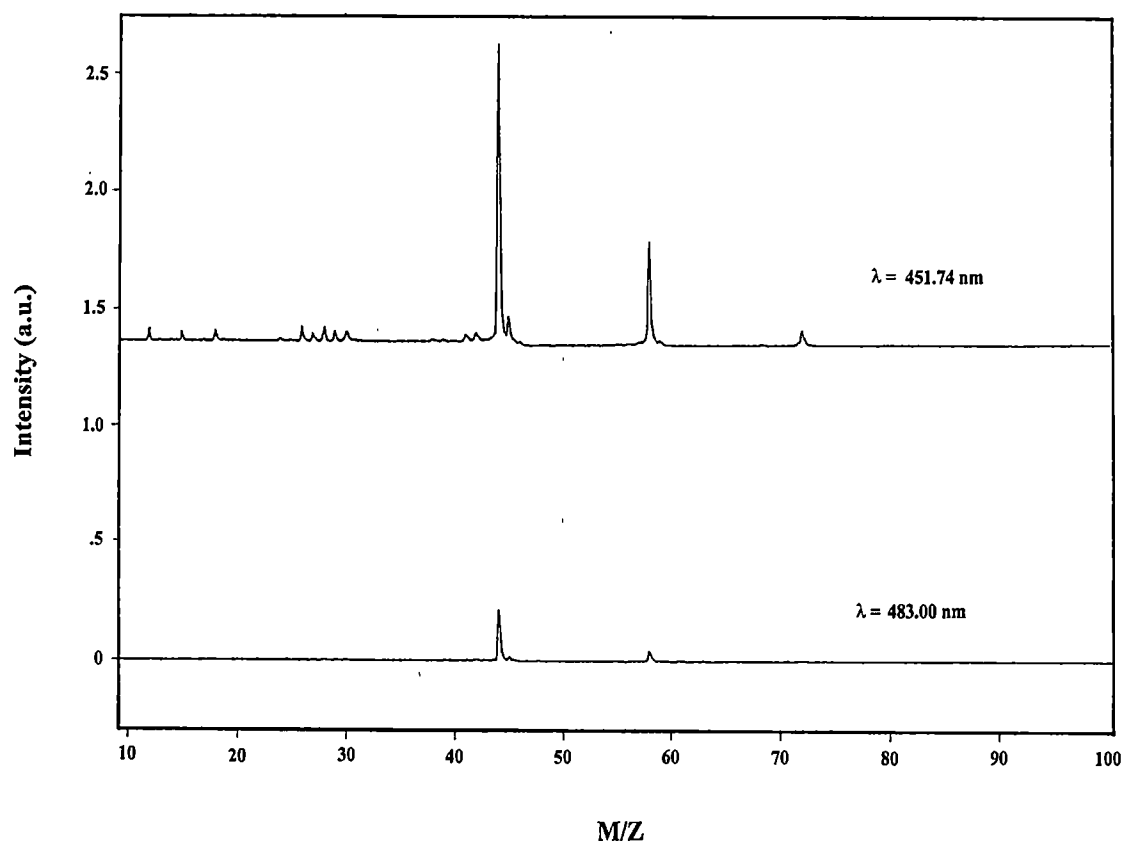


Figure 41. Mass spectra of 2-butylamine showing the decrease in ionization intensity for longer wavelengths.

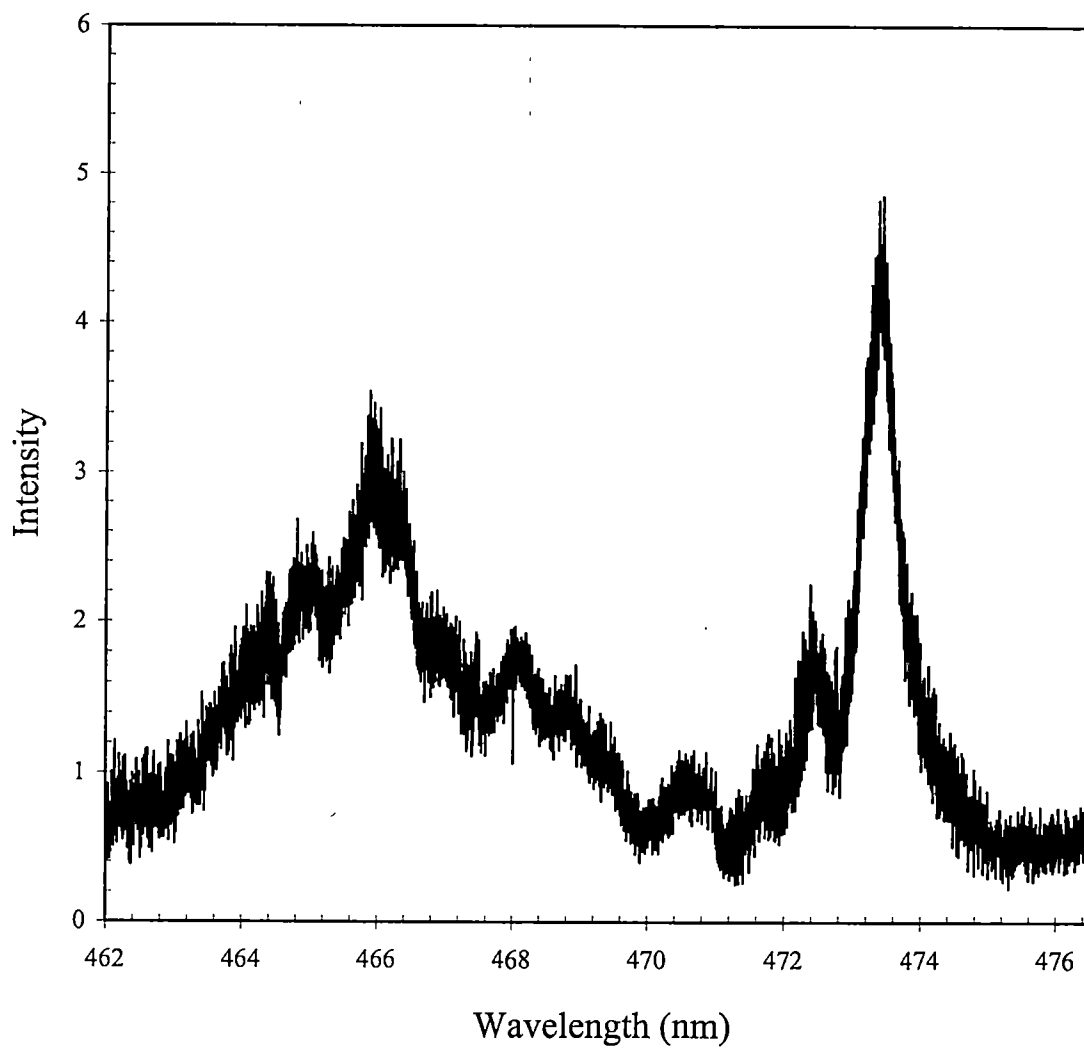


Figure 42. Wavelength dependence of 2-butylamine showing the (2+2) REMPI through the 3s Rydberg state.

approximately  $700\text{ cm}^{-1}$  in the vibrational progression previously reported. The smaller peaks (separated by  $\sim 70\text{ cm}^{-1}$ ) could possibly correspond to rotational structure.

In addition to the fragments, the wavelength dependence of the clusters was also studied. Data for the dimer is presented in Figure 43. It is interesting that the dimer exhibits a dip in intensity at the wavelength that corresponds to the peak in the molecule. This could be due to a loss of oscillator strength in the dimer to the molecule, or collisional dissociation of the dimer as a result of more intense fragmentation of the parent. Discovery of a reasonably intense resonance in the multiphoton ionization of 2-butylamine was a considerable step towards measuring the polarization ratios. At this point, the BASIC program used to acquire spectra (see Appendix II) was modified to perform the polarization experiments. Previously, intensity measurements from the boxcar integrator were recorded at regular time intervals and stored in a plain text file. The program was adjusted to read the intensity values from the boxcar at regularly spaced intervals for a predetermined length of time, and, since the laser operated at a set frequency, the same number of laser shots were recorded for each measurement. The program then averaged the intensity values and calculated a standard deviation as a measure of the error in the experimental values. The procedure was that the polarization of the laser was set using the optics described previously and the program acquired the data for approximately 100 laser shots. The laser polarization was then altered manually and data was once again collected.

The rate of ionization for circular to linear polarizations was initially investigated using a racemic mixture of 2-butylamine. The racemic mixture was used since the enantiomer was not required for this effect, i.e., circular to linear ratios are independent of the



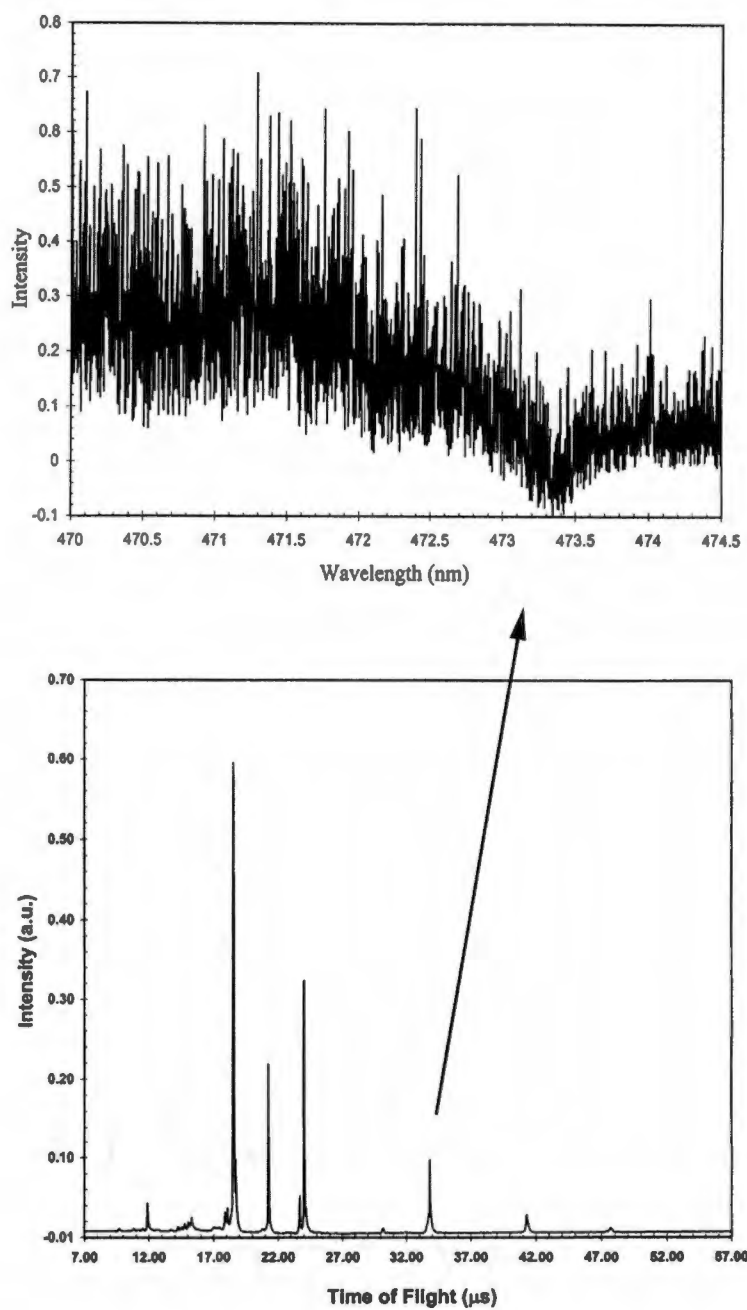


Figure 43. Wavelength dependence of the MPI of the 2-butylamine dimer showing the dip in signal at 473.35 nm.

chirality of the molecule. These ratios are primarily used as a method of determining the symmetry of the excited state. Figure 44 shows a plot of the ionization intensity as a function of the angle of the double Fresnel rhomb (which determined the polarization of the laser). The double Fresnel rhomb was rotated in  $5^\circ$  increments in order to adjust the laser beam through linear, elliptical, and left and right circular polarizations. The angle corresponds to the angle between the polarization vector of the laser beam incident on the single Fresnel rhomb and the vertical axis of the rhomb. The oscillation in the ionization signal is quite evident as the polarization of the laser was adjusted.

The ratio of circular to linear was determined to be  $1.25 \pm 0.03$  at an excitation wavelength of 473.35 nm for the 2-butylamine. This wavelength was chosen since the second photon is in resonance with the 3s Rydberg state of the molecule as previously discussed. The ratio of less than  $3/2$  indicates that the transition preserves the symmetry of the molecule. It must be pointed out that the work of McClain and Berg applies to the situation in which the second photon is in resonance with a real state of the molecule while only one photon is used in the ionization step. In this experiment, however, two photons are required to ionize the molecule after the second photon which again was in resonance with a real state of the molecule just as in Berg's case. It is unclear what effect, if any, the two photon ionization process will have on the circular to linear ratio. If we assume that every molecule that reaches the two photon resonance state becomes ionized, then it is probable that the preceding development would remain valid. The power density used in this experiment was quite high, approximately  $10^{11}$  W/cm<sup>2</sup>, so the assumption that all molecules that reach the resonance state become ionized is reasonable.

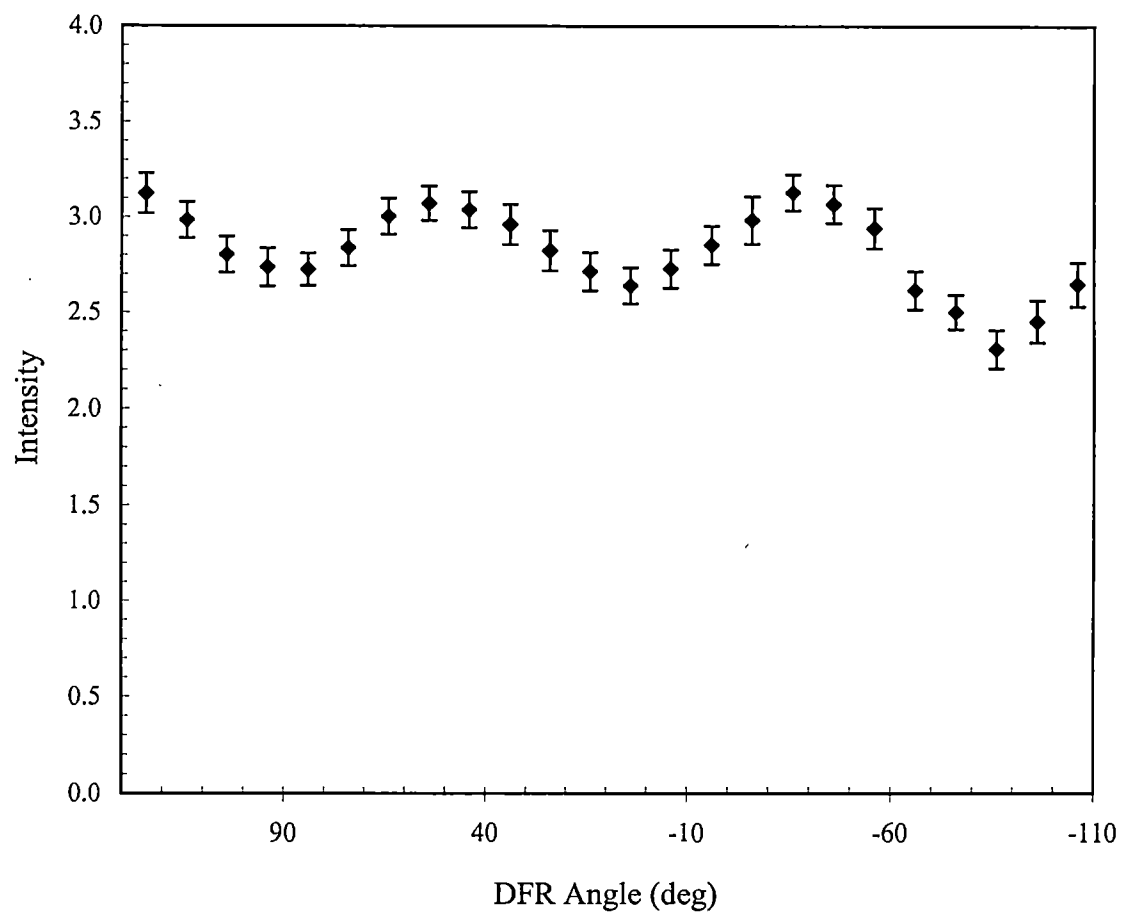


Figure 44. Polarization dependence of the MPI of racemic 2-butylamine at 473.35 nm.

The experiment was repeated for the (R)-(-)-2-butylamine (see Figure 45) and the same ratio was obtained within experimental error. The effect of the wavelength of the laser was studied by moving the laser to 470.00 nm and repeating the polarization experiment. The result of this experiment is shown in Figure 46. The oscillation of the intensity has clearly disappeared thereby indicating that the state, i.e., the molecular symmetry of the state, does in fact determine the ratio of circular to linear polarization. As a further experiment, the circular to linear ratio for the dimer peak was measured at an excitation wavelength of 473.35 nm (see Figure 47). As can be seen from the plot, there is no clear dependence on the circular to linear polarization in the dimer signal.

At this point, it is unclear from the data if there is a difference in the ionization for left and right circularly polarized laser light. In order to further explore the circular dependence the following procedure was adopted. Rather than continuously move through various polarizations, data was accumulated for approximately one hundred laser shots using right circularly polarized light. The polarization of the laser was then immediately adjusted to left circularly polarized light and the experiment was repeated. As a check on the data obtained in the linear experiments and for the sake of completeness, intensity measurements were also obtained for linearly polarized laser light. Figure 48 shows the results for (S)-(+)-2-butylamine. The circular-to-linear ratio is  $1.23 \pm 0.05$  which is in agreement with value obtained with the racemic mixture. From the plot of the data, it seems that the intensity of the ionization using left circularly polarized light is slightly larger (~1%) than the intensity of the ionization using right circularly polarized light. The ionization rates for the two different polarizations are:  $\sigma_{\text{RCPL}} = 2.62 \pm 0.12$ ,  $\sigma_{\text{LCPL}} = 2.78 \pm 0.10$ . The rates are the same within the statistical error of the

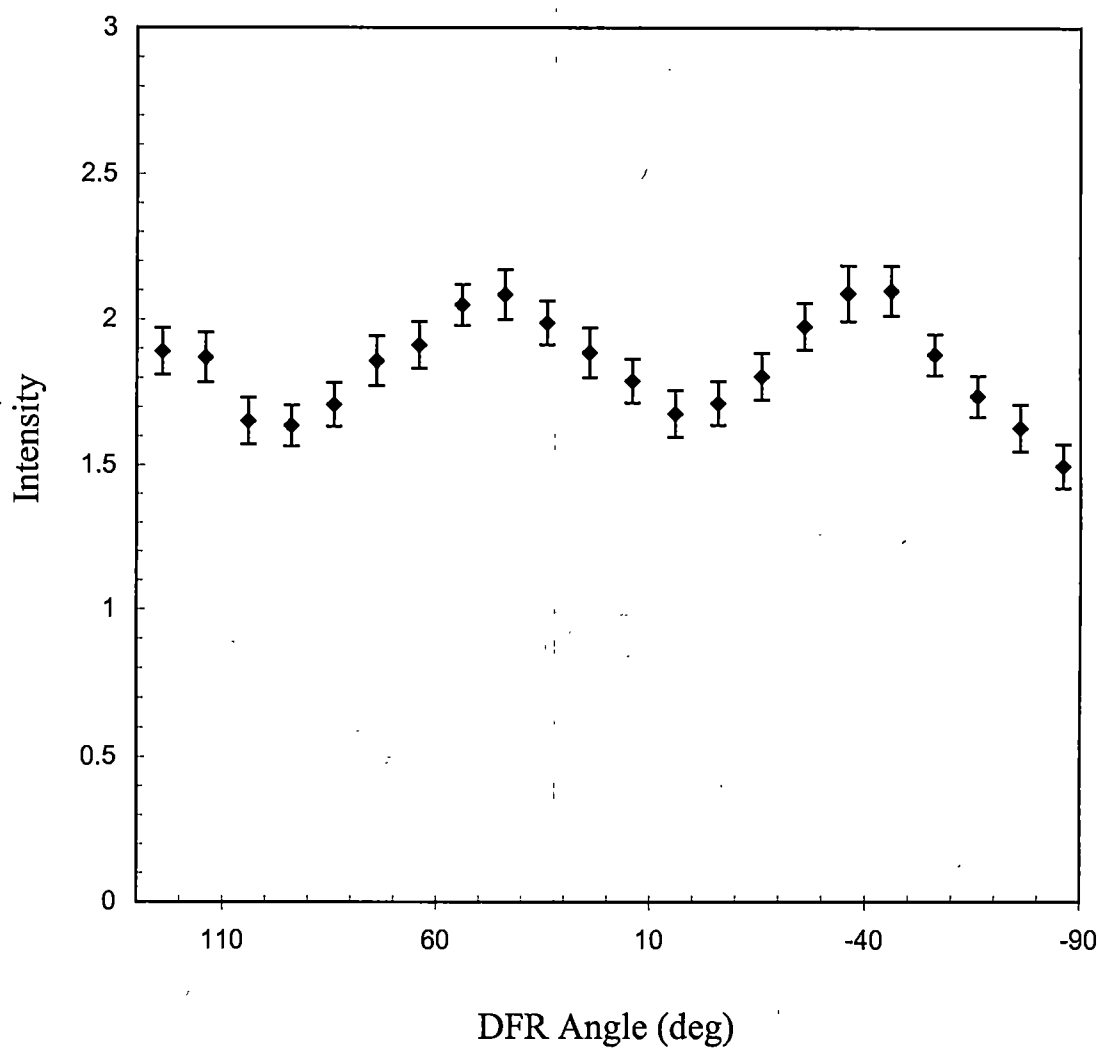


Figure 45. Polarization dependence of the MPI of (R)-(-)-2-butylamine at 473.35 nm.

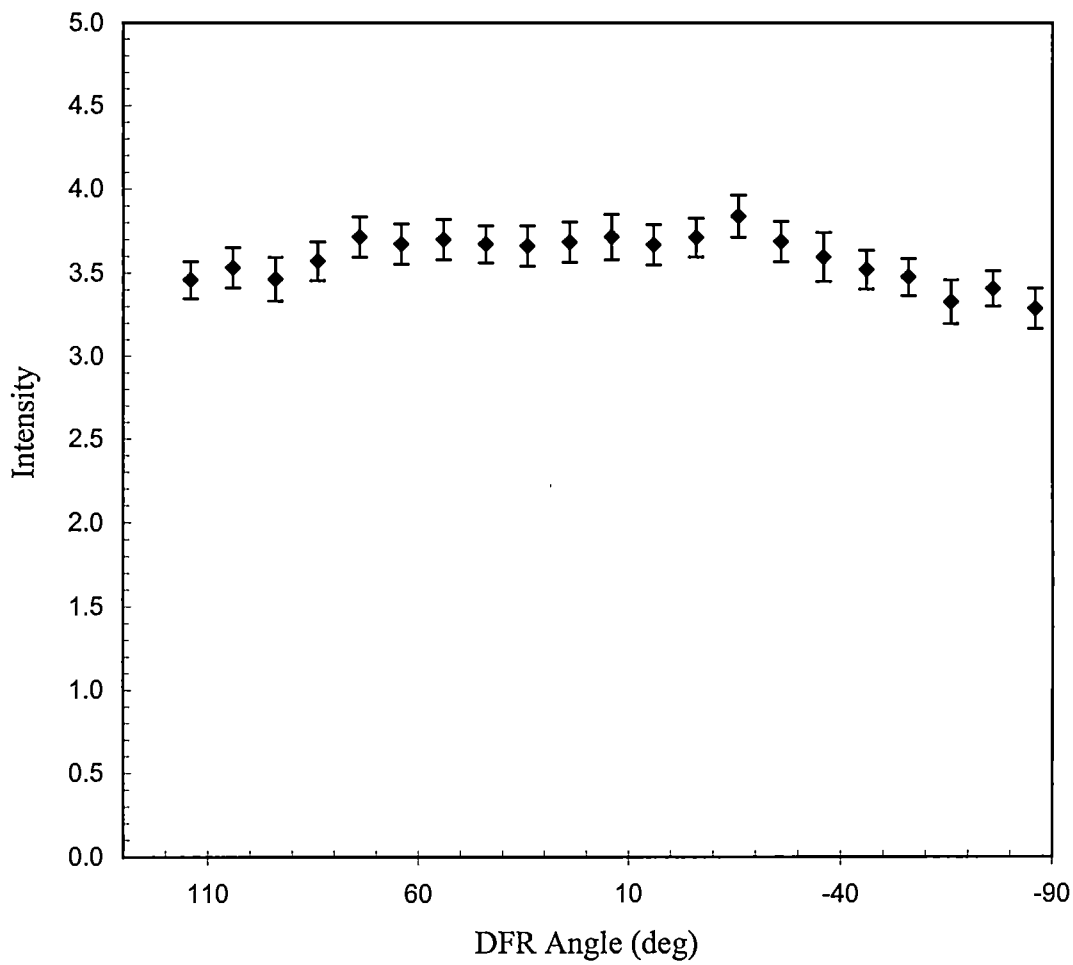


Figure 46. Polarization dependence of the MPI of (R)-(-)-2-butylamine at 470 nm.

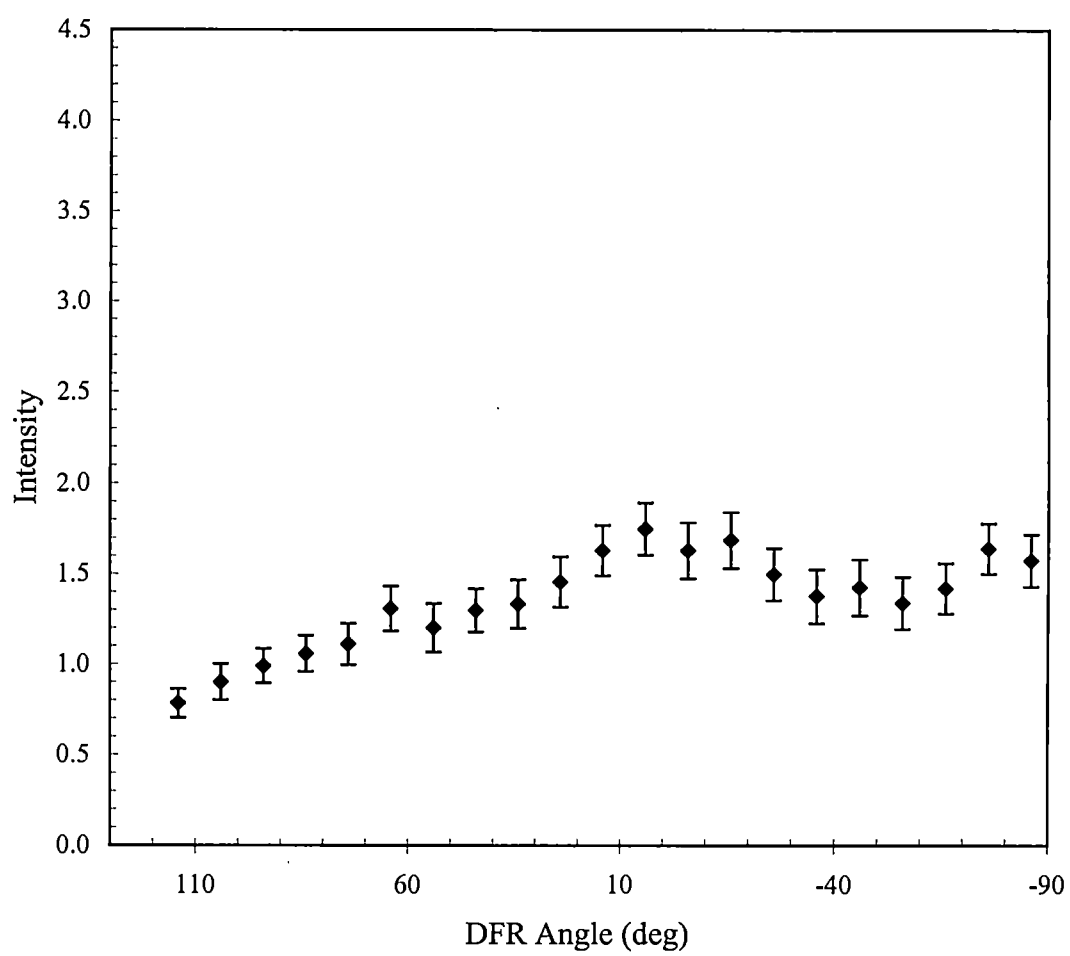


Figure 47. Polarization dependence of the MPI of racemic 2-butylamine dimer at 473.35 nm.

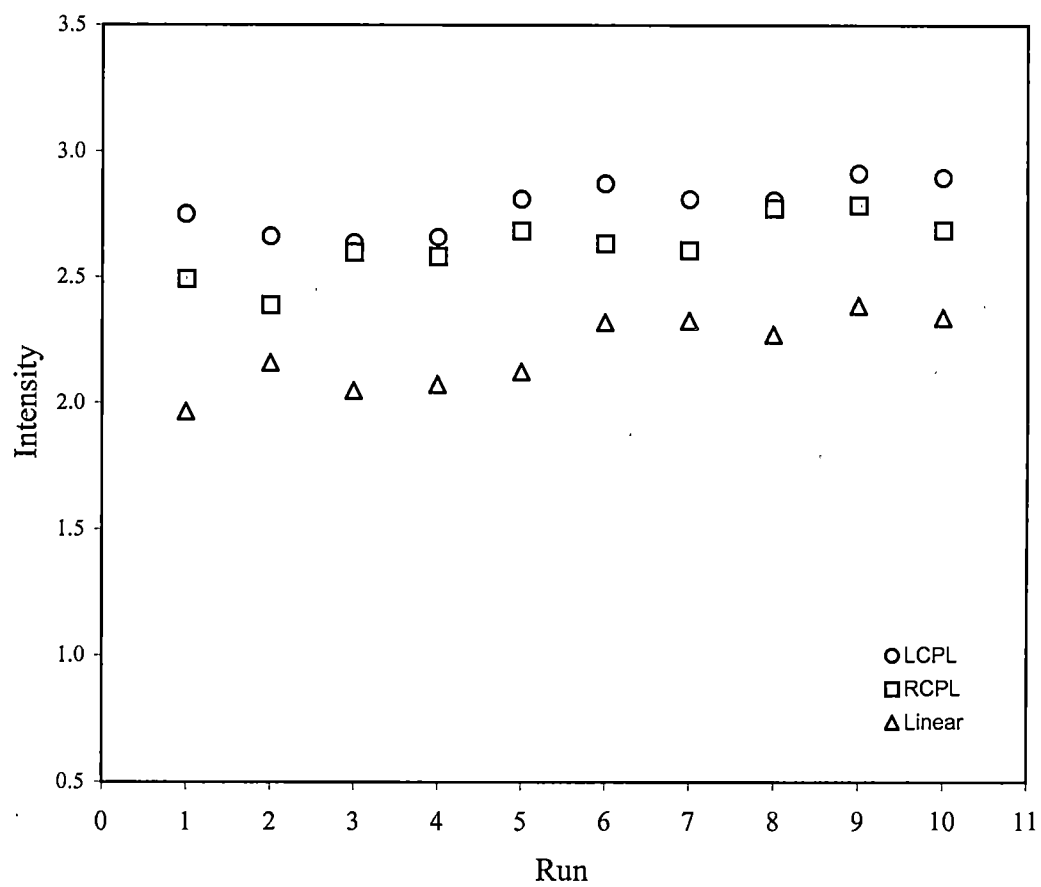


Figure 48. Polarization dependence of the MPI of (S)-(+)-2-butylamine at 473.35 nm.



experiment. However, it is interesting that the ionization rate with left circularly polarized light was consistently higher than the ionization rate with right circularly polarized light.

After replacing the (S)-(+)-2-butylamine with the (R)-(-)-2-butylamine, the results were identical, i.e., the ionization was still slightly larger with left circularly polarized light. The results of the circular dichroism experiment indicated an artifact in the experiment. As a result, the experiment was repeated using benzene since the circular to linear ratios were well documented and there should be no difference between the left and right circular polarizations since benzene is achiral and should not have a circular dichroism. In order to determine the appropriate wavelength for obtaining the circular to linear ratio in the benzene, a wavelength scan was taken and is shown in Figure 49. Polarization data was taken at a wavelength of 471.12 nm which corresponded to a (2+2) REMPI with the second photon in resonance with the  $14_0^1 1_0^3$  vibrational level of the  $^1B_{2u}$  electronic state of the benzene molecule. The results of this experiment are shown in Figure 50. Within experimental error, the ionization with left and right circularly polarized light are identical. There does not seem to be a preference as there was with the 2-butylamine and the circular-to-linear ratio was less than 3/2 ( $\sigma_C/\sigma_L = 1.62 \pm 0.004$ ) which is consistent with the symmetry of the molecular state.

Time-of-flight mass spectrometers are known to exhibit a memory effect. In other words, when one switches samples in the spectrometer, quite often the old sample shows up in the mass spectrum. The reason for this is that the sample, particularly those with rather low vapor pressures, can adhere to the walls of the gas introduction system and the pulsed valve. They can then become dislodged with the new sample and are detected in the

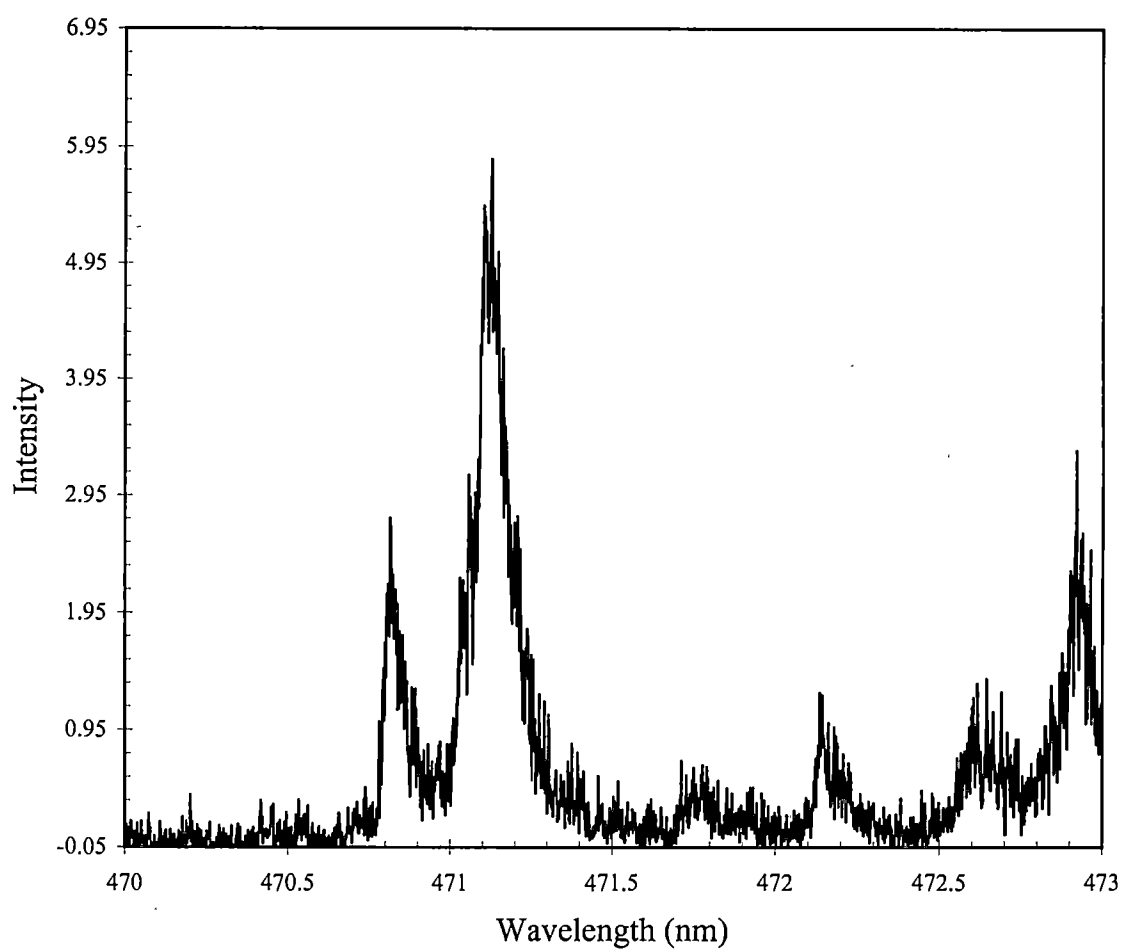


Figure 49. Wavelength dependence of the (2+2) REMPI of benzene through the  ${}^1B_{2u}$  state.

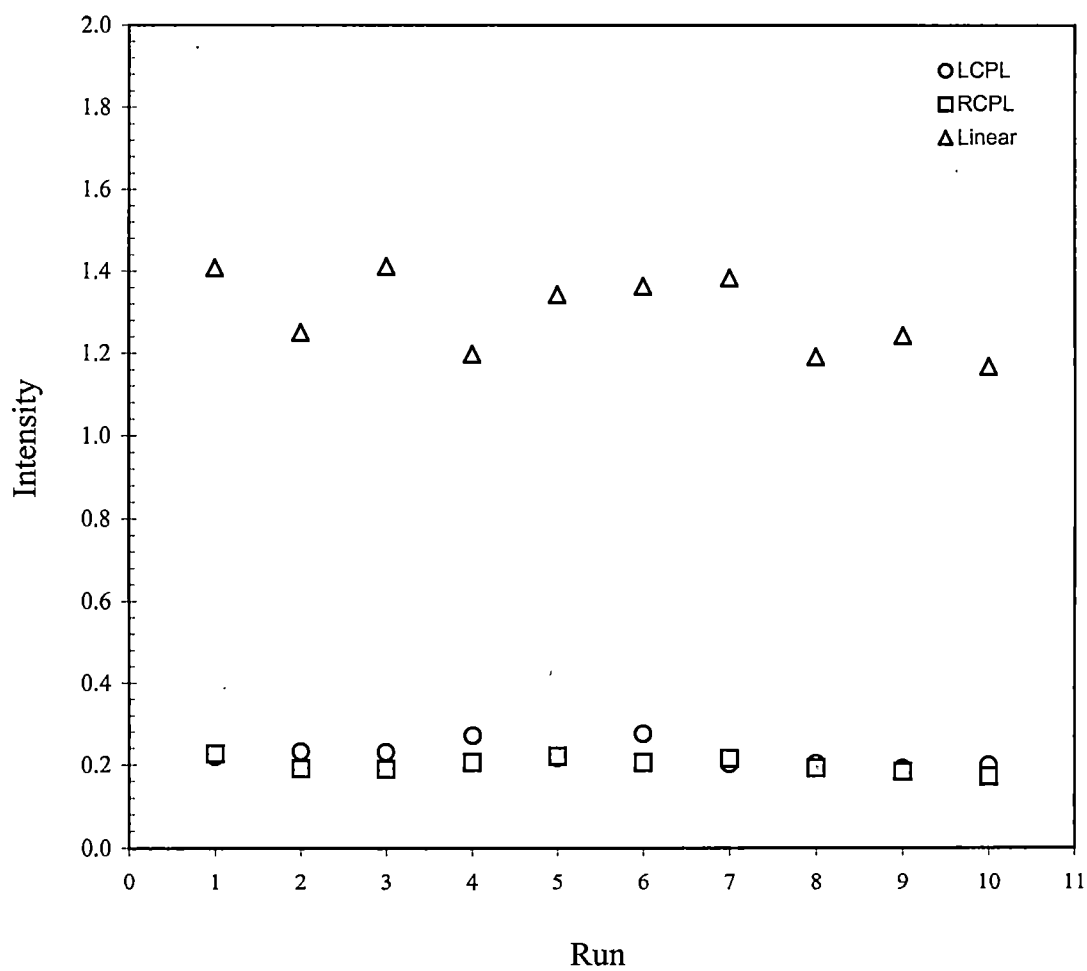


Figure 50. Polarization dependence of the MPI of benzene.

mass spectrometer. This was a possible explanation for the results of the 2-butylamine since it was conceivable that the (R)-(-)-2-butylamine was interfering with the measurement of the (S)-(+)-2-butylamine. The lines of the gas introduction system were replaced and the pulsed valve was heated while argon at high pressure was filtered through. In addition, the measurements of benzene were somewhat serendipitous since it could replace any 2-butylamine in the valve. After cleaning the system, the mass spectrum was checked with pure argon at approximately 50° C and no evidence of the 2-butylamine was found. The (R)-(-)-2-butylamine was then loaded into the glass ampoule and degassed as in the previous experiments. The polarization measurements were then repeated. The results are shown in Figure 51. This time the ionization rate with right circularly polarized light is slightly higher than the ionization rate with left circularly polarized light,  $\sigma_{\text{RCPL}} = 3.86 \pm 0.12$ ,  $\sigma_{\text{LCPL}} = 3.77 \pm 0.08$ . As in the case of the (S)-(+)-2-butylamine, the two values are the same within the statistical error of the experiment, but it is interesting that the ionization is now consistently greater with right circularly polarized light.

At this time, a commercial circular dichroism instrument became available and the one photon CD spectrum was obtained for the (R)-(-) 2-butylamine and is shown in Figure 52. Clearly, two photons using the 473.35 nm laser light per this experiment would not reach the CD peak, so the actual measurement of a circular dichroism with this molecule at 473.35 nm would be difficult.

### Conclusion

The circular-to-linear ratio was successfully measured to be approximately 1.25 for the racemic and the enantiomers of 2-butylamine. The ratio was consistent with a resonance

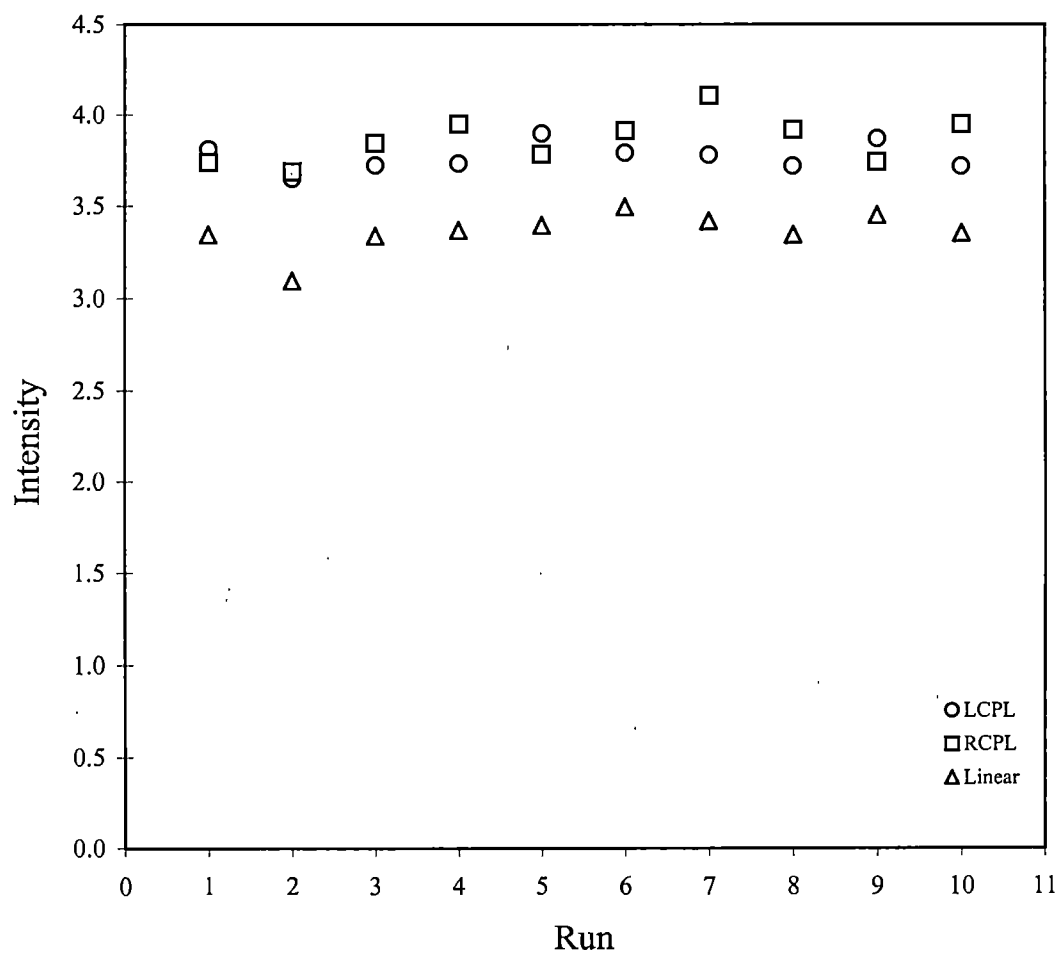


Figure 51. Polarization dependence of the MPI of (R)-(-)-2-butylamine at 473.35 nm.

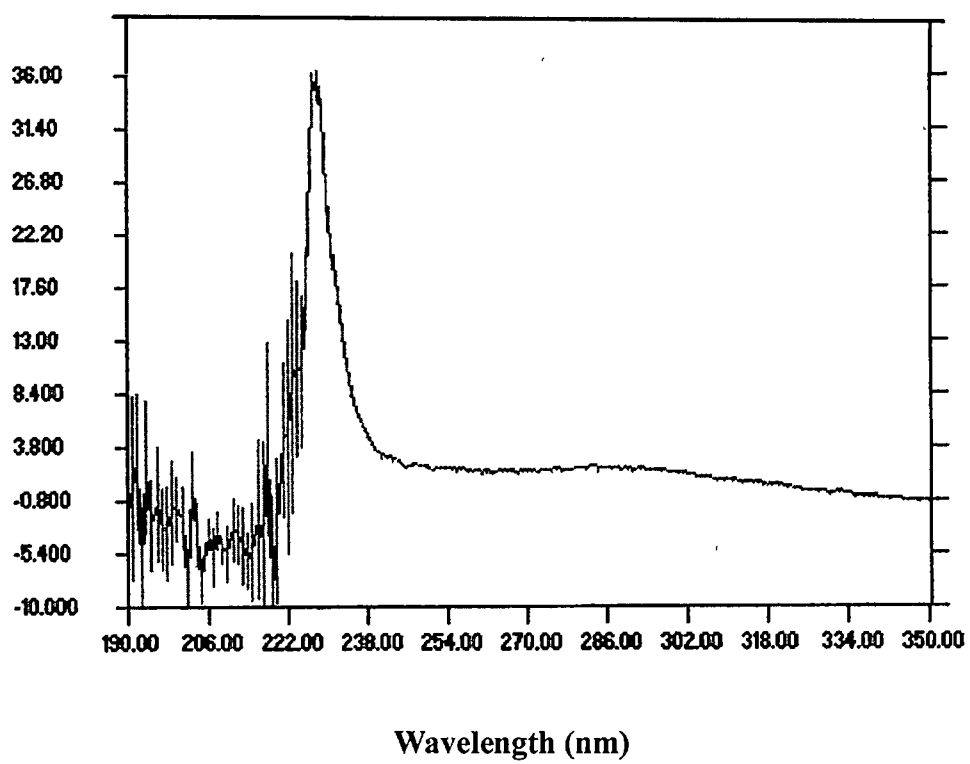


Figure 52. Circular dichroism of (R)-(-)-2-butylamine:

state that preserved the symmetry of the molecule. Within the boundaries of the experimental error, a circular dichroism in the multiphoton ionization of this chiral molecule in a (2+2) REMPI excitation through the 3s Rydberg state was not observed. However, the results indicate a possible effect that may be further studied with improvements in the experimental setup. The measurement of a circular dichroism in multiphoton ionization presents numerous experimental challenges. For instance, the stability of the laser is crucial in measuring such a minute quantity. Though it was hoped that averaging enough laser shots would reduce this error, it was discovered that the laser often would decrease in power over time in addition to the normal shot-to-shot fluctuations thus increasing the difficulty in measuring such a small quantity.

## CHAPTER VI

## CONCLUSIONS

A novel method for measuring optical rotation in chiral molecules was described. The primary advantages of this method were visual appeal and the possibility for determining optical rotations for dilute samples. A small energy difference (on the order of  $10^{-10}$  eV) was measured between the two enantiomers of an iron (II) phenanthroline complex using Mössbauer spectroscopy. Though this difference cannot be conclusively ascribed to the effect of the parity violating weak interaction, it does represent an important first step towards an observation of this fundamental difference in the regime of molecular spectroscopy.

The influence of spin polarized electrons emitted from a  $^{90}\text{Sr}$  beta source on the crystallizations of sodium chlorate and sodium bromate was investigated. The emission of circularly polarized bremsstrahlung radiation as the electrons decelerated in the solution was presented as a possible mechanism to explain the enantiomeric excesses observed in the crystallizations. In addition to the beta-radiolysis effects, a significant bias towards the formation of dextrorotatory crystals was observed in the crystallizations of sodium bromate. Though some chiral impurity is the most likely explanation for this bias, no proof was obtained to validate the presence of impurities. Since the sodium chlorate and sodium bromate experiments were performed in identical ways, it is reasonable to assume that if there was an impurity, it was most likely present in both the chlorate and the bromate. Hence, the impurity had a much greater effect on the crystallizations of sodium bromate.



The construction of a time-of-flight mass spectrometer was presented as a method for measuring polarization effects in the multiphoton ionization of a chiral molecule entrained in a nozzle jet expansion using a high resolution OPO laser. Circular-to-linear ratios were measured for the (2+2) resonantly enhanced multiphoton ionization of the chiral 2-butylamine through a 3s Rydberg state. An attempt was made to measure the difference in ionization rate for right- and left-circularly polarized light via the aforementioned multiphoton ionization of 2-butylamine. Within the statistical error of the experiment, no difference was measured, however, the data does indicate a possible effect. Further investigation with improved stability is required to verify the effect.

## List of References

1. J.B. Biot, *Mem. Inst.*, **1**, 1-372 (1812).
2. L. Pasteur, *A.C.R.*, **14**, 40 (1860).
3. A. Fresnel, *Ann. Chim. Phys.* **28**, 147 (1825).
4. R. de L. Kronig, *J. Opt. Soc. Am.*, **12**, 547 (1927).
5. R. Cameron, G.C. Tabisz, *Molecular Physics*, **90**, 159-164 (1997).
6. P. Drude, *Lehrbuch der Optik*; Hirzel: Leipzig, 1900; p 379. Dover: New York, 1959; English translation.
7. R.N. Zare, B.H. Spencer, D.S. Springer, M.P. Jacobson, *Laser Experiments for Beginners*, University Science Books: Sausalito, Ca, 1995; Expts 2-8, pp. 55-61.
8. S.M. Mahurin, R.N. Compton, R.N. Zare, *J. Chem. Ed.*, **76**, 1234 (1999).
9. T.M. Lowry, E.M. Richards, *J. Chem. Soc. London*, **125**, 2511 (1924).
10. T.D. Lee, C.N. Yang, *Phys. Rev.*, **104**, 254 (1956).
11. C.S. Wu, R.W. Hayward, D.D. Hoppes, R.P. Hudson, *Phys. Rev.*, **105**, 1413 (1957).
12. S.L. Glashow, *Nucl. Phys.*, **22**, 579 (1961).
13. S. Weinberg, *Phys. Rev. Lett.*, **19**, 1264 (1967).
14. A. Salam, "Elementary Particle Theory: Relativistic Groups and Analyticity (8<sup>th</sup> Nobel Symp.)," ed. N. Svartholm; Stockholm Almquist and Wicksell, 1968.
15. G. t'Hooft, *Nucl. Phys. B*, **33**, 173 (1971).
16. C.S. Wood, S.C. Bennet, D. Cho, B.P. Masterson, J.I. Roberts, C.E. Tanner, C.E. Weimann, *Science*, **275**, 1759 (1997).
17. Y.B. Zel'dovich, *Sov. Phys. - JETP*, **9**, 682 (1959).
18. M.A. Bouchiat, C. Bouchiat, *J. Phys. (Paris)*, **35**, 899 (1974).
19. L.M. Barkov, M.S. Zolotarev, *JETP*, **52**, 360 (1980).
20. T.D. Wolfenden, P.E.G. Baird, P.G.H. Sandars, *Europhys. Lett.*, **15**, 731 (1991).
21. S.J. Phipp, N.H. Edwards, P.E.G. Baird, S. Nakayama, *J. Phys. B*, **29**, 1861 (1996).

22. M.A. Bouchiat, C. Bouchiat, *Rep. Prog. Phys.*, **60**, 1351 (1997).
23. B.P. Masterson, C.E. Wiemann, "Atomic Parity Nonconservation in Precision Tests of the Standard Electroweak Model," pp. 545-576 (P. Langacker, Ed., World Scientific, Singapore, 1995).
24. D.W. Rein, *J. Mol. Evol.*, **4**, 15 (1974).
25. V.S. Letokhov, *Phys. Lett. A*, **53**, 275 (1975).
26. S.F. Mason, G.E. Tranter, *Mol. Phys.*, **53**, 1091 (1984).
27. A.J. MacDermott, G.E. Tranter, S.J. Trainor, *Chem. Phys. Lett.*, **194**, 152 (1992).
28. Bakasov, T. K. Ha, M. Quack, *J. Chem. Phys.*, **109**, 7263 (1998).
29. A. Hegstrom, D.W. Rein, P.G.H. Sandars, *J. Chem. Phys.*, **73**, 2329 (1980).
30. J.K. Laerdahl, P. Schwerdtfeger, *Phys. Rev. A*, **60**, 4439 (1999).
31. E. Arimondo, P. Glorieux, T. Oka, *Optics Comm.*, **23**, 369 (1977).
32. Ch. Daussy, T. Marrel, A. Amy-Klain, C.T. Nguyen, Ch.J. Borde, Ch. Chardonnet, *Phys. Rev. Lett.*, **83**, 1554 (1999).
33. J.K. Laerdahl, P. Schwerdtfeger, H.M. Quiney, *Phys. Rev. Lett.*, **84**, 3811 (2000).
34. A.L. Barra, J.B. Robert, *Mol. Phys.*, **88**, 875 (1996).
35. A. Allerhand, R. Addleman, D. Osman, *J. Am. Chem. Soc.*, **107**, 5809 (1985).
36. L. Keszthelyi, *J. Biological Phys.*, **20**, 241 (1994).
37. P. Frank, W.A. Bonner, R.N. Zare, "On One Hand But Not the Other: The Challenge of the Origin and Survival of Homochirality in Prebiotic Chemistry," (in press).
38. G. Schlessinger, *Inorganic Chem.*, **12**, 267 (1970).
39. A. Zalkin, D. Templeton, T. Ukei, *Inorganic Chem.*, **12**, 1641 (1973).
40. F. Basolo, J.C. Hayes, H.M. Neumann, *J. Am. Chem. Soc.*, **76**, 3807 (1954).
41. R.N. Compton, private communication.

42. I. Adams, J.M. Thomas, G.M. Bancroft, K.D. Butler, M. Barber, *J. Chem. Soc. D*, 751 (1972).
43. A.S. Lahamer, S.M. Mahurin, R.N. Compton, D. House, J.K. Laerdahl, M. Lein, P. Schwerdtfeger, *Phys. Rev. Lett.*, **85**, 4470 (2000).
44. F.S. Kipping, W.J. Pope, *J. Chem. Soc. (London) Trans.*, **73**, 606 (1898).
45. J.W. Mullin, "Crystallization." Cleveland: CRC Press; 1972, p. 136-150.
46. S.T. Kipping, W.J. Pope, *Nature*, **59**, 53 (1898).
47. D.K. Kondepudi, R. Kaufman, N. Singh, *Science*, **250**, 975 (1990).
48. A.D. Randolph, M.D. Larson, "Theory of Particulate Processes", 2<sup>nd</sup> ed., Academic Press: San Diego, 1988.
49. G. Beurskens-Kerssen, J. Kroon, H.J. Endeman, J. van Laar, J.M. Bijvoet, "Crystallography and Crystal Perfection," Ed. G.N. Ramachandran. Academic Press: New York and London, 1963.
50. L. Keszthelyi, *Phys. Lett.*, **64A**, 287 (1977).
51. A. Mozumder, "Fundamentals of Radiation Chemistry," San Diego: Academic Press, 1999.
52. M. Goldhaber et al., *Phys. Rev.*, **106**, 826 (1957).
53. P.M. Johnson, M.R. Berman, D. Zakheim, *J. Chem. Phys.*, **62**, 2500 (1975).
54. J.C. Miller, R.N. Compton, *J. Chem. Phys.*, **84**, 675 (1986).
55. D. Zakheim, P. Johnson, *J. Chem. Phys.*, **68**, 3644 (1978).
56. H. Haberland, U. Buck, M. Tolle, *Rev. Sci. Inst.*, **56**, 1712 (1985).
57. J.A.R. Samson, *Rev. Sci. Inst.*, **40**, 1174 (1969).
58. M.G. White, W.A. Chupka, M. Seaver, A. Woodward, S.D. Colson, *J. Chem. Phys.*, **80**, 678 (1984).
59. W.C. Wiley, I.H. McLaren, *Rev. Sci. Inst.*, **26**, 1150 (1955).
60. S. Klarsfield, A. Maquet, *Phys. Rev. Lett.*, **29**, 79 (1972).
61. H.R. Reiss, *Phys. Rev. Lett.*, **29**, 1129 (1972).

62. H.S. Carman, R.N. Compton, *J. Chem. Phys.*, **90**, 1307 (1989).
63. J. Paul, K. Siegman, *Chem. Phys. Lett.*, **304**, 23 (1999).
64. LE. Cuellar, C.S. Feigerle, H.S. Carman, R.N. Compton, *Phys. Rev. A*, **43**, 6437 (1991).
65. W.M. McClain, *J. Chem. Phys.*, **55**, 2789 (1971).
66. J.O. Berg, D.H. Parker, M.A. El-Sayed, *J. Chem. Phys.*, **68**, 5661 (1978).
67. P.M. Johnson, *J. Chem. Phys.*, **62**, 4562 (1975).
68. W.J. Meath, E.A. Power, *J. Mod. Optics.*, **36**, 977 (1989)
69. E.A. Power, "New Frontiers in Quantum Electrodynamics and Quantum Optics," Ed. A.O.Barut, Plenum Press: New York, 1990.
70. I. Tinoco, *J. Chem. Phys.*, **62**, 1006 (1975).
71. Mass Spec Data Center, National Institute of Standards and Technology.
72. G. Siuzdak, J.J. BelBruno, *J. Phys. Chem.*, **94**, 4559 (1990).
73. K. Watanabe, T. Nakayama, J.R. Mottl, *J. Quant. Spec. Rad. Trans*, **2**, 369 (1962).
74. M.B. Robin, "Higher Excited States of Polyatomic Molecules," Academic Press: New York, 1974.
75. H. Okabe, "Photochemistry of Small Molecules," Wiley: New York, 1978.

## Appendices

## APPENDIX I

```
CLS

REM  Open serial port 1 at baud rate of 9600
      OPEN "COM1: 9600, N, 8, 1, CS, DS, CD" FOR RANDOM AS #1

REM  Open file to store data
      INPUT "Enter filename: "; fout$
      OPEN fout$ FOR OUTPUT AS #2

REM  Enter wavelength range
      INPUT "Enter the beginning wavelength: "; STARTWAVE
      INPUT "Enter the ending wavelength: "; ENDWAVE

      PRINT "Hit enter to begin"
      50 b$ = INKEY$
      IF b$ = "" THEN GOTO 50

      PRINT #2, STARTWAVE, ENDWAVE
      PRINT #2,
      PRINT #2,
      PRINT #1, ""

REM  Set all values of A/D Converter to default settings
      PRINT #1, "MR"

REM  Set the first 7 ports as input ports
      PRINT #1, "I7"

100  REM  Starting point
      y = y + 1

REM  Read value of port 1 and saves it as variable, v
      PRINT #1, "?1"
      INPUT #1, v

REM  Time delay
```



```
FOR a = 1 TO 500
NEXT a

REM Saves values of cycle number (y) and voltage reading (v) to file

PRINT #2, y; v
CLS

REM Prints cycle number and voltage on the screen

PRINT y; v

REM Stop routine

a$ = INKEY$
IF a$ = "" THEN GOTO 100
PRINT "Program Complete"
CLOSE
END
```

## APPENDIX II

```
CLS

REM  Open serial port 1 at baud rate of 9600

      OPEN "COM1:9600, N, 8, 1, CS, DS, CD" FOR RANDOM AS #1

REM  Open file to store data

      INPUT "Enter filename: "; fout$
      OPEN fout$ FOR OUTPUT AS #2
      PRINT "Hit enter to begin"
      50 b$=INKEY$
      IF b$="" THEN GOTO 50
      PRINT #2,
      PRINT #2,
      PRINT #1, ""

REM  Reset all values in the A/D Converter to default settings

      PRINT #1, "MR"

REM  Designate first 7 ports as input ports to receive data

      PRINT #1, "I7"

REM  Dimension array variables to store data
REM  Starting point

      FOR y = 1 TO 100

REM  Read value of port 1

      PRINT #1, "?1"
      INPUT #1, v

REM  Time delay

      FOR a = 1 TO 500
      NEXT a

REM  Saves voltage read to array for future standard deviation calculation

      x(y) = v
```

```
REM Prints data to file and to the screen

PRINT #2, y; v
CLS
PRINT y; v

REM Sums the voltages for calculation of the average

b = b + v

NEXT y

REM Calculation of the average voltage

avg = b/y

REM Calculation of the standard deviation

FOR i = 1 TO 100
S(i) = (x(i) - avg)^2
Next i

FOR i = 1 TO 100
S = S + S(i)
Next i

Sx = (S/(y-1))^.5

PRINT #2,
PRINT #2,
PRINT #2, avg
PRINT "Average: "; avg
PRINT #2,
PRINT "Standard Deviation: "; Sx
PRINT "Program Complete"
CLOSE
END
```

## VITA

Shannon Mahurin was born in Stuttgart, Germany on September 2, 1972. He attended public schools in Indianapolis, Indiana and Bell County, Kentucky, where he graduated from Bell County High School in May 1990. He enrolled at Cumberland College, Williamsburg, Kentucky in August 1990. He received a Bachelor of Science degree in physics from Cumberland College in May 1994. After one year of study at Eastern Kentucky University, Richmond, Kentucky, he entered the physics graduate program at the University of Tennessee, Knoxville, in August 1995 where he worked under the direction of Dr. Robert Compton in the area of chemical physics. The doctoral degree was received in December 2000.